# Framework for a Unified Macroscale Model of Magnetostriction

Alecsander N. Imhof

Dissertation submitted to the Faculty of the
Virginia Polytechnic Institute and State University
in partial fulfillment of the requirements for the degree of

Doctor of Philosophy
in
Engineering Mechanics

Gary Seidel, Chair
Giti Khodaparast
Scott W. Case
Uwe C. Täuber

May 1, 2025
Blacksburg, Virginia

Keywords: Non-linear Constitutive Model, Thermodynamically consistent Numerical Approximation, Internal State Variable Theory

# Framework for a Unified Macroscale Model of Magnetostriction

Alecsander N. Imhof

(ABSTRACT)

This dissertation presents the development of a framework for a unified mutliscale model of magnetostriction. The lack of accurate models of macroscale hysteretic magnetostriction has inhibited the development of novel devices and savings. This thesis presents a framework for such a model. After motivating and providing the necessary background knowledge regarding these models, an analytic model of anhysteretic magnetostriction will be derived using equilibrium statistical mechanics. It will be shown how specific assumptions regarding the symmetry of key micromagnetic energies (magnetocrystalline, magnetoelastic, and Zeeman) reduce a general three-dimensional statistical mechanics model to a one-dimensional form with an exact solution. Additionally, a useful form of the analytic equations that ensures numerical accuracy will be provided. Furthermore, a comparison to experimental data performed for several magnetostrictive materials will show that the model accurately predicts the behavior of Terfenol-D while two different iron gallium alloys are modeled with varying accuracy. Next, this dissertation attempts to expand the 1D model to two dimensions. This requires numerical approximation techniques which take the form of quadrature methods in the existing magnetostrictive literature. Examining the inherent assumptions of models in the literature highlights that they often produce artificial spurious responses due to numerical inaccuracy. An analysis of several quadrature methods is presented and it is shown how the numerical accuracy of the approximation techniques impacts the validity of the resulting magnetostrictive constitutive models. The numerical accuracy for each method is presented, and the influence of this accuracy on the model's predictions is analyzed. The ability of the most accurate method to simulate experimental data from the literature is tested. Results show that when inaccurate numerical approximations are used the resulting constitutive mdoels have degenerate / non-physical behaviors that limit their utility. Finally, the preliminary research necessary to construct a thermodynamically consistent model for magnetostrictive hysteresis will be presented. This model will be inspired by existing continuum hysteresis models including the Jiles-Atherton model and plasticity-based models. The potential next steps of realizing this model are then proposed.

# Framework for a Unified Macroscale Model of Magnetostriction

Alecsander N. Imhof

(GENERAL AUDIENCE ABSTRACT)

Magnetic materials have a non-linear dependence on mechanical forces. Unfortunately, many of the existing models cannot accurately simulate this coupling of magnetism and mechanics at size scales relevant to device design. This effort is particularly difficult as modeling the dissipative and lossy processes of a purely magnetic system is its own ongoing area of research. This dissertation intends to provide an unambiguous framework that allows for an intuitive understanding of how to couple all of the complex phenomena of these materials. It is the hope that this framework will inspire advances in the field of magnetostrictive modeling which in turn enables further advancement of technologies that have already facilitated benefits in the fields of biomedicine and energy efficiency.

# Dedication

*I would like to dedicate my work to my loving and supportive family, without whom I would not have been able to accomplish this endeavor. My parents Andrew and Sandra Imhof have been a continuous source of aid and I hope I have made them proud. My twin brother Anthony and younger sister Adriana helped to keep me in good spirits whenever times were hard and I'm very lucky to have them.*

# Acknowledgments

I must acknowledge and thank my advisor Dr. John Domann. His knowledge and dedication to the pursuit of quality research was nothing short of inspirational. His guidance and support throughout my graduate career has instilled in me an appreciation for the demands of scientific progress and understanding, and for that I am forever grateful. I would also like to acknowledge my former labmates Michael Goforth and Priya Shanmugam. I most certainly would not have made it through graduate school without their camaraderie and can only hope I offered them the same comfort they offered me. Finally, during the week of my final exam I was without power and only with the kindness and generosity of my cousin Brandon Posa, my friends Ryan and Alena Ochsenhirt, and the fine folks at Atrium Staffing was I able to complete and present my work to my committee. I quite literally could not have done this without them.

# Contents

# List of Figures

# List of Tables

# Chapter 1

# Introduction

## 1.1 Introduction

Magnetostriction is the spontaneous strain that occurs when a magnetic material is subjected to a magnetic field. It is one of the numerous effects under the umbrella term magnetoelasticity which describes the coupling between magnetization and elasticity, thermal expansion, strain, and torsion. Because they convert magnetic energy into mechanical energy and vice versa magnetostrictive materials are classified as 'active' or 'smart' materials. This property lends itself to both actuating and sensing devices in numerous different applications including micropositioning [26, 182], active vibration control [64, 77, 109], or miscellaneous applications in the fields of aerospace [22, 177, 180] and biomedicine [76, 79, 141]. These potential applications have increased interest in magnetostrictive materials which in turn has motivated the development of increasingly accurate material models. In order to fully realize the potential of these devices advanced predictive models of magnetostriction are required. Many of the current magnetostrictive models that exist in the literature were developed by introducing ad hoc mechanical dependence into previously established magnetism models. As a result, these models are unable to simulate the magnetostrictive effects essential to the aforementioned devices.

Magnetometers offer an example of both the advantages that magnetostriction based devices offer and how current models inhibit their design. Extremely subtle changes in magnetic flux are currently detected using superconducting quantum interference devices (SQUIDs). Unfortunately, these devices are expensive to maintain and operate as they require cryogenic refrigeration and intense magnetic shielding. Magnetostrictive magnetometers are an attractive alternative as they are smaller, cost-efficient, have lower power consumption, and can withstand mechanical disturbances. The key phenomenon at the core of these devices is the $\Delta E$ effect which describes the change in stiffness of a magnetostrictive material under an applied magnetic field. While the elastic Young's modulus of the material does not change, the total stiffness of the material is also dependent on a magnetostrictive compliance term. This change in stiffness can be measured by combining the magnetostrictive material with a piezoelectric material to create a microelectromechanical system (MEMS) resonator. Figure 1.1 (a) shows a representation of this device, the resonance frequency of which will be modulated by a change in stiffness. The detuning of the resonance frequency will modulate the current running through the sensor which serves as a measurement of the magnetic field.

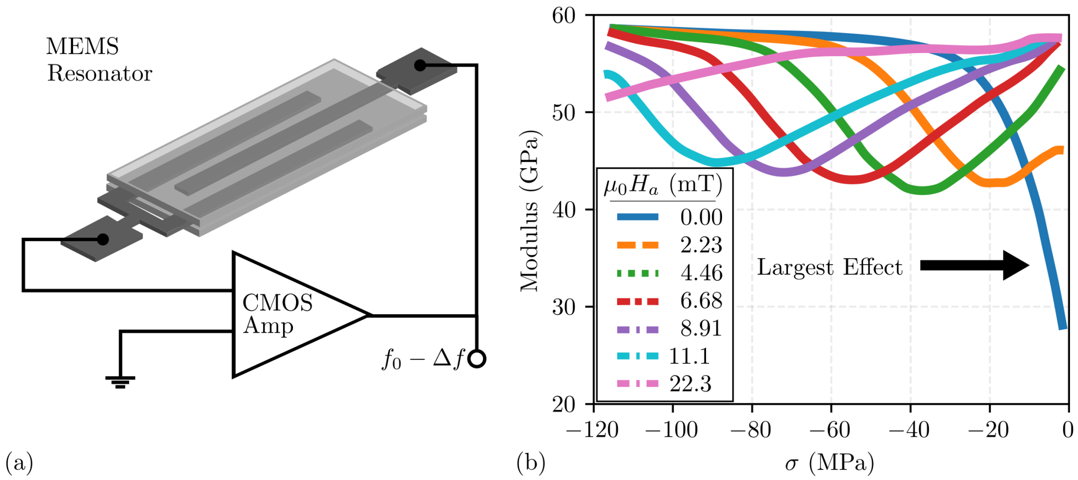

Figure 1.1: (a) Schematic illustration of the resonant magnetoelectric MEMS-CMOS magnetic field sensor (b) $Fe_{81.0}Ga_{19.0}$ Young's Modulus stress response for varied applied magnetic fields. Digitized from [97].

Figure 1.1 (b) is a plot of the Young's modulus of the magnetostrictive alloy iron gallium

($Fe_{81.0}Ga_{19.0}$) against applied stress at various applied magnetic fields. This data was digitized from Kellog *et al.* [97] and shows that the magnitude of the $\Delta E$ effect decreases under increasing magnetic fields. Note that the $\Delta E$ is most pronounced when no magnetic field is applied to the material. As will be explored in section 2.3.2, the ad-hoc method through which magnetostriction is introduced in many models predicts zero change in stiffness at zero magnetization and so they cannot assist in designing these magnetometers. A key focus of this dissertation will be on the many different assumptions inherent to existing models of magnetostriction and how they limit the validity of the models' final predictions.

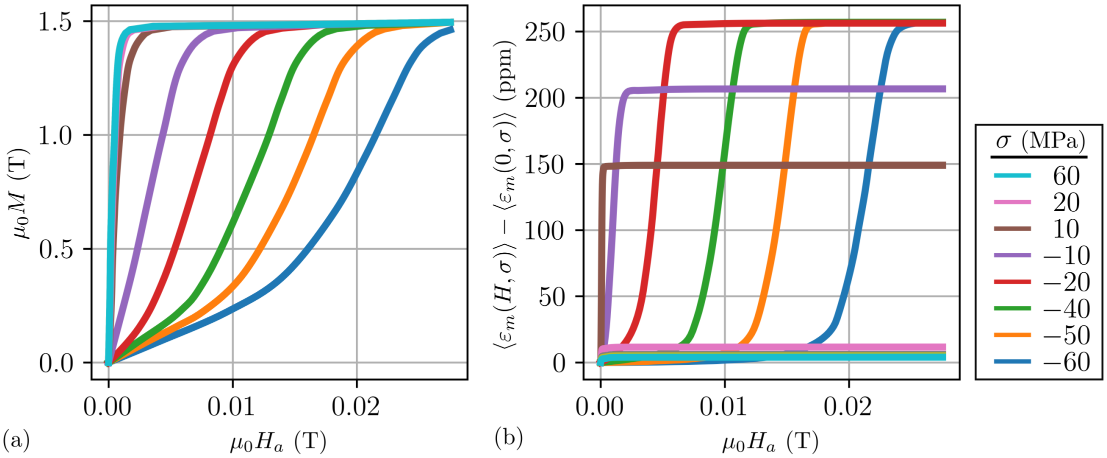

(a) (b)

Figure 1.2: Magnetization (a) and Magnetostriction (b) curves for $Fe_{79.1}Ga_{20.9}$ at varied applied stresses.

At this point it is worth establishing the main magnetostrictive material responses which constitutive models are attempting to simulate. The macroscale behavior of these materials is typically presented as magnetization $\boldsymbol{M}$ and magnetostriction $\boldsymbol{\varepsilon}^m$ curves at various applied magnetic fields $\boldsymbol{H}_a$ and stresses $\boldsymbol{\sigma}$. Figure 1.2 shows (a) $\boldsymbol{M} - \boldsymbol{H}_a$ and (b) $\boldsymbol{\varepsilon}^m - \boldsymbol{H}_a$ curves digitized from Mahadevan *et al.* [115]. Starting from the cyan line in the top left in Figure 1.2 (a) and traveling to the blue line in the bottom right the applied stresses go from tension to compression. Note that changes in the applied loads dramatically changes the susceptibility of the material and can introduce additional nonlinear regions to the magnetization. A key behavior observed in both Figure 1.2 (a) and (b) is that the magnetization and magnetostriction both saturate under increasing applied magnetic fields. A valid constitutive model of magnetostriction should be able to capture this highly-nonlinear behavior.

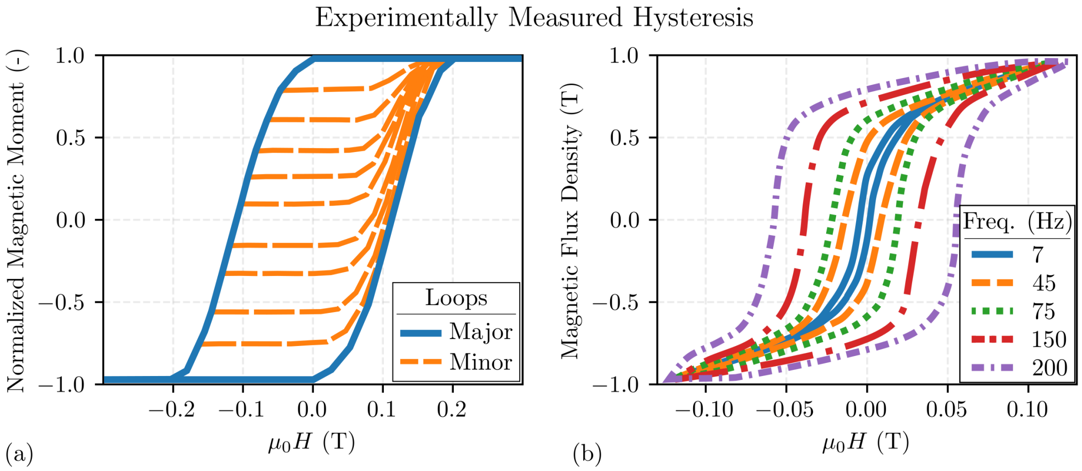

Figure 1.3: Experimentally measured behavior digitized from (a) da Col *et al.* [51] and (b) Talebian *et al.* [158] respectively.

Thus far the material responses presented have been anhysteretic or lossless. However, a defining feature of magnetic materials is hysteresis. Figure 1.3 shows experimentally measured hysteresis behavior digitized from da Col *et al.* [51] and Talebian *et al.* [158] respectively. Figure 1.3(a) shows the major and minor loops of nickel nanowires. Figure 1.3(b) shows the major hysteresis loop of the magnetostrictive material Terfenol-D under applied magnetic fields at varying frequencies. These two figures highlight that a material's specific magnetization can be reached in an infinite number of different ways depending on the history and dynamics of the applied magnetic field. Simulating this highly complicated response offers its own set of challenges even without introducing mechanics. The following section reviews the history of magnetostrictive materials and argues that an additional reason that modeling still requires further development is that, until relatively recently, the materials did not have significant practical application.

## 1.2 History of Magnetostrictive Materials

Even though magnetostriction was discovered over a century ago, accurately modeling the phenomena is still an ongoing area of research. There are several reasons for this aside from the inherent difficulties shown in the previous section. Firstly, interest in magnetostrictive materials has been limited as for most of their history the magnitude of their coupled response had little technological merit. Secondly, piezoelectric materials offered more significant responses that are easier to both model and control as compared to magnetostriction. This section will explore how magnetostrictive material development has improved but that modeling has understandably lagged behind.

The study of magnetostriction began in the 1840's when James P. Joule first measured the change in length exhibited by iron samples when magnetized with a magnetic field [93]. However, as these deformations were so minuscule (magnetostriction ≈1.2 ppm) it was believed they could not be used for practical applications [93]. For nearly one-hundred years there was little to no development in the field of magnetostriction. Conversely, piezoelectric materials, discovered in 1880 by brothers Pierre and Jacques Curie, were capable of producing far more significant strains (≈1000 ppm) [117]. The availability of highly capable piezoelectric materials drew focus away from the study of magnetostriction. The opinion on the practical use of magnetostriction changed in the 1960's when it was observed that at cryogenic temperatures rare earth materials were capable of much larger deformations.

In the early 1960's research to improve sonar technology motivated Clark, Bozorth, DeSavage, Rhyne, and Legvold to discover that rare-earth metals such as Terbium and Dysprosium exhibited large magnetostriction (≈10,000 ppm) at low temperature [43, 144]. By alloying Tb and Dy with elements that exhibit higher Curie temperatures, such as iron, these researchers at the US Naval Ordinance Laboratory produced materials that exhibit large magnetostriction at room temperature. Unfortunately, both alloys required extremely large magnetic fields to produce strain due to their large magnetocrystalline anisotropy (MCA). Luckily it was found that the MCA of these alloys had opposing signs and Clark combined them with the specific composition $Tb_{0.27}Dy_{0.73}Fe_2$. This alloy, named Terfenol-D, exhibits large magnetostriction (≈2000 ppm) under smaller magnetic fields [44, 143].

The next important milestone in magnetostrictive material research was the development of Galfenol. As Terfenol-D is brittle and has a low tensile strength [33] Clark *et al.* [46, 47] developed more robust iron gallium alloys at the Naval Surface Warfare center. The hardiness of iron gallium alloys increased its use in the development of smart structure devices [96, 97].

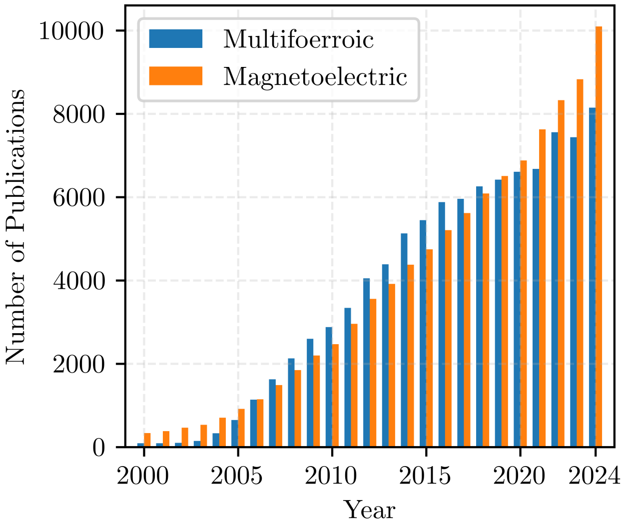

Figure 1.4: Number of articles reported in Google Scholar from 2000 to 2024 pertaining to “Multiferroic” and “Magnetoelectric”.

This interest magnetostrictive materials has only grown in recent years as their potential use in multiferroic materials has been recognized. Multiferroic materials couple at least two ferric orders (i.e., ferromagnetism, ferroelectricity, or ferroelasticity) and magnetostrictive materials can be used to create a multiferroic response by combining them with other materials in composite heterostructures. In 2001, Ryu *et al.* developed a laminated Terfenol-D/PZT/Terfenol-DME composite [145], allowing the magnetoelectric effect to be exploited at room temperature. Figure 1.4 illustrates how significant this event was for magnetoelectric laminates as the number of scientific publications and patents regarding them have increased between 2000 and 2024 according to Google Scholar. Magnetostrictive materials and their range of application continue to advance at an ever-quickening pace and modeling must improve to fully realize their potential benefits.

## 1.3 Statement of the Problem

Section 1.1 established that magnetostriction is a useful property that lends itself to advantageous applications, however this property is difficult to simulate. Furthermore, Section 1.2 showed that the material property was justifiably overlooked. Improvements to material design have renewed interest in accurate constitutive models. This thesis attempts to address that need by providing a framework for a unified model of magnetostriction.

There are numerous models in the current literature and while some have strong fundamental principles, others are a combination of inconsistent arbitrary equations. One of the main motivations behind this framework is the differences between the existing models cannot be readily compared in their current presentation. The individual assumptions and contributions of a model are often obfuscated, and this framework would allow the range of validity of their choices to be more easily evaluated. Finally, many of the existing models define behaviors that violate the laws of thermodynamics and this rigorous framework would ensure consistency.

## 1.4 Intellectual Merit

This dissertation offers several advances to the body of knowledge surrounding the field of magnetostriction. As previously stated, many existing models combine a plethora of smaller models without consideration for how these individual pieces interact with each other. One of the main reasons this issue arises is because the assumptions of each model are often not explicitly addressed in the literature. For example, a review article published in 2022 explores many varied types of magnetostrictive models and separates the nonlinear magnetostrictive models into two categories, anhysteretic and hysteretic [103]. Table 1.1 shows the subcategories of models that are included in the article. While the delineation between lossless and lossy models is logical, the subcategories of models do not clearly address their core differences.

Table 1.1: Kumar Review Article Model Groupings

| Anhysteretic | Hysteretic |
|---|---|
| Continuum Based | Stoner–Wohlfarth |
| Effective field based Langevin | Preisach |
| Armstrong | Play |
| Multiscale | Jiles–Atherton |
| Micromagnetic | Plasticity based |
|  | Multiscale |
|  | Armstrong |

Models found in the Effective field based Langevin, Armstrong, and Multiscale groups are all built using statistical mechanics. The core difference between these models is their definition of the internal energy of the system at the microscale. Understanding which micromagnetic energies were used in this initial definition makes the further deviations in the models (i.e., the need for mean field theory or numerical approximations) much more comprehensible.

An even larger grievance is that several models are arguably in the wrong categories all together. For example, it is possible for mean field theory models to predict hysteresis. Without knowing the particular or well-defined conditions that can influence the predictions of a model it cannot be used with any confidence to describe material behavior. Similarly, many researchers develop an anhysteretic model and introduce hysteresis by placing it in the larger Jiles-Atherton model. Understanding and quantifying the specific contributions of the new model is muddled as only the final combined results are typically presented. The creation of smaller models focused on addressing different phenomena (e.g., hysteretic or anhysteretic behavior) is a promising approach to more general models, and this framework seeks to establish an intuitive and consistent way to do so.

Even after establishing a thermodynamically consistent framework there is still the potential for a constitutive relation to predict spurious invalid behavior. Later chapters in this thesis will assert that a fully general 3D model of magnetostriction will require numerical approximations. A key finding in the work presented in Chapter 4 is that even a numerically accurate approximation of magnetostriction can produce artificial spurious responses that are thermodynamically inconsistent. Consequently, this work establishes several methods to help determine if a numerical approximation method is thermodynamically consistent. One such method is using a Legendre transform to ensure that the choice of independent variable does not influence the predictions of a model.

This thesis also examines a fundamental problem in applied mathematics, modeling the behavior of materials that display radically different, dominant behaviors at different length scales. While micromagnetic models are significantly accurate, it is often hard to bridge the microscale physics to the macroscale. Trying to model realistic materials with bottom-up strategies quickly becomes intractable and has led to the adaptation of statistical mechanics as an alternative strategy. This problem is referred to as the 'tyranny of scales' and solutions attempt to use knowledge of lower scale behaviors to determine which are inessential details and which directly influence the macroscale behavior of the materials. Ideally the methods employed by this work can be applied to other nonlinear and hysteretic materials.

Finally, many existing models of magnetostriction are phenomenological as they lack a rigorous thermodynamic background. Describing empirical relationships, these models often have limited ranges of validity and require large efforts in curve fitting. These simulations can be useful but a model capable of predicting material behavior is desired. To that end the models used in this unified framework will be developed using statistical mechanics. These continuum models allow for a more thorough understanding of the material behavior which ultimately benefits device design.

## 1.5 Broader Impacts

As magnetostrictive materials were developed their potential use in smart materials applications was recognized. For example, after its creation, researchers wanted to use Terfenol-D as a transducer. However, when operating at high frequencies the efficiency of the transducers due to internal loss generated by eddy currents. While attempts were made to mitigate these losses, including changing the manufacturing process and laminating the materials, evaluation of these attempts required prototypes which were very costly and time consuming. [152, 153]. This is a familiar story to magnetostrictive materials where in the lack of an accurate constitutive model hinders innovation. In addition to the knowledge base advancements presented in the previous section, the proposed framework enables several broad societal benefits, including the biomedical devices that improve patients' quality of life and economic and environmental savings in terms of more efficient power transformers.

Biomedicine is an emerging but rapidly growing application field for magnetostrictive sensors.

These devices enable the monitoring of physiological functions and medical treatments by measuring relevant stresses and translating them into detectable changes in magnetization. The main advantage of these devices iss that they are non-intrusive for several reasons. 1) they do not require an in-body power supply, 2) they do not require implanted connections, and 3) they do not interfere with physiological functionalities [79]. These non-intrusive features are especially appealing when it comes to treating bone fractures.

The total number of bone fractures reported in the United States ranges from 12 to 15 million per year [1]. This highly disabling condition is typically treated using fixation devices like bone plates. The healing state of the bone can be directly related to the amount of stress in the plate where the highest stresses are experienced during the early stages of fracture healing. When the bone is fully healed the plate must be removed. However if the plate is taken out prematurely, the bone will never mend completely and the risk of future fractures will increase. Furthermore, leaving the bone plate in for too long can make removal difficult as the bone will grow excessively after it has healed. Therefore, the ability to monitor the bone healing state is of great interest to both the patient and their doctor.

At present, periodical X-ray images are used to judge the bone healing state. Unfortunately, several studies have shown that X-ray images are not accurate enough to characterize bone strength or fracture repair with this method largely relying on a doctor's clinical experience. Non-intrusive magnetostrictive sensors provide a much more accurate measurement of stress thereby allowing bone plates to be removed at the proper time directly improving the quality of life of fracture patients.

Another field in which a magnetostrictive model would have significant benefits concerns power transformers. Amorphous magnetic materials have been widely used as a core material of power and solid-state transformers due to their availability, low cost, and high saturation flux density [118, 149, 166]. Additionally, amorphous metal distribution transformers (AMDTs) have low no-load losses, and their extensive use could have a considerable impact on global energy-saving efforts [122]. Table 1.2 summarizes the potential energy savings and reduction of $CO_2$ emissions in the major regions of the world [81] from using AMDTs over grain-oriented silicon steel transformers. An updated study by the same group in 2014 says that global losses were estimated to be worth $113 billion in 2011 and roughly 1056 million tons of $CO_2$-equivalent greenhouse gas emissions can be associated with these losses [6].

Table 1.2: Potential benefits from transformer efficiency improvements

| Country | Loss (TWh – $B) | Savings (TWh – $B) | CO Reduction (MT) |
|---|---|---|---|
| USA | 141 – 14.9 | 84 – 8.9 | 60 |
| EU-25 | 55 – 5.8 | 22 – 2.2 | 15 |
| Japan | 44 – 4.7 | 21 – 2.1 | 17 |

Unfortunately, the material properties that enable the ADMT related savings have their own cost. The magnetostrictive properties of ADMTs are much stronger than that of the cores they would be replacing (grain-oriented silicon steel) [18]. This becomes an issue as due to magnetostriction the cores of transformers and other high-power electric devices produce a low-pitched humming sound when oscillating AC currents generate magnetic fields [123]. The audible noise of power transformers has become an increasing environmental concern [190] and the switch to AMDTs will only exacerbate this issue. Overall noise pollution has already led governments to change legislation and introduce noise limits [78] and as rising energy demands tend to bring transformers closer to residential areas this will be a growing concern. Moreover, magnetostriction causes energy loss in these devices due to frictional heating in the ferromagnetic cores. This loss is responsible for wasted energy, and it can also reduce the lifespan of the transformer and require additional cooling. Hence, an accurate description of magnetostriction would allow for the design optimization of power transformers thereby maintaining a high-quality low living environment, removing megatons of $CO_2$ emissions from the atmosphere, and saving billions of dollars [102].

## 1.6 Conclusion

In the proposed dissertation, a unified macroscale constitutive model of magnetostriction will be derived in order to provide a consistent model suitable for use in high fidelity simulations. A reduced order model, derived using equilibrium statistical mechanics, will be used as basis for anhysteretic magnetostriction. The results of this anhysteretic model will be used to inform approaches to simulate the exchange interaction and multiple hysteresis mechanisms (static and dynamic). The goal is to provide constitutive frameworks reflecting the essential features such as saturation, nonlinear coupling, and thermodynamically consistent hysteresis.

The rest of this dissertation is organized into five chapters. The overview presented in this chapter will be followed by a deeper discussion of the problem statement and the phenomena of magnetism and magnetostriction needed to comprehend the contributions of this dissertation in chapter 2. In this same chapter a literature review will discuss the current state of the art models.

Chapters 3 and 4 are reproduced here from the original manuscripts published in 2022 in IOPscience's journal Multifunctional Materials and currently under review by IOPscience's Journal of Physics A respectively. In chapter 3, an analytic model of anhysteretic magnetostriction will be derived using equilibrium statistical mechanics. It will be shown how specific assumptions regarding the symmetry of key micromagnetic energies (magnetocrystalline, magnetoelastic, and Zeeman) reduce a general three-dimensional statistical mechanics model to a one-dimensional form with an exact solution. Additionally, a useful form of the analytic equations that ensures numerical accuracy will be provided. Furthermore, a comparison to experimental data performed for several magnetostrictive materials will show that the model accurately predicts the behavior of Terfenol-D while two different Iron Gallium alloys are modeled with varying accuracy.

In Chapter 4, an analysis of approximation methods for a two dimensional model of magnetostriction is presented. It is shown that a two-dimensional statistical mechanics model requires numerical approximation techniques, which take the form of quadrature methods in the existing magnetostrictive literature. The inherent assumptions of four approximation techniques are compared. The numerical accuracy for each method is presented, and the influence of this accuracy on the model's predictions is analyzed. The ability of the most accurate method to simulate experimental data from the literature is tested. Results show that when inaccurate numerical approximations are used the resulting constitutive models have degenerate/non-physical behaviors that limit their utility. Conversely, models with a consistent level of numerical accuracy are capable of predicting the behavior of magnetostrictive materials but their computational efficiency is reduced.

In chapter 5, the preliminary work for deriving a thermodynamically consistent model of magnetostriction hysteresis is presented. Much like the anhysteretic models, the laws of thermodynamics present the general relationship between potentials and conjugate work variables. In the non-equilibrium formalism a pseudo-potential of dissipation is defined and relations the irreversible change to the evolution of internal state variables. Existing hysteresis models will guide the development of the irreversible constitutive relationships.

Finally, in Chapter 6, the presented work is summarized and open ended questions that require future study are discussed.

# Chapter 2

# Background

This chapter provides the necessary background information needed to understand the novel work presented in later chapters. It begins with identifying where the need for constitutive laws arises from a mathematical perspective. This is followed by a discussion on the origin of magnetism, magnetization, and hysteresis, each of which will guide the development of the constitutive laws. Finally, a thorough review of the existing magnetic and magnetostriction models is presented so that the specific necessary improvements to the field can be distinguished and emphasized.

## 2.1 Problem Definition

The need for the proposed work can be identified by reviewing the fundamental mathematics and physics needed to model any material. The set of equations needed to fully define a material system are typically divided into four groups. These groups are the governing equations, boundary conditions, auxiliary relations or compatibility expressions, and constitutive laws.

As this work is focused on coupling mechanics and magnetism the relevant governing equations are Cauchy's equations of motion and Maxwell's equations. The mechanical balance law of the body is the Cauchy momentum equation,

$$\nabla \cdot \boldsymbol{\sigma} = \rho \ddot{\boldsymbol{x}}, \tag{2.1}$$

where $\rho$ is the mass density, $\boldsymbol{x}$ is the displacement vector. The second set of governing equations are Maxwell's equations. Maxwell's equations offer a description of electromagnetic fields, relating the following quantities, magnetic flux density ($\boldsymbol{B}$) and its work conjugate magnetic field ($\boldsymbol{H}$), while the electrical variables are electric flux density ($\boldsymbol{D}$), its work conjugate - electric field ($\boldsymbol{E}$), and current density ($\boldsymbol{J}$), like so,

$$\nabla \cdot \boldsymbol{B} = 0 \tag{2.2}$$

$$\nabla \cdot \boldsymbol{D} = \rho_e \tag{2.3}$$

$$\nabla \times \boldsymbol{H} = \boldsymbol{J} + \dot{\boldsymbol{D}} \tag{2.4}$$

$$\nabla \times \boldsymbol{E} = -\dot{\boldsymbol{B}}, \tag{2.5}$$

where $\rho_e$ is the free electric charge density. These equations can be simplified placing a static constraint on the system. This constraint excludes both electric terms and the time derivative terms in the magnetostatic limit simplifying Maxwell's equations to:

$$\nabla \cdot \boldsymbol{B} = 0 \tag{2.6}$$

$$\nabla \times \boldsymbol{H} = 0 \tag{2.7}$$

To solve the governing equations constraints are placed on them in the form of boundary conditions. For a mechanical body the boundary conditions are the traction conditions where the traction vector $\boldsymbol{T}^{(\hat{\boldsymbol{n}})}$ characterizes the pressure applied to a surface, (i.e., a projection of the stress tensor $\boldsymbol{\sigma}$ onto the surface normal $\hat{\boldsymbol{n}}$),

$$\boldsymbol{\sigma} \cdot \hat{\boldsymbol{n}} = \boldsymbol{T}^{(\hat{\boldsymbol{n}})} = 0 \tag{2.8}$$

For a magnetic body the boundary conditions are placed on the two magnetic fields $\boldsymbol{B}$ and $\boldsymbol{H}$,

$$[\![\boldsymbol{B}]\!] \cdot \hat{\boldsymbol{n}} = 0 \tag{2.9}$$

$$[\![\boldsymbol{H}]\!] \times \hat{\boldsymbol{n}} = 0, \tag{2.10}$$

in which the normal component of $\boldsymbol{B}$ and tangential component of $\boldsymbol{H}$ are continuous across the boundary. These conditions hold so long as there are no surface currents and are operating in the magnetostatic limit.

To fully determine the system of equations the auxiliary relations further define certain quantities. These equations include the strain displacement $\boldsymbol{x}$ relation,

$$\boldsymbol{\varepsilon} = \frac{1}{2}(\nabla \boldsymbol{x} + \nabla \boldsymbol{x}^t), \tag{2.11}$$

and the definition of the magnetic scalar potential $\varphi_m$,

$$\boldsymbol{H} = -\nabla \varphi_m. \tag{2.12}$$

The final set of equations necessary to define the system are the constitutive laws. Constitutive laws describe the relationship between the fields and the material medium, and arise from thermodynamic constraints. The derivation of constitutive laws usually begins by expressing the specific internal or free energy, specific entropy, and heat flux of a material in terms of the temperature, parameters characterizing shape changes, and any internal state variables (such as yield stress) that characterize the material state. The goal of this work is to define the functional dependence of magnetization and magnetostriction on applied magnetic fields and stresses (i.e., $\boldsymbol{M}(\boldsymbol{H}_a, \boldsymbol{\sigma})$ and $\boldsymbol{\varepsilon}^m(\boldsymbol{H}_a, \boldsymbol{\sigma})$).

### 2.1.1 Thermodynamics

The following derivation will begin with a summary of the principal thermodynamic relations valid for a generic system with homogeneous properties, later the description will be specialized for magnetostriction. The first law of thermodynamics expresses the conservation of energy and states that, under a generic transformation where work $\delta W$ is performed on the system and heat $\delta Q$ is absorbed by it,

$$dU = \delta W + \delta Q \tag{2.13}$$

where U is the internal energy, $\delta$ denotes dependency on the path, and $d$ represents an exact differential and is used for state path-independent variables. It is assumed that the work $\delta W$ can be expressed in terms of two appropriate conjugate work variables $\mathbb{S}$ and $\mathbb{F}$, according to the expression

$$dW = \mathbb{S} d\mathbb{F} \tag{2.14}$$

$\mathbb{F}$ is a state variable, describing some property of the system, and $\mathbb{S}$ characterizes the external action exerted on the system.

The second law of thermodynamics introduces a second state function, the entropy $S$, which, given any reversible or irreversible transformation, always satisfies the inequality,

$$dS \geq \frac{\delta Q}{\Theta}. \tag{2.15}$$

where temperature $\Theta$ and $\mathbb{S}$ are intensive variables that do not depend on system size, whereas $S$ and $\mathbb{F}$ are extensive variables that scale proportionally system size such as total volume or mass.

While it is the final goal to develop a hysteretic model this cannot be done without non-equilibrium thermodynamics. This overcomplicates the current derivation and so the following derivation will assume the system is always in equilibrium,(i.e., developing a constitutive law for anhysteretic magnetostriction). To restrict the system to equilibrium reversible processes the second law is constrained to,

$$\Theta dS = \delta Q. \tag{2.16}$$

Substituting this into the first law produces the fundamental thermodynamic relation,

$$dU = \mathbb{S} d\mathbb{F} + \Theta dS \tag{2.17}$$

Equation (2.17) yields expressions, known as equations of state, for various thermodynamic parameters in terms of the derivatives of the thermodynamic potentials,

$$\left[\frac{dU}{d\mathbb{F}}\right]_{dS} = \mathbb{S}, \qquad \left[\frac{dU}{dS}\right]_{d\mathbb{F}} = \Theta. \tag{2.18}$$

The subscripts denote that these thermodynamic transformations are constrained, in this case with constant entropy and generalized state variable (e.g., magnetization).

The thermodynamic potentials are state functions that dictate how the system evolves, and the four common potentials are the internal energy $U(\mathbb{F}, S)$ the enthalpy $E(\mathbb{S}, S)$, the Helmholtz free energy $F(\mathbb{F}, \Theta)$, and Gibbs free energy $G(\mathbb{S}, \Theta)$. Each of these potentials can be related to one another through Legendre transforms, which allows one to choose the desired independent variables of their system. The work presented in this thesis uses the Gibbs free energy as it is easier to control $\mathbb{S}$, which includes the applied magnetic fields and stresses, and temperature in real world experiments than it is to control magnetization, strain, and entropy.

To specialize these thermodynamic relations for magnetostriction the work can be defined for magnetism and mechanics as,

$$dW = \mu_0 \boldsymbol{H_a} d\boldsymbol{M} + \boldsymbol{\sigma} d\boldsymbol{\varepsilon} \tag{2.19}$$

where $\mu_0$ is the permeability of free space. Note that this specific definition of magnetic work was chosen as the field doing the work is one that is easy to experimentally control and results in a change in the magnetization of the body instead of a change in the magnetic flux density in all of free space. Derivations for this definition of work can be found in numerous textbooks including those by Bertotti [24] and Coey [49]. Additionally, by performing Legendre transforms such that the Gibbs Free energy is the chosen thermodynamic potential, and magnetic and mechanical work are suitably defined the following equations of state are produced:

$$\left[\frac{-1}{\mu_0}\frac{\partial G}{\partial \boldsymbol{H}_a}\right]_\Theta = \boldsymbol{M}(\boldsymbol{H}_a, \boldsymbol{\sigma}), \qquad \left[\frac{-\partial G}{\partial \sigma}\right]_\Theta = \boldsymbol{\varepsilon}^m(\boldsymbol{H}_a, \sigma). \tag{2.20}$$

These expressions can be used to derive the system constitutive law, once the thermodynamic potentials are defined. The proposed laws should mimic the phenomenological behavior of the material and if possible should be based on the physical processes that govern the response of the system. Section 2.2 will explore the magnetization and magnetostriction at the atomic, microscopic, and mesoscopic levels to guide this development.

### 2.1.2 Non-Equilibrium Thermodynamics

At this point it is worth reintroducing the concept on non-equilibrium thermodynamics. In order to use the previously presented thermodynamic equations while not in equilibrium it is assumed that each volume element of the system is in local thermodynamic equilibrium. This assumption asserts that the local states of a non-equilibrium system can be described in terms of thermodynamic fields which are continuous functions of space and time. The hypothesis of local equilibrium is explicitly stated as a basic assumption in classical non-equilibrium thermodynamics [57, 80, 100].

The local form of the first law can be written as follows:

$$\rho \dot{u} = \dot{\boldsymbol{W}} + \dot{\boldsymbol{Q}} \tag{2.21}$$

where $u$ is the internal energy density. Once again, the work $\dot{\boldsymbol{W}}$ can be expressed in terms of two appropriate conjugate work variables $\mathbb{s}$ (a generalized force) and $\mathbb{f}$ (a generalized displacement). The heat flow of the system is described by the divergence of heat flux vector $\boldsymbol{q}$ and an internal heat source per unit mass $r$. The local form of the first law of thermodynamics can be expanded as

$$\rho \dot{u} = \mathbb{s} \cdot \dot{\mathbb{f}} - \nabla \cdot \boldsymbol{q} + r. \tag{2.22}$$

The local form of the second law can be written as follows:

$$\mathcal{H} = \dot{\mathcal{S}} - \mathcal{J} \tag{2.23}$$

where $\mathcal{H}$ is the net entropy production, $\mathcal{S}$ is the net internal-entropy, and $\mathcal{J}$ is the entropy flow of the system. The net internal-entropy is dependent on the specific entropy scalar field $\eta$ and the mass density $\rho$. Also, the entropy flow can be defined analogously to the heat flow and is characterized by an entropy flux $\boldsymbol{J}$ and an entropy supply $j$. The heat flow and entropy flow are related such that

$$\boldsymbol{J} = \frac{\boldsymbol{q}}{\Theta} \quad \text{and} \quad j = \frac{r}{\Theta} \tag{2.24}$$

Using the previous definitions the local entropy imbalance is

$$\rho\dot{\eta} + \nabla \cdot \frac{\boldsymbol{q}}{\Theta} - \frac{r}{\Theta} = \Gamma \geq 0 \tag{2.25}$$

where $\Gamma$ is net entropy production density. Combining the first and second laws produces the following free energy imbalance:

$$\rho(\Theta\dot{\eta} - \dot{u}) + \mathbb{s} \cdot \dot{\mathbb{f}} - \boldsymbol{q} \cdot \frac{\nabla\Theta}{\Theta} = -\Theta\Gamma \leq 0 \tag{2.26}$$

From this point forward a dissipation or entropy production of the system needs to be defined. Once again, the proposed dissipation potential should simulate the phenomenological loss behavior of the material, the details of which will be provided in Section 2.2.2. The focus of Chapter 5 is on defining the evolution of dissipation using internal state variable theory (ISV).

## 2.2 Fundamental Phenomenological Behaviors

In this section the background physics of magnetism and magnetostriction are established to guide the constitutive laws that are developed, beginning with the origins of atomic magnetism. The magnetism of materials is a quantum effect originating at the atomic level. At the atomic scale valence band electrons have orbital motion around the nucleus. As this motion is analogous to a small current it creates a small magnetic moment, following Ampère's Law (one of Maxwell's equations). An additional magnetic moment is generated from the intrinsic spin (angular momentum) of the electron itself. Of note the magnitude of the total magnetic moment $\mu$ is constant.

At a length scale large enough for the atomic structure of the material to be ignored, a magnetic medium is modeled as a collection of magnetic moments contained within a volume $V$. The magnetization can then by defined as the magnetic moment per unit volume,

$$\boldsymbol{M} = \lim_{V \to 0} \frac{\sum \mu}{V}. \tag{2.27}$$

At this continuum scale the magnetization also has a constant magnitude and so the quantity of interest is magnetization direction cosines or unit vector $\boldsymbol{m}$,

$$\boldsymbol{M} = M_s \boldsymbol{m} \tag{2.28}$$

$$|\boldsymbol{M}| = M_s \tag{2.29}$$

where $M_s$ is the saturation magnetization.

### 2.2.1 Domains and Micromagnetic Energies

At the micron size scale, it is observed that magnetic medium breaks into a domain structure. Figure 2.1 ($a$) shows a Magneto-Optic Kerr Effect (MOKE) image of a magnetic film [155]. The shaded regions in this image represent the magnetic domains, the size, number, and orientation of which is governed competing micromagnetic energy densities. The energies typically included in magnetostrictive models are Exchange, Magnetocrystalline Anisotropy, Magnetoelastic. Magnetostatic, and Zeeman energy each of which will now be defined. Exchange is the quantum mechanical interaction that occurs when electron orbitals 'overlap' and can cause atoms to exchange electrons. The energy cost of exchange is dependent on the relative orientation of spins of two electrons. In ferromagnetic materials exchange aligns spins to be parallel. This effect is short range and typically influences nearest, or next-nearest, neighbors. Exchange is given by:

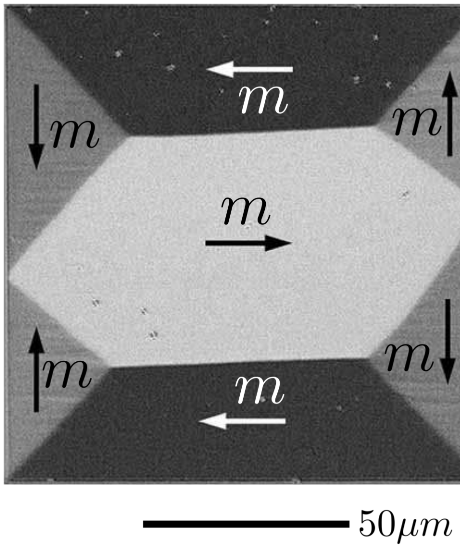

Figure 2.1: Domain pattern from a permalloy film imaged using MOKE microscopy [155].

$$f_{EX} = -\mu_0 \int_{\Omega_i} A \cdot (\nabla \boldsymbol{m})^2 dV \tag{2.30}$$

where $A$ is referred to as the exchange stiffness constant.

Magnetocrystalline anisotropy is due to interactions of the magnetization with the hosting crystal lattice. Based on the crystallographic orientation of a grain, certain axes are preferred by these domains within the grain, and these axes are referred to as easy axes. This effect once again occurs due to complex quantum interactions and so the micromagnetic definition of MCA energy is a phenomenological energy term derived using a Taylor series expansion of the free energy. A general formula that describes this magnetocrystalline anisotropy behavior is given by:

$$f_{MCA} = \int_{\Omega_i} K_{ij} m_i m_j dV \tag{2.31}$$

where the MCA coefficients in anisotropy tensor $K_{ij}$ should have the same symmetry as the crystal being modeled and repeated indices are summed over from 1 to 3.

Magnetoelastic anisotropy is defined as the perturbation of other anisotropy energies. This is intuitive as deforming the crystal (which interacts with magnetization) should change the equilibrium state of the micromagnetic energy. The magnetoelastic anisotropy is given by:

$$f_{ME} = \int_{\Omega_i} B_1 \sum_i (m_i^2 - \frac{1}{3})\varepsilon_{ij} + B_2 \sum_{i \neq j} m_i m_j \varepsilon_{ij} dV \tag{2.32}$$

where $B_1$ and $B_2$ are the magnetoelastic coupling constants. Of note the 1/3 term is included as this energy describes Joulian magnetostriction which is volume conserving.

The magnetostatic or self-demagnetization energy depends on the external field $H_m$ produced by the magnetization of a body. This energy is dependent on the physical shape of the body and favors magnetization configurations that minimize to average magnetization of the body.

This energy is expressed as the gradient of magnetic potential.

$$f_D = -\frac{\mu_0}{2} \int_{\Omega_i} M_s \boldsymbol{H}_M \cdot \boldsymbol{m}.dV \tag{2.33}$$

Finally, in addition to the internal mechanics described above, the magnetization is coupled to the external field. The Zeeman energy favors when magnetization that is parallel to the applied field.

$$f_Z = -\mu_0 \int_{\Omega_i} M_s \boldsymbol{H}_a \cdot \boldsymbol{m} dV \tag{2.34}$$

### 2.2.2 Domain Evolution

The macroscale response of magnetostrictive materials is directly tied to the evolution of the domain structure. Figure 2.2 shows how an applied magnetic field influences magnetic domains and how their averaged response determines the macroscale magnetization.

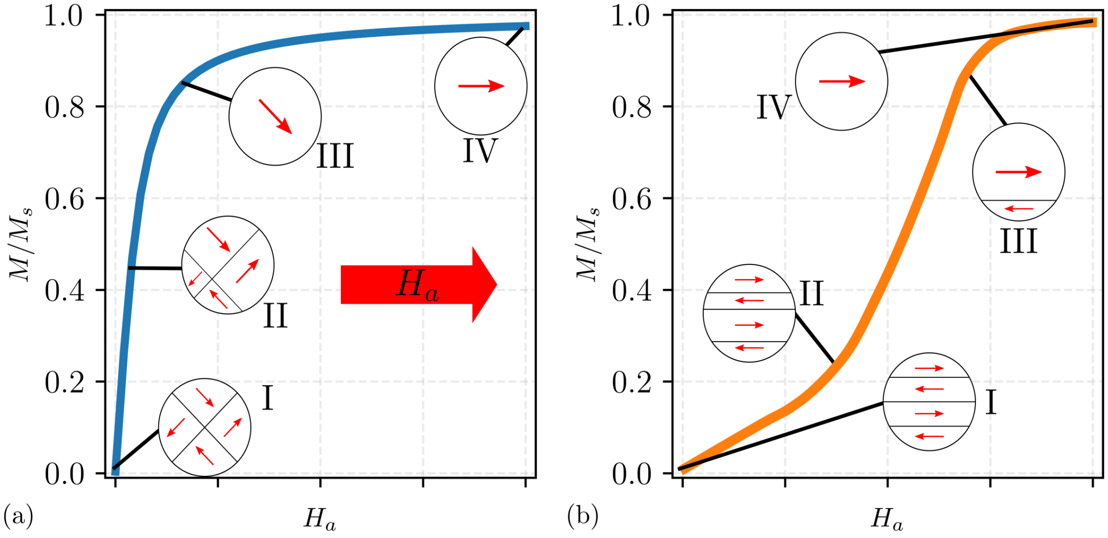

Figure 2.2: Domain evolution in a magnetic field without (a) and with (b) an applied stress.

Figure 2.2 (a) shows a macroscale magnetization curve, with inset representative snapshots of approximate domain structures that occur at several points along the curve. A clear link between the microscopic image and the macroscale response is highlighted in these snapshots. For example, the orientations $\boldsymbol{m}$ shown in inset I of Figure 2.2 (a) have a vector sum of zero, resulting in no net macroscale magnetization. By then applying an external magnetic field $\boldsymbol{H}_a$, the domains that are aligned with the field will begin to grow, as shown in inset II of Figure 2.2 (a). Inset III of Figure 2.2 (a) shows that domains aligned with the field will continue to grow as the magnitude of the external magnetic field increases, until only a single domain remains. Finally, the domain will rotate until it is parallel to the applied field and the material saturates, as shown in inset IV of Figure 2.2 (a). Figure 2.2 (b) shows a similar process as shown in Figure 2.2 (a), however an applied stress changes the initial domain structure and so influences the saturation process. Figure 2.2 highlights that the macroscale response of these materials is dictated by mechanisms occurring at the micro and mesoscale. The specific influences of stress and material symmetry on the magnetization process are explored further in Chapter 3.

While Figure 2.2 only showed anhysteretic behavior it is widely understood that hysteresis is also directly related to the properties of the free energy of the system. The competition of the micromagnetic energies creates complex free energy term that is capable of having multiple local energy minima. Hysteresis occurs when the system is trapped at these local energy minima and cannot reach thermodynamic equilibrium. The local energy minima can be caused by three types of phenomena, interaction between domains, anisotropy energies and internal frictional type pinning forces caused by interstitial dislocations and impurities. As external applied fields and stresses irreversibly change the structure of the magnetic domain the system spontaneously jumps to new stable configurations. This jumping mechanism is known as the Barkhausen effect.

The other prominent source of hysteresis or loss in magnetic system is eddy currents. Eddy currents are generated by domain wall motion in an analogous process to how moving electrical charges generate magnetic fields. These currents are a dissipation mechanism as they generate heat. Eddy current losses are typically separated into two groups, classical and anomalous or excess loss. Classical loss is dependent on the shape and geometry of the system and can be accurately described using Maxwell's equations. The anomalous or excess loss arises from the eddy currents surrounding the active domain walls in motion. Both of these losses are dependent on frequency and are therefore rate-dependent processes, however their dependence on frequency varies. The different space and time scales that each of the sources of hysteresis occur at allows total loss to be described by distinct general laws. This loss separation is advantageous when developing hysteretic models of magnetostriction.

This section presented the microscale phenomena that occur in magnetostrictive materials and dictate their macroscale behavior. The following section will explore the different models that have attempted to simulate magnetostriction. Statistical mechanics offers a logical way to bridge the microscale physics to the macroscale but there are still different considerations that can be made that dramatically influence the validity of a model's predictions. The following section provides a review of the more prolific models and highlights some of their limitations that this thesis aims to address.

## 2.3 Previous Constitutive Models

This section will explore the existing models of magnetostriction. It is broken into three sections, first it is worth noting that micromagnetic models accurately describe these materials but are limited to small size scales. Recognizing this accuracy should motivate macroscale models to retain as much relevant information about the microscale while still remaining computationally efficient. Next, anhysteretic models are reviewed and it is highlighted that depending on the size scale that mechanics are introduced to the model can dramatically limit their range of validity. Finally hysteretic models, which can be broken up into two groups phenomenological and continuum (i.e., the Jiles-Atherton and plasticity-based models). Chapter 5 offers more detailed descriptions of the two sets of continuum models.

### 2.3.1 Micromagnetic Models

Micromagnetic models minimize a free energy term comprised of each of the relevant micromagnetic energies. This variational theory of micromagnetics was originally proposed by Brown [31, 32, 32] and serves as the gold standard for magnetic and magnetostrictive modeling at this size scale [52, 71, 72]. However, these models require mesh sizes on the order of 5-10 nm (i.e., on the order of exchange length) to model magnetic domain walls. This restricts the geometry sizes that can be efficiently modeled, typically to below 10 cubic microns [19, 86, 112, 113, 174]. This lack of accurate constitutive models above tens of cubic microns and for frequencies up to tens of megahertz has impaired the development of new strain-mediated magnetoelectric technologies. The goal of the proposed work is therefore to efficiently relate the well-defined microscale physics of these materials to the macroscale.

### 2.3.2 Anhysteretic Models

This subsection reviews models that predict anhysteretic curves. Anhysteretic magnetization and magnetostriction refers to the equilibrium state of the material. These idealized curves represent lossless processes without dependence on history. The two major approaches for modeling anhysteretic behavior are to define the constitutive laws using either a polynomial series expansion or statistical mechanics. The statistical mechanics models can be further subdivided by which micromagnetic energies are included in the Landau Free energy.

Polynomial series expansions of either the Helmholtz or Gibbs free energy are straightforward to utilize once the expansion coefficients (i.e., material properties) are identified [35, 170]. However, conducting the requisite number of experiments to measure the expansion coefficients can be technically challenging and costly. Furthermore, finite expansions are incapable of capturing the saturating behavior inherent in magnetic phenomena. As a result, the use of polynomial models must be accompanied by knowledge of their bias conditions and limited range of validity.

Existing statistical models of magnetostriction often assume zero exchange coupling (i.e., paramagnetic behavior), to derive more computationally efficient models [15, 68, 154, 169]. The Brillouin and Langevin functions are both statistical models of paramagnetism in which they have defined their Landau free energy with only the Zeeman energy. The Brillouin function assumes that magnetization direction cosines $\boldsymbol{m}$ are constrained to only point up and down (i.e., mimicking spins), while the Langevin function allows the magnetization direction cosines to point in any direction on the unit circle. The statistical mechanical basis of these models allows them to predict saturation which has led to their continued adaptation through ad-hoc assumptions and procedures in an attempt to predict more complicated behaviors.

To adapt paramagnetic models to predict ferromagnetism macroscale models often use mean field theory (MFT) to approximate the effects of the exchange interaction. MFT assumes that each magnetic moment experiences an effective field that is the average influence of all other magnetic moments in the system (i.e., each spin interacts equally with all other spins, not just nearest neighbors). This effective field is defined as

$$H_e = \alpha M \tag{2.35}$$

where $\alpha$ approximates inter-domain coupling. Reducing the complexity of the exchange interaction to a single phenomenological parameter serves as a simple and effective method to study how the exchange interaction can introduce effects of hysteresis by bifurcating the single well free energy describing paramagnetism into a multi-well landscape with multiple energy minima [24, 41, 49, 50]. This leads to the prediction of spontaneous net magnetization, even with zero external magnetic field. Despite the advantages of MFT, it is not able to accurately reproduce some mechanical behaviors occurring at the domain level. Notably, having this effective field dependent on the average magnetization and a constant does not properly account for all magnetoelastic effects.

Paramagnetic models introduce mechanics using the same MFT approach, by assuming micromagnetic expressions for magnetostriction are valid at the macroscale. This method will be referred to as 'Langevin magnetostriction'. An example of this approach is to assume magnetostriction $\boldsymbol{\varepsilon_m} \propto \boldsymbol{M} \otimes \boldsymbol{M}$, with $\boldsymbol{M} = M_s \mathcal{L}(\boldsymbol{h})\hat{\boldsymbol{h}}$ where $\mathcal{L}$ is the Langevin function depending on the reduced magnetic field $\boldsymbol{h}$ [111, 148]. While Langevin magnetostriction provides a path to incorporating saturating behavior and magneto-mechanical coupling, it also introduces inconsistencies compared to experimental observations, and more advanced models (e.g., micromagnetics). One large inconsistency introduced by Langevin magnetostriction concerns the $\Delta E$ effect. Consider that when $\boldsymbol{H} = 0$ an anhysteretic constitutive model predicts $\boldsymbol{M} = 0$, and therefore the assumptions above identically produce zero macroscopic magnetostriction $\boldsymbol{\varepsilon_m} = 0$. However, magnetic domains are easily controlled with stress $\boldsymbol{\sigma}$ at zero magnetic field, which is exemplified in numerous experimental studies that observe the peak $\Delta E$ effect occurs when $\boldsymbol{H} = 0$ [54, 55, 87]. As a reminder an initial assumption of these paramagnetic models is that the Landau free energy only contains Zeeman energy (e.g., no dependence on mechanics). The next branch of models instead populates the Landua free energy with both MCA and magnetoelastic anisotropy.

By including the relevant micromagnetic energies in the Landau free energy statistical mechanic models can potentially model paramagnetic, ferromagnetic, ferrimagnetic, and antiferromagnetic materials with arbitrary anisotropy energies, and even account for polycrystalline materials [24, 41]. However, accurately solving these models can require computationally expensive numerical integration which greatly restricts their use in numerical simulations like finite element models. Improving the computational efficiency of these models has been the focus of recent research that has shown an excellent ability to fit these models to experimental data [13, 15, 66, 67, 68, 69]. These computationally efficient models are derived using common simplifying assumptions including zero exchange coupling (i.e., paramagnetic behavior) [15, 68, 154, 169], and simplified magnetocrystalline anisotropies [67, 68, 69, 169]. Chapter 3 and its associated Appendix A show how the assumptions of these models can restrict them to modeling only specific material compositions and that their numerics influence the behavior of the material (i.e., lead to numerically induced anisotropies). Additionally, Chapter 4 shows that even under many simplifying assumptions these models may require numerical simulation.

### 2.3.3 Hysteretic Models

There is a plethora of different models for macroscale magnetic hysteresis that are derived in significantly varied ways. As has been established the macroscale response of the materials is highly dependent on the evolution of the microscale physics. Macroscale descriptions often reduce the number of degrees of freedom which in turn can weaken a model's physical consistency, which can serve as a method to categorize these models. Models with less consistency are typically classified as phenomenological. Phenomenological models include the Preisach, Prandtl-Ishlinskii, neural networks, and deep learning techniques [4, 5, 83, 171]. The Preisach model is one of the earliest models of hysteresis and is based on an operator known as a hysteron which takes the values of ±1 depending on the field values applied to the model and the history of these fields. The simplicity of this model and its accuracy led to many modifications for use in magnetostrictive modeling and control. Despite these appealing qualities, phenomenological models are often very reliant on curve fitting to large experimental data sets, and place less emphasis on the underlying micro and nanoscale physics. As the goal of this dissertation is to construct a macroscale predictive model of magnetostriction based on the microscale physics, these predominately numeric approaches will not be discussed in later chapters.

A common practice for continuum hysteresis models is to develop an anhysteretic model that hysteresis is then introduced to. The most popular of these approaches is the Jiles-Atherton (JA) model, which introduces hysteresis in terms of a first-order differential equation. A major component of the JA model is the decomposition of magnetization $\boldsymbol{M}$ into reversible $\boldsymbol{M}^{rev}$ and irreversible $\boldsymbol{M}^{irr}$ components. Both of these terms are then related to the anhysteretic magnetization $M^{an}$. In the original model and many of its derivatives the definition of anhysteretic magnetization is the Langevin function. Note that there are several thermodynamic inconsistencies inherent to the original JA model. Ad hoc revisions have been made to the model to address issues including, the occurrence of negative slopes in minor loops [36], that setting $M^{irr} = M^{an}$ does not result in a lossless curve [40, 167], and that loss or dissipation is not positive at all instances in the magnetization process (i.e., violating the second law of thermodynamics) [151].

Another branch of modeling magnetic hysteresis recognizes the similarity between ferromagnetic behavior and plasticity in mechanical problems [84, 85]. The thermodynamic framework with which these models are built inherently addresses many of the inconsistencies of the JA model. However, as many of these models are analogous to those developed for plasticity, they do not properly address intermediate results, only the final result. At this point it is worth highlighting that like the JA model this non-equilibrium framework requires an anhysteretic model. Often these plasticity models have overly simplified anhysteretic models (i.e., ones that do not predict saturation) and so the hysteretic part of the model is made more complex to simulate the behavior in Figure 5.1 [39, 74, 157]. Chapter 5 will show how a general thermodynamic framework allows for a saturating anhysteretic model of magnetostriction which in turn should reduce the complexity of the required hysteretic model.

# Chapter 3

# Nonlinear One-Dimensional Constitutive Model for Magnetostrictive Materials

## Attribution

This chapter, a collaborative work with John P. Domann, was originally published in Multifunctional Materials in 2022.

## Author Contributions

Imhof and Domann conceived of the project. Imhof was responsible for developing the constitutive model and implementing it in code, verified the numerical accuracy of the model and compared the model to experimental data. Imhof also prepared the initial draft of the manuscript and its associated visuals and coordinated the revisions. All of this was done with supervisory assistance from Domann, who also reviewed and edited the work at all stages until publication.

## 3.1 Introduction

Magnetostrictive materials enable the use of numerous technologies including energy harvesters, ultrasonic transducers, vibration dampers, and even novel antennas [42, 56, 59, 61, 104, 110, 126, 172, 173, 186]. These materials intrinsically couple a material's magnetic and mechanical degrees of freedom, allowing the magnetization $\boldsymbol{M}(\boldsymbol{H}, \boldsymbol{\sigma})$ and magnetostriction $\boldsymbol{\varepsilon_m}(\boldsymbol{H}, \boldsymbol{\sigma})$ to be described as a function of the magnetic field $\boldsymbol{H}$ and stress $\boldsymbol{\sigma}$ (or total strain $\boldsymbol{\varepsilon}$). However, it is difficult to accurately model the strongly coupled nonlinear magneto-mechanical constitutive response of these materials at the macroscale. The lack of an accurate non-linear magnetostrictive constitutive model has likely inhibited the design of novel magnetostrictive technologies.

There are numerous models of macroscale magnetostriction. These models aim to capture several key features including hysteresis loops and the influence of magnetostriction on these loops. These models can generally be described as either phenomenological models with numerous parameters that need to be curve fit to experimental data, or statistical models. The ultimate goal of utilizing statistical models is to build macroscale models from well-defined microscale physics (i.e., micromechanics). One of the earliest phenomenological models is the Preisach model which inherently captures hysteretic behavior through the use of hysterons [4]. While the Preisach and other curve fitting approaches (i.e. Prandtl-Ishlinskii, neural network, and deep learning models) [5, 83, 171] offer robust ways to model experimentally observed magnetostrictive behavior, in practice they are very reliant on curve fitting to large (i.e., costly) experimental data sets, and place less emphasis on the underlying micro and nanoscale physics compared to models that leverage statistical mechanics.

Statistical models of magnetization commonly model the anhysteretic and hysteretic behavior of materials separately. Anhysteretic curves correspond to the lowest possible energy state of the system or equilibrium positions. Of note, this anhysteretic behavior can be experimentally measured and so the accuracy of an anhysteretic model can be rigorously tested. Hysteretic curves represent the metastable equilibrium points that a material can reach and are dependent on the previous states of the material. This dependence on the material's history makes hysteretic curves path dependent and harder to model. Furthermore, after an anhysteretic model is built it is common to introduce hysteresis through other approaches such as the Jiles-Atherton model [91].

Figure 3.1 schematically illustrates two potential anhysteretic magnetization curves $\boldsymbol{M}(\boldsymbol{H},\boldsymbol{\sigma}_0)$ at fixed stress $\boldsymbol{\sigma}_0$. Two commonly encountered behaviors are highlighted. Type I curves are concave down until saturation, while Type II curves transition from concave up to concave down between demagnetization and saturation (i.e., they show sigmoidal behavior). Type I curves are commonly seen in materials like Terfenol-D ($\mathrm{Tb}_{0.3}\mathrm{Dy}_{0.7}\mathrm{Fe}_{19.2}$) [115, 188], while Type II curves are encountered in some compositions of Galfenol (e.g., $\mathrm{Fe}_{81.6}\mathrm{Ga}_{18.4}$) when placed in compression [115]. The specific MH curve displayed by a given material is strongly dependent on its crystalline structure in addition to any externally controlled anisotropies, like an applied stress. Three common approaches to capture the behaviors seen in Figure 3.1 are to either 1) construct polynomial series expansions, 2) assume a modified Langevin behavior, or 3) utilize statistical mechanics to bridge established microscale physics to the macroscale [8, 12, 35, 66, 98, 150, 170, 187, 189].

Polynomial series expansions start by constructing phenomenological Taylor series expansion of either the Helmholtz $f(\boldsymbol{H},\boldsymbol{\varepsilon})$ or Gibbs $g(\boldsymbol{H},\boldsymbol{\sigma})$ free energy density. Once a series is constructed $g \approx -\mu_0 \chi_{ij} H_i H_j/2 + ...$, classical thermodynamics is utilized to obtain conjugate field variables like the magnetization $\mu_0 \boldsymbol{M} = -(\partial g/\partial \boldsymbol{H})$ and magnetostriction $\boldsymbol{\varepsilon}_m = -(\partial g/\partial \boldsymbol{\sigma})$. These models are straightforward to utilize once the expansion coefficients (i.e., material properties) are identified [35, 170]. However, conducting the requisite

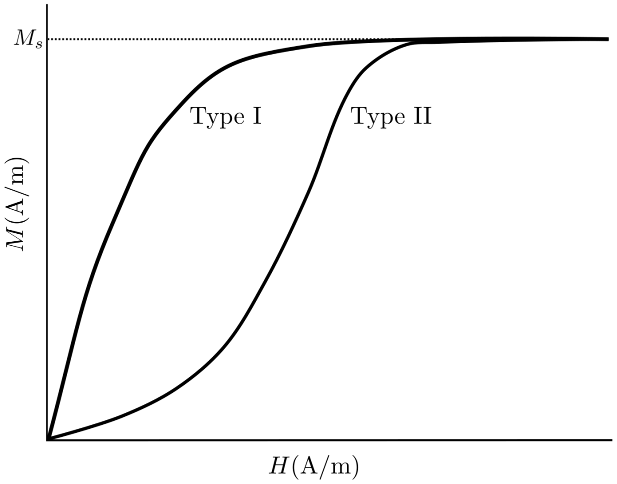

Figure 3.1: Schematic of two representative MH curves for magnetostrictive materials at fixed stress. Depending on the crystal structure of the material the responses can generally be described by curves that are always concave down (Type I) or curves that transition from concave up to down. (Type II)

number of experiments to measure the expansion coefficients can be technically challenging and costly. Routinely only first order expansions are utilized, resulting in a preponderance of 'piezomagnetic' models, even though piezomagnetism is a fairly rare phenomenon most prevalent in antiferromagnets [63, 88, 131, 179]. One important restriction on polynomial approaches is immediately evident from the curves in Figure 3.1. Notably, finite expansions are incapable of capturing the saturating behavior inherent in magnetic phenomena. As a result the use of polynomial models must be accompanied by knowledge of their bias conditions and limited range of validity. While the use of higher-order expansions can increase the range of validity, their use comes at the large cost of rapidly increasing the number of expansion coefficients. In practice unknowns or variations in test setups can result in difficulties using these linearized material properties when modeling an actual nonlinear device.

A common alternative to polynomial models is to *a priori* assume a magnetic constitutive response that saturates and also assume micromagnetic expressions for magnetostriction are valid at the macroscale. We refer to this below as 'Langevin magnetostriction'. An example of this approach is to assume $\boldsymbol{\varepsilon_m} \propto \boldsymbol{M} \otimes \boldsymbol{M}$, with $\boldsymbol{M} = M_s \mathcal{L}(\boldsymbol{h})\hat{\boldsymbol{h}}$ where $M_s$ is the saturation magnetization and $\mathcal{L}$ is the Langevin function depending on the reduced magnetic field $\boldsymbol{h}$ [111, 148]. While the reduced field $\boldsymbol{h}(\boldsymbol{H}, T)$ is conventionally obtained from a ratio of the magnetic field energy divided by the thermal energy, several authors have made *ad-hoc* assumptions that extend $\boldsymbol{h}(\boldsymbol{H}, \boldsymbol{\sigma}, T)$ to depend on stress $\boldsymbol{\sigma}$ as well [98, 111, 148, 150, 176, 187, 189]. Langevin magnetostriction can qualitatively simulate a family of the Type I magnetization curves shown in Figure 3.1, where stress modulates the susceptibility. While Langevin magnetostriction provides a path to incorporating saturating behavior and magneto-mechanical coupling, it also introduces inconsistencies compared to experimental observations, and more advanced models (e.g., micromagnetics). One large inconsistency introduced by Langevin magnetostriction concerns the ΔE effect.

While the assumption $\boldsymbol{\varepsilon_m} \propto \boldsymbol{M} \otimes \boldsymbol{M}$ is often justified by appealing to the micromagnetic response $\boldsymbol{\varepsilon_m} \propto \boldsymbol{M} \otimes \boldsymbol{M}/M_s^2 = \boldsymbol{m} \otimes \boldsymbol{m}$, it is not generally possible to simply extend micromagnetic behavior to the macroscale without a suitable averaging procedure (e.g., it's more accurate to say $\boldsymbol{\varepsilon_m} \propto \langle \boldsymbol{m} \otimes \boldsymbol{m} \rangle$, where $\langle . \rangle$ is a relevant thermal average). Consider that when $\boldsymbol{H} = 0$ an anhysteretic constitutive model predicts $\boldsymbol{M} = 0$, and therefore the assumptions above identically produce zero macroscopic magnetostriction $\boldsymbol{\varepsilon_m}(\boldsymbol{H} = 0, \boldsymbol{\sigma}) = 0$. However, magnetic domains are easily controlled with stress at zero magnetic field, which is exemplified in numerous experimental studies that observe the peak $\Delta E$ effect occurs when $\boldsymbol{H} = 0$ [54, 55, 87]. This observed response is explicitly due to zero-field magnetostriction. Attempting to use Langevin Magnetostriction models while designing a device reliant on the $\Delta E$ effect, like a magnetometer [82, 125, 168], is therefore expected to be a challenging endeavor. Instead of *a priori* assuming $\boldsymbol{M} = M_s \mathcal{L}(\boldsymbol{h})\hat{\boldsymbol{h}}$, we highlight that the Langevin model for classical paramagnetism is derived using statistical mechanics, indicating these assumptions likely do not need to be made.

Models constructed with statistical mechanics are capable of capturing the full nonlinear saturating behavior and strong magneto-mechanical coupling of magnetostrictive materials. The Gibbs Canonical Ensemble can be used to model a magnetostrictive material in thermal equilibrium with a heat bath (the environment) at constant temperature, capable of having work done on it. As shown in Equations (4.2) - (3.2) this can be used to calculate the partition function $Z$ and the expected macroscale free energy $G$ for a given (microscopic) Landau free energy $G_L$ [24].

$$Z = \int_{\mathbb{M}} \exp\left(-\frac{G_L}{k_b T}\right) \mathrm{d}\boldsymbol{m} \tag{3.1}$$

$$G = -k_b T \ln Z \tag{3.2}$$

In these equations $k_b T$ is the thermal energy and integration is over all possible states of the system (i.e. $\mathbb{M}$ is the set of all admissible magnetization distributions). The Landau free energy contains any of the relevant energy densities used in micromagnetics. This allows the impact of external magnetic fields, magnetostatic fields (demag), magnetocrystalline anisotropy (MCA), exchange energy, and magnetostriction to be incorporated [24, 41, 50, 94, 105, 133]. Once the expected energy $G$ is constructed, classical thermodynamics can be utilized, and a series of partial derivatives leads to the average properties of the system. For a uniform system with volume $V$, the average magnetic moment $\langle \boldsymbol{\mu} \rangle = \langle \boldsymbol{M} \rangle V = -(\partial G / \partial \boldsymbol{H})/\mu_0$, and magnetostriction $\langle \boldsymbol{\varepsilon}_m \rangle = -(\partial G / \partial \boldsymbol{\sigma})/V$.

Models that include all of the relevant micromagnetic energy densities can potentially model paramagnetic, ferromagnetic, ferrimagnetic, and antiferromagnetic materials with arbitrary anisotropy energies, and even account for polycrystalline materials [24, 41]. Once the general 3D definitions of the micromagnetic energies are included (e.g., cubic MCA), the partition function currently has no known exact analytic solution. Therefore, evaluating the integrals often requires approximations including numerical evaluation [8, 12, 66]. Improving the computational efficiency of these models has been the focus of recent research that has shown an excellent ability to fit these models to experimental data [13, 15, 66, 67, 68, 69]. These improvements are the result of common simplifying assumptions including zero exchange coupling (i.e., paramagnetic behavior) [15, 68, 154, 169], potentially with simplified magnetocrystalline anisotropies [67, 68, 69, 169]. The supplemental section of this paper shows how the assumptions of these models can restrict them to modeling only specific material compositions. Furthermore, it is shown that the early versions of these models use an approximated MCA that can only be developed using an MCA that violates time reversal symmetry. Finally, it was shown that the numerics of these models are influencing the behavior of the material.

While generating a general 3D model is certainly a goal for this line of research, the authors contend that simplifying the model to one dimension serves as a necessary first step along this line and has several additional benefits. Most notably, as we will show below there is a closed form analytical solution for a suitably simplified 1D model. Using this model in the JA model offers a complete hysteretic model of magnetostriction in one dimension. Furthermore, it provides an accurate model that future numerical approximations can be compared to. Additionally, we note that most macroscale experimental studies have utilized conditions where the applied magnetic field and surface traction are parallel $\boldsymbol{H} \parallel \boldsymbol{T}$ [13, 45, 65, 115, 121, 178, 187, 188]. Each of the cited experimental studies has therefore provided effectively one-dimensional data, and not tested general 3D loading conditions. In addition to explaining existing experimental data, a valid 1D model is also expected to find use in reduced order models, including magnetostrictive rod and beam theories [130, 174, 184].

The work in this paper presents an analytic constitutive model for magnetostrictive materials that is derived using statistical mechanics. This is made possible by restricting the allowed orientations of the applied magnetic field, stress, and MCA, in addition to restricting the allowable type of MCA. In the following sections we present the necessary assumptions, derive a 1D magnetostrictive constitutive model, provide a convenient numerical implementation, and use the model to simulate experimental data from the literature. Results show this model is capable of accurately simulating the response of materials with isotropic Joulian magnetostriction when the magnetocrystalline anisotropy of the material produces Type I magnetization curves as depicted in Figure 3.1).

## 3.2 Model Development

### 3.2.1 Boltzmann Statistics

In this section we use the Gibbs Canonical Ensemble to describe a paramagnetic magnetostrictive material in thermal equilibrium with an environment at constant temperature, capable of having work done on it. For a paramagnetic material we focus on the average response of an isolated magnetic moment, allowing us to write the partition function and expected free energy density as

$$z = \int_S \exp\left(-\beta g_L\right) \mathrm{d}\boldsymbol{m} \tag{3.3}$$

$$g = -\beta^{-1} \ln z \tag{3.4}$$

where $g_L$ is the Landau free energy density, $\beta^{-1}$ is the thermal energy density, and integration is now restricted to all orientations of $\boldsymbol{m} = \boldsymbol{M}/M_s$ (i.e., over the unit sphere $S$). Notationally, we are using lowercase letters $\{z, g_L, g\}$ to denote intensive properties (e.g., energy densities), while the capital $\{Z, G_L, G\}$ in Equations (4.2) and (3.2) were extensive properties of the system. Shown in Equation (3.5), we consider a free energy density composed of Zeeman

$f_z$, magnetoelastic anisotropy $f_{me}$, and magnetocrystalline anisotropy $f_{mca}$ energy densities [24, 41, 50, 133].

$$g_L = f_z(\boldsymbol{m}; \boldsymbol{H}) + f_{me}(\boldsymbol{m}; \boldsymbol{\sigma}) + f_{mca}(\boldsymbol{m}; \boldsymbol{K}) \tag{3.5}$$

where the notation $f(\boldsymbol{m}; ...)$ indicates $\boldsymbol{m}$ is a prescribed parameter and $\boldsymbol{K}$ is the MCA tensor. Once the partition function is constructed the equilibrium magnetization and magnetostriction are calculated by taking partial derivatives of the expected free energy in Equation (3.4), leading to

$$\begin{aligned}
\langle \boldsymbol{M} \rangle &= M_s \frac{1}{z} \int_S \boldsymbol{m} \exp(-\beta g_L) \mathrm{d}\boldsymbol{m} \\
&= M_s \langle \boldsymbol{m} \rangle \qquad (3.6) \\
\langle \boldsymbol{\varepsilon}_m \rangle &= \frac{3\lambda_s}{2} \frac{1}{z} \int_S \boldsymbol{m} \otimes \boldsymbol{m} \exp(-\beta g_L) \mathrm{d}\boldsymbol{m} \\
&= \frac{3}{2} \lambda_s \langle \boldsymbol{m} \otimes \boldsymbol{m} \rangle \qquad (3.7)
\end{aligned}$$

where $\lambda_s$ is the saturation magnetostriction. Based on Equations (4.17) and (4.18) for the average magnetization and magnetostriction, we can identify the probability density function $P(\boldsymbol{m}; \boldsymbol{H}, \boldsymbol{\sigma}, \beta) = \exp(-\beta g_L)/z$. This allows equations (4.17) and (4.18) to be interpreted as thermal averages of the micromagnetic equations for magnetization and isotropic Joulian magnetostriction.

In addition to obtaining the magnetization and magnetostriction, the nonlinear material properties can be calculated by taking derivatives of the previous expressions. The properties are readily shown to be,

$$\langle \boldsymbol{\chi} \rangle = \beta\mu_0(\langle \boldsymbol{M} \otimes \boldsymbol{M} \rangle - \langle \boldsymbol{M} \rangle \otimes \langle \boldsymbol{M} \rangle) \tag{3.8}$$

$$\langle \boldsymbol{S_m} \rangle = \beta(\langle \boldsymbol{\varepsilon}_m \otimes \boldsymbol{\varepsilon}_m \rangle - \langle \boldsymbol{\varepsilon}_m \rangle \otimes \langle \boldsymbol{\varepsilon}_m \rangle) \tag{3.9}$$

$$\langle \boldsymbol{q} \rangle = \beta(\langle \boldsymbol{M} \otimes \boldsymbol{\varepsilon}_m \rangle - \langle \boldsymbol{M} \rangle \otimes \langle \boldsymbol{\varepsilon}_m \rangle) \tag{3.10}$$

where $\langle \boldsymbol{\chi} \rangle$ is the magnetic susceptibility at constant stress, $\langle \boldsymbol{S_m} \rangle$ the magnetostrictive compliance at constant magnetic field, and $\langle \boldsymbol{q} \rangle$ the piezomagnetic coupling tensor defined by $\langle \boldsymbol{q} \rangle = \partial \langle \boldsymbol{M} \rangle / \partial \boldsymbol{\sigma} = \mu_0^{-1} \partial \langle \boldsymbol{\varepsilon_m} \rangle / \partial \boldsymbol{H}$. We briefly note that the total compliance $\boldsymbol{S} = \boldsymbol{S}_{el} + \langle \boldsymbol{S}_m \rangle$, where $\boldsymbol{S}_{el}$ is the elastic compliance (e.g., inverse Young's modulus for 1D loading). The form of Equations (3.8) - (3.10) reveals that the macroscopic material properties are proportional to the statistical variance / fluctuation of the underlying microscopic fields (i.e., $\text{var}(x) = \langle x^2 \rangle - \langle x \rangle^2$). Finally, we note that a key advantage of having accurate solutions to Equations (4.17) and (4.18) is that they are reused in Equations 8-10. Therefore, in calculating equations (3.8)-(3.10) only 3 additional terms $\langle \boldsymbol{M} \otimes \boldsymbol{M} \rangle$, $\langle \boldsymbol{\varepsilon}_m \otimes \boldsymbol{\varepsilon}_m \rangle$, and $\langle \boldsymbol{M} \otimes \boldsymbol{\varepsilon}_m \rangle$ need to be calculated. In contrast, when the integrals in Equations (4.17) and (4.18) are approximated, numerical differentiation is needed to provide the linearized materials properties [37, 58, 68, 69, 127, 160, 161]. This increases the computational burden of the approximations.

We briefly note that due to the exponential term in the partition function, Equations (4.5) - (3.10) can lose numerical accuracy when evaluated. One way to preserve the numerical accuracy of the solution is by shifting the free energy with functions that are independent of $\boldsymbol{m}$. The magnetization $\langle \tilde{\boldsymbol{M}} \rangle$ and magnetostriction $\langle \tilde{\boldsymbol{\varepsilon}}_{\boldsymbol{m}} \rangle$ obtained from the free energy $\tilde{g}_L = g_L + f(\boldsymbol{H}, \boldsymbol{\sigma})$ is related to the average magnetization $\langle \boldsymbol{M} \rangle$ and magnetostriction $\langle \boldsymbol{\varepsilon}_m \rangle$

obtained from $g_L$ by

$$\tilde{z} = \int_S \exp\left(-\beta \tilde{g_L}\right) \mathrm{d}\boldsymbol{m} = z\, \exp(-\beta f) \tag{3.11}$$

$$\left\langle \tilde{\boldsymbol{M}} \right\rangle = -\frac{1}{\mu_0} \frac{\partial f}{\partial \boldsymbol{H}} + \langle \boldsymbol{M} \rangle \tag{3.12}$$

$$\langle \tilde{\boldsymbol{\varepsilon}}_m \rangle = -\frac{\partial f}{\partial \boldsymbol{\sigma}} + \langle \boldsymbol{\varepsilon}_m \rangle\,. \tag{3.13}$$

In practice, a function independent of $\boldsymbol{m}$ can be added to $g_L$ to ensure the Boltzmann term $\exp\left(-\beta \tilde{g_L}\right) \leq 1$ which aids in numerical calculations (i.e., so the exponential doesn't lead to numerical inaccuracies when $g_L << -1$). In what follows, terms with tilde overbars are understood to include an energy offset as described in Equations (3.11)-(3.13).

As previously stated, the integrals used in Boltzmann statistics do not generally possess closed form solutions. However, we now show that exact closed form solutions exist for a specific type of MCA and restrictions on the orientations of the magnetic field and stress.

### 3.2.2 Quadratic Anisotropy

A closed form solution to Equations (4.5) - (3.10) can be obtained under the following assumptions: 1) the MCA can be represented as a quadratic form $f_{mca} = \boldsymbol{m} \cdot \boldsymbol{K}\boldsymbol{m}$, 2) the material displays isotropic magnetostriction (i.e., $\lambda_{100} = \lambda_{111} = \lambda_s$), 3) the combined magnetoelastic anisotropy and MCA is transversely isotropic, and 4) the magnetic field is perpendicular to the isotropic anisotropy plane. To satisfy these requirements we assume the material has transversely isotropic MCA, with only two unique eigenvalues $K_i$. We assume the unique direction to be the 1-direction, while the 23-plane is isotropic (i.e., $K_1 \neq K_2 = K_3$). Additionally, we assume the stress state has only 2 unique principal stresses $\sigma_1 \neq \sigma_2 = \sigma_3$, where the stress and MCA eigenvectors are parallel. These stress assumptions are commonly satisfied for long rod or beam-like materials with one unique axis, and are consistent with numerous experimental studies [13, 45, 65, 115, 121, 178, 187, 188]. The assumption of transversely isotropic MCA is a key mathematical assumption in this model that restricts the possible materials this model is suitable for. This point will be examined further in the results section.

To see how these assumptions lead to a closed form solution we first construct the total anisotropy energy density $f_A$

$$f_A = f_{mca} + f_{me} \tag{3.14}$$

$$f_{mca} = \boldsymbol{m} \cdot \boldsymbol{K m} = K_{ij} m_i m_j \tag{3.15}$$

$$f_{me} = \boldsymbol{m} \cdot \boldsymbol{\Sigma m} = -\frac{3}{2}\lambda_s \sigma_{ij} m_i m_j, \tag{3.16}$$

where the isotropic magnetostriction is described by $\boldsymbol{\Sigma} = -3\lambda_s \boldsymbol{\sigma}/2$ and $\boldsymbol{\sigma}$ is the Cauchy stress. Both $\boldsymbol{K}$ and $\boldsymbol{\Sigma}$ are symmetric rank 2 tensors. We combine them to define the non-dimensionalized anisotropy tensor $\boldsymbol{A} = -\beta\left(\boldsymbol{K} + \boldsymbol{\Sigma}\right)$. The non-dimensionalized magnetic field is $\boldsymbol{h} = \beta\mu_0 M_s \boldsymbol{H}$.

Expressing these energies with components parallel to the eigenvectors of $\boldsymbol{A}$, $-\beta g_L = A_i m_i^2 + h_i m_i$, where $A_i$ are the eigenvalues of $\boldsymbol{A}$. Additionally, the transversely isotropic $\boldsymbol{A}$ has only two unique eigenvalues $A_1 \neq A_2 = A_3$, and following assumption 4) $\boldsymbol{h} = h\hat{\boldsymbol{e}}_{\boldsymbol{1}}$ is parallel to the 1-axis. Accounting for the fact that $|\boldsymbol{m}| = 1$ is a unit vector, and discarding the resultant term independent of $\boldsymbol{m}$, we have $-\beta g_L = A m_1^2 + h m_1$, where $A = A_1 - A_2$ is the change in anisotropy energy from the isotropic plane to the transverse axis. Summarizing, based on the assumptions above we can simplify Equation (4.5) to

$$z = 2\pi \int_{-1}^{1} \exp\left(A m_1^2 + h m_1\right) \mathrm{d}m_1 \tag{3.17}$$

Of note, performing the change of variables $y = \sqrt{A}(m_1 + h/2A)$ on (3.17) and decomposing the integral from $-1 < m_1 < 1$ into two integrals $-1 < m_1 < 0$ and $0 < m_1 < 1$ produces two integrals that are identical to the definition of the Dawson function, as shown here,

$$\mathrm{D}(x) = \exp(-x^2) \int_0^x \exp(t^2)\mathrm{d}t. \tag{3.18}$$

However, when $A < 0$ the Dawson function produces complex numbers and calculations using this function can rapidly accumulate large numerical errors. In that case, using the same change of variables on (3.17) while assuming $A < 0$ and decomposing the integral now produces integrals that are identical to the definition of the error function,

$$\mathrm{Erf}(x) = \frac{2}{\sqrt{\pi}} \int_0^x \exp(-t^2)\mathrm{d}t. \tag{3.19}$$

These special functions often occur in statistics and the possible solutions to equation (3.17) are summarized below.

$$\frac{z}{2\pi} = \begin{cases} z_+ = \frac{\exp(A+h)\,\mathrm{D}(\alpha_+) + \exp(A-h)\,\mathrm{D}(\alpha_-)}{\sqrt{A}} & A > 0 \\ z_- = -\frac{\exp\left(-\frac{h^2}{4A}\right)\sqrt{\pi}(\mathrm{Erf}(\gamma_+) - \mathrm{Erf}(\gamma_-))}{2\sqrt{-A}} & A < 0 \end{cases} \tag{3.20}$$

where $\alpha_\pm = (2A \pm h)/(2\sqrt{A})$ and $\gamma_\pm = (h \pm 2A)/(2\sqrt{-A})$. Following equations (4.17) to (3.10) above, derivatives of these expressions can be used to obtain the magnetization, magnetostriction, and nonlinear material properties. However, we first make several refinements to these equations as there are numerous points where, although they are analytically correct, they can accrue large numerical errors when evaluated.

The first point at which the current solutions can become inaccurate is when $h >> |A|$. Notice that in (3.20) as $A \to 0$ the equations become indeterminate. A simple fix for this problem is to utilize a series expansion of the partition function (Equation (3.17)) for small anisotropy values about $A = 0$. The general form of the series expansion is provided in the Appendix in section A.1. Additionally, this approximation can be used to solve for the magnetization, magnetostriction, and material properties. The series expansion should be used when $|A|/h < \epsilon$, where $\epsilon$ will depend on the specific numerical implementation. When testing second order expansions using Matlab, we found a cutoff ratio of $|A|/h < 10^{-7}$ preserved accuracy in the magnetization and magnetostriction.

The use of the error function $\mathrm{Erf}(x)$ is susceptible to numerical errors when $x >> 1$. The numerical accuracy can be improved by introducing the scaled complimentary error function $\mathrm{Erfcx}(x)$, where $\mathrm{Erf}(x) = 1 - \exp(-x^2)\,\mathrm{Erfcx}(x)$. This has the advantage of removing several exponential terms, and helping to avoid arithmetic underflow [48]. As previously stated, these solutions can be further simplified by shifting the free energy. The specific energy offsets used below were all chosen to ensure that exponential terms in the solutions remain bounded as the magnetic field and stress become large. Combining these refinements changes Equation (3.20) to

$$\frac{\tilde{z}}{2\pi} = \begin{cases} \tilde{z}_+ = \frac{\mathrm{D}(\alpha_+) + \exp(-2h)\,\mathrm{D}(\alpha_-)}{\sqrt{A}} & A > 0 \\ \tilde{z}_- = -\frac{\sqrt{\pi}(-\,\mathrm{Erfcx}(\gamma_+) + \exp(-2h)\,\mathrm{Erfcx}(\gamma_-))}{2\sqrt{-A}} & A < 0,\ \gamma_+ > 0 \\ \tilde{z}_- = -\frac{\sqrt{\pi}(-2 + \exp\left(-\gamma_+^2\right)\mathrm{Erfcx}(\gamma_+) + \exp\left(-\gamma_-^2\right)\mathrm{Erfcx}(\gamma_-))}{2\sqrt{-A}} & A < 0,\ \gamma_+ < 0, \end{cases} \tag{3.21}$$

where the energy offsets applied to Equation (3.21) are

$$f = \begin{cases} -A - h & A > 0 \\ -A - h & A < 0,\ \gamma_+ > 0 \\ h^2/4A & A < 0,\ \gamma_+ < 0. \end{cases} \tag{3.22}$$

These offsets were selected to ensure the exponential terms in (3.20) converge to zero as $\{h,\, A\} \to \infty$. The derivatives of equations (3.21) and (3.22) with respect to $h$ results in the average magnetization,

$$\frac{\langle M \rangle}{M_s} = \begin{cases} -\frac{h}{2A} - \frac{-1+\exp(-2h)}{2A\,\tilde{z}_+} & A > 0 \\ -\frac{h}{2A} - \frac{1-\exp(-2h)}{2A\,\tilde{z}_-} & A < 0,\ \gamma_+ > 0 \\ -\frac{h}{2A} + \frac{\exp\left(-\gamma_+^2\right)-\exp\left(-\gamma_-^2\right)}{2A\,\tilde{z}_-} & A < 0, \gamma_+ < 0. \end{cases} \tag{3.23}$$

Additionally, the derivative of (3.20) with respect to $A$ results in an average magnetostriction of

$$\frac{2}{3}\frac{\langle \varepsilon_m \rangle}{\lambda_s} = \begin{cases} \frac{h^2-2A}{4A^2} + \frac{h}{\tilde{z}_+}\left(\frac{1+\exp(-2h)}{2Ah} - \frac{1-\exp(-2h)}{4A^2}\right) & A > 0 \\ \frac{h^2-2A}{4A^2} + \frac{h}{\tilde{z}_-}\left(\frac{1+\exp(-2h)}{2Ah} - \frac{1-\exp(-2h)}{4A^2}\right) & A < 0,\ \gamma_+ > 0 \\ \frac{h^2-2A}{4A^2} + \frac{h}{\tilde{z}_-}\left(\frac{\exp\left(\gamma_+^2\right)+\exp\left(-\gamma_-^2\right)}{2Ah} - \frac{\exp\left(\gamma_+^2\right)+\exp\left(-\gamma_-^2\right)}{4A^2}\right) & A < 0,\ \gamma_+ < 0 \end{cases} \tag{3.24}$$

Expressions for the nonlinear material properties in Equations (3.8) - (3.10) can be obtained through additional derivatives of the equations above. As these expressions are reasonably lengthy, we provide them in section A.2 of the Appendix.

As a final note, the equations above are written assuming that $h \geq 0$. Values for $h < 0$ can readily be obtained by noting the magnetization is an odd function with respect to $h$, while the magnetostriction is even (i.e., for $h < 0$ $M(h) = -M(|h|)$. We also note that in contrast to the Langevin Magnetostriction models discussed in the introduction, when $h = 0$ the magnetostriction $\langle \varepsilon_m \rangle \neq 0$ in this model. Instead, when $h = 0$ a net magnetostriction is induced due to the competing MCA and magnetoelastic anisotropy energies. Finally, similar equations for $\langle M \rangle$ and $\langle \varepsilon_m \rangle$ have previously appeared in the literature, most closely matching the results in Equation (3.23) and (3.24) when $A > 0$ [139, 159]. However, the authors believe this is the first time that solutions capable of maintaining numerical accuracy compared to standard numerical integration methods (i.e. Riemann sums) for both $A < 0$ and $A > 0$ has been presented.

## 3.3 Results and Discussion

This section provides 1) a numerical comparison of the closed form solutions presented in equations (3.21), (3.23), and (3.24) to conventional numerical integration, 2) a qualitative assessment of material response these solutions produce, and finally 3) assesses the model's ability to simulate the experimentally measured response of several common magnetostrictive materials.

### 3.3.1 Numerical Accuracy

To evaluate the numerical accuracy of these solutions they were compared to standard numerical integration. A grid of $N = 100$ logarithmically spaced field points $10^{-2} \leq h \leq 10^{6}$ and $N = 200$ logarithmically spaced anisotropies $10^{-2} \leq | \pm A| \leq 10^{6}$ were generated for $N_{total} = 20,000$ points. At each grid point numerical integration was performed using Matlab's `integral()` function with relative and absolute errors of $10^{-12}$. The relative errors for each equation were calculated as $|f_{num} - f_{eqn}|/f_{num}$, where $f$ is the parameter of interest. While we utilized Matlab's built-in scaled complimentary error function `erfcx()`, the built-in Dawson function was quite slow, and instead we approximated D() using McCabe's continued fraction. This achieves a precision to $10^{-15}$, and has a simple and fast numerical implementation [119]. Furthermore, the analytical solutions were found to be three orders of magnitude faster than standard numerical integration. The accuracy results are summarized in Table 3.1. Additionally, detailed error surfaces are shown in section A.3 of the

Table 3.1: Accuracy compared to numerical integration

| Function | Avg. Error | Max Error |
|---|---|---|
| $\tilde{z}$ | $2.4 \times 10^{-3}$ | $6.8 \times 10^{-1}$ |
| $\langle M \rangle$ | $1.9 \times 10^{-11}$ | $2.3 \times 10^{-9}$ |
| $\langle \varepsilon_m \rangle$ | $2.4 \times 10^{-5}$ | $3.9 \times 10^{-3}$ |

Appendix. The data in Table 3.1 shows 1) the average relative error per grid point (i.e., sum of individual errors divided by $N_{total}$) and 2) the maximum relative error at a single grid point. The relative errors of all three functions were approximately $10^{-14}$ for the majority of the tested grid points. The only region where the solutions became inaccurate was when the series expansion was used for $|A|/h < 10^{-7}$. The maximum errors were all measured in the expansion region. It should be noted that without the series expansion the error can quickly climb above 100% in that region (i.e., the expansion worked). While the partition function had a maximum error of over 50% for the expansion, the resulting magnetization and magnetostriction still remained accurate as they depend on derivatives of $z$ not its absolute value. The max relative error in the magnetostriction only reached 0.4%.

To provide more context for this information, if we consider the material properties for Terfenol-D that are presented in Section 3.3.3 below, we can show that the accuracy analysis above is valid for applied fields $0 \leq \mu_0 H \leq 200$ T and stresses $0 \leq \sigma \leq 10$ TPa, respectively. This range is clearly far outside those used in standard laboratory settings, leaving the authors to conclude the presented equations remain numerically accurate for fields and stress conditions typically applied to these materials. Material failure and additional phenomena would need to be considered before these equations become numerically inaccurate. Additionally, this accuracy is separate from the consideration of whether or not the model can accurately describe experimental measurements, which will be considered in Section 3.3 below.

### 3.3.2 Qualitative Assessment

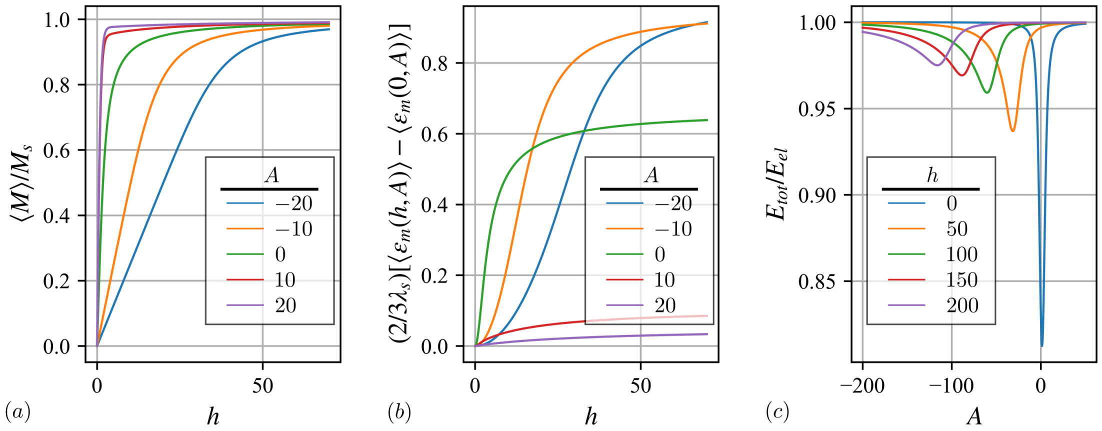

Figure 3.2: Model predictions of (a) magnetization and (b) magnetostriction and (c) the $\Delta E$ effect for possible $h$ and $A$ values.

Having shown the equations above accurately solve the integral expressions used in statistical mechanics, we now turn our attention to analyzing the qualitative response of the resulting model. Figure 3.2 illustrates the (a) magnetization and (b) magnetostriction curves at fixed anisotropy $A$. Figure 3.2 (c) shows the $\Delta E$ effect this model predicts at fixed values of $h$. Starting with Figure 3.2 (a) we note that in addition to properly saturating, the model has a lower susceptibility when A is negative and a higher susceptibility when A is positive which corresponded to compression and tensions respectively, for a positive magnetostrictive material. Furthermore, when $A = 0$ the model reduces to the Langevin function as required. Finally, while only small values of $A$ are presented in Figure 3.2(a), over the entire range of tested values $10^{-2} \leq |\pm A| \leq 10^{6}$ only Type I behavior was observed. This model does not qualitatively describe materials with Type II MH curves.

Figure 3.2 (b) shows the predicted magnetostriction curves as a function of $h$ with different lines at fixed anisotropy $A$. Note that the zero field magnetostriction has been subtracted from each curve to clearly display all curves on the same graph. Therefore, the plot shows

$\langle \varepsilon_m(h, A)\rangle - \langle \varepsilon_m(0, A)\rangle$. For a positive magnetostrictive material in tension $A > 0$, the model correctly predicts a small change in magnetostriction as $h$ increases. For this case tension produces an initial magnetization configuration where the microscale magnetization starts either parallel or anti-parallel to the magnetic field direction. Upon increasing $h$ the anti-parallel domains transition to parallel, however there is no resulting magnetostriction as $\varepsilon_m \propto m_1^2$ is even in the magnetization. Conversely, compression causes the magnetization to initially align perpendicular to the applied field direction. Increasing the applied magnetic field then forces the domains to become parallel. For a large enough initial compression this results in $\langle \varepsilon_m(h, A)\rangle - \langle \varepsilon_m(0, A)\rangle = 3\lambda_s/2$ as $h$ increases.

Concluding with Figure 3.2 (c) the total Young's modulus of the material $E_{tot}$ was calculated using the using the magnetostrictive compliance $S_m$ and elastic Young's Modulus $E_{el}$,

$$E_{tot} = (1/E_{el} + \langle S_m\rangle)^{-1}. \tag{3.25}$$

As the intention of Figure 3.2 is qualitative assessment of the predicted behavior, a Young's Modulus of 1 Pa was chosen. Changing this value changes the amplitude of $E_{tot}$ and $\Delta E$, but not the locations of the peaks. The trends in this graph are consistent with experimental data in which the largest $\Delta E$ effect is observed at zero magnetic field [55]. Furthermore, recalling that A is composed of MCA and magnetoelastic anisotropy, this model shows that in order to maximize the $\Delta E$ effect an applied stress that cancels out MCA is required. The maximum value of $\langle S_m\rangle$ obtained from Equation (3.9) is equal to $\beta\lambda_s^2/5$, leading to the maximum $\Delta E = E_{el} - E_{tot}$.

$$\max \Delta E = \left(\frac{1}{E_{el}} + \frac{5}{\beta\lambda_s^2 E_{el}^2}\right)^{-1} \tag{3.26}$$

### 3.3.3 Experimental Comparison

In addition to confirming the numerical accuracy of the magnetization and magnetostriction in Equations (3.23) and (3.24), the solutions were compared to magnetization and magnetostriction curves found in the literature for three different materials, Terfenol-D $Tb_{0.3}Dy_{0.7}Fe_{19.2}$, and two compositions of Galfenol $Fe_{79.1}Ga_{20.9}$, and $Fe_{81.6}Ga_{18.4}$. It is worth emphasizing that none of these materials are paramagnetic, and single crystals of each display cubic symmetry. However, for polycrystalline sample that have undergone processing that induces a preferred axis (e.g., stress annealing), it is plausible that they can be approximated with a transversely isotropic model [142]. The section below tests this assumption. The authors digitized data for Terfenol-D from Zhao and Lord [188], and the two compositions of Galfenol from Mahadevan, Evans, and Dapino [115]. The saturation magnetization $M_s$ and saturation magnetostriction $\lambda_s$ were directly obtained from the experimental data, with $M_s = \max(|M|)$, and $\lambda_s = 2/3\max(|\varepsilon_m|)$. The magnetostriction calculation came from curves where we assume the initial bias stress was large enough to exclusively produce 180° domain walls in the material when $H = 0$. After $M_s$ and $\lambda_s$ were obtained, the only remaining unknowns in the model are the magnetocrystalline anisotropy coefficient $K$, and the thermal energy density term $\beta$. For each material $K$ and $\beta$ were identified by minimizing the relative error between the constitutive model and the experimental data. This calculation produces error surfaces that only depend on two variables. Therefore, we did not use a nonlinear optimization routine but instead calculated the error over a grid of $K$ and $\beta$ values. These error surfaces are presented in the results below.

The values of $K$ and $\beta$ obtained from this procedure, along with the average and maximum relative error between the modeled and experimental data are presented in Table 4.2. As we calculate errors when comparing the 1) magnetization and 2) magnetostriction data, we present three sets of values for $\{K, \beta\}$, and their errors for each material. The three cases are for 1) fitting the combined data set, 2) fitting only the magnetization data, and 3) fitting only the magnetostriction data. The last two fits can be utilized for models requiring only $\langle M \rangle$ or $\langle \varepsilon_m \rangle$ (i.e., in one-way-coupled models).

Table 3.2: Model Parameters and Results*

| Material | Fit | $K$ | $\beta$ | Avg. Error $\langle M \rangle$ | Avg. Error $\langle \varepsilon_m \rangle$ | Max. Error $\langle M \rangle$ | Max. Error $\langle \varepsilon_m \rangle$ |
|---|---|---|---|---|---|---|---|
| $Tb_{0.3}Dy_{0.7}Fe_{19.2}$ | Combined | -4697 | $6.5 \times 10^{-4}$ | 7.8 % | 3.0 % | 33 % | 20 % |
| $M_s = 7.8 \times 10^5$ | Only $\langle M \rangle$ | 6515 | $1.6 \times 10^{-4}$ | 5.0 % | — | 55 % | — |
| $\lambda_s = 1.4 \times 10^3$ | Only $\langle \varepsilon_m \rangle$ | -4697 | $6.6 \times 10^{-4}$ | — | 3.0 % | — | 19 % |
| $Fe_{79.1}Ga_{20.9}$ | Combined | 363.6 | $1.1 \times 10^{-3}$ | 6.4 % | 12 % | 26 % | 38 % |
| $M_s = 1.2 \times 10^6$ | Only $\langle M \rangle$ | -767.7 | $7.4 \times 10^{-4}$ | 4.0 % | — | 13 % | — |
| $\lambda_s = 1.3 \times 10^2$ | Only $\langle \varepsilon_m \rangle$ | 1010 | $2.8 \times 10^{-3}$ | — | 6.7 % | — | 37 % |
| $Fe_{81.6}Ga_{18.4}$ | Combined | 909.2 | $1.7 \times 10^{-3}$ | 6.8 % | 7.0 % | 23 % | 31 % |
| $M_s = 1.2 \times 10^6$ | Only $\langle M \rangle$ | 1333 | $1.6 \times 10^{-3}$ | 6.5 % | — | 22 % | — |
| $\lambda_s = 1.7 \times 10^2$ | Only $\langle \varepsilon_m \rangle$ | 1636 | $4.6 \times 10^{-3}$ | — | 5.7 % | — | 31 % |

*Units: $M_s$ (A/M), $\lambda_s$ (ppm), $K$ (J/m$^3$), $\beta$ (m$^3$/J)

Figure 3.3 parts (a) and (b) compare the model with experimental data for Terfenol-D using the combined fit parameters in Table 4.2. The solid lines are the digitized experimental data, while the circular markers are modeled data points. Figures 3.3 (c)-(e) show the average relative error per data point for the data in 3.3(a) and 3.3(b). The red triangular markers show the location of the optimal values for the combined error, while the yellow circles are the locations of minimum error when fitting just the magnetization / magnetostriction. When using the $\{K, \beta\}$ that minimize the combined error, there is 7.8% and 3.0% relative error per data point in the magnetization and magnetostriction comparison, respectively. It is worth noting that the best fit parameters for the magnetization 3.3(d) and magnetostriction 3.3(e) occur for different $\{K, \beta\}$. The combined result in 3.3(c) is skewed towards the optimal magnetostriction location as a wide range of $\{K, \beta\}$ values produce errors close to the global

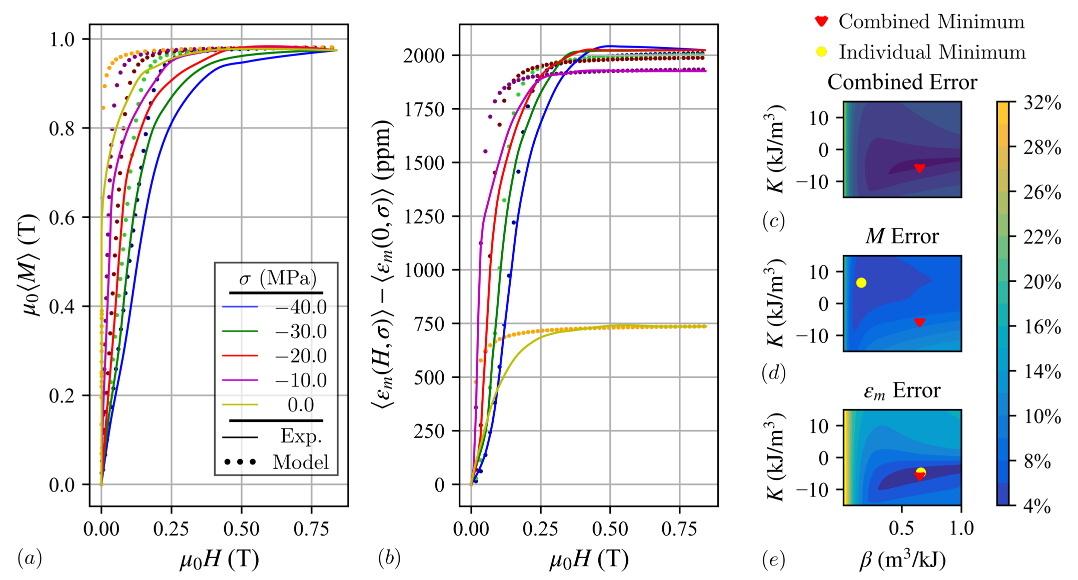

Figure 3.3: (a) Magnetization and (b) magnetostriction of $Tb_{0.3}Dy_{0.7}Fe_{19.2}$ at constant stress values compared to the 1D constitutive model with $\{K, \beta\}$ minimizing the combined error. Relative errors of (c) the combined data, (d) only the magnetization, and (e) only the magnetostriction for a parametric sweep of $K$ and $\beta$. In parts (c)-(e) the red triangular markers are the locations of minimum combined error, while the yellow circular markers are locations of minimum magnetization or magnetostriction error. Data digitized from [188].

magnetization minima of 5.0% (as seen in 3.3(d)). It is possible to reduce the average error to 5.0% if only the magnetization is compared, or 3.0% if only the magnetostriction is compared.

Figure 3.4 parts (a) and (b) show a comparison of the experimental data for $Fe_{79.1}Ga_{20.9}$ using the combined fit parameters, with formatting identical to 3.3. Figures 3.4(c)-(e) show the average relative error for the data in 3.4(a) and 3.4(b) is 6.4% and 12% per data point respectively. For this material the magnetization data is accurately described, while the model struggles to capture the magnetostriction data in compression. It is possible to reduce the average error to 4.0% if only the magnetization is compared, or 6.7% if only the magnetostriction is compared (i.e., the presented magnetization is close to its best fit, while the magnetostriction can be improved). Figure 3.5 parts (a) and (b) show a comparison of

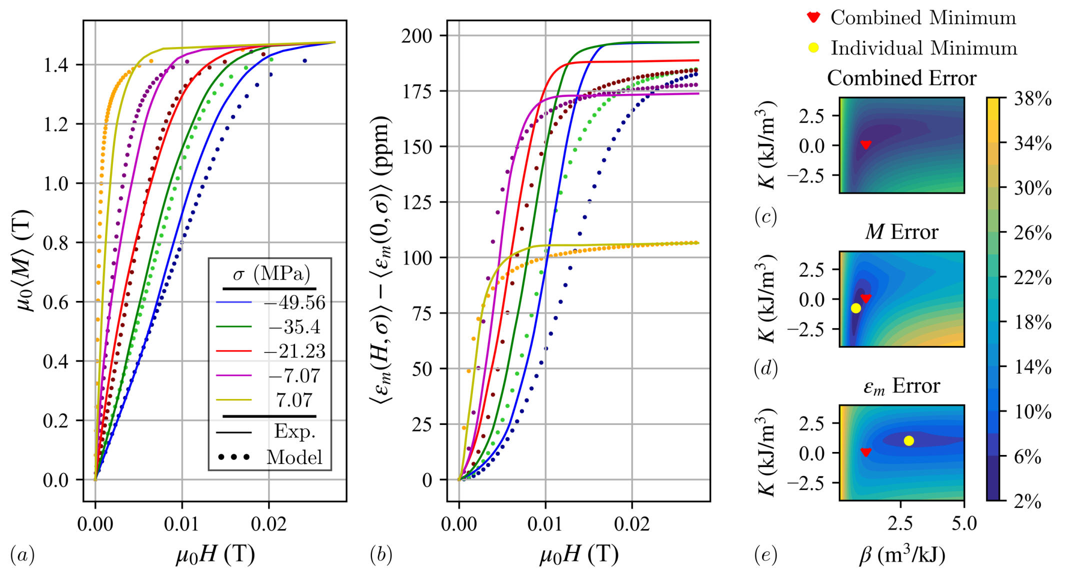

Figure 3.4: (a) Magnetization and (b) magnetostriction of $Fe_{79.1}Ga_{20.9}$ at constant stress values compared to constitutive model. Relative errors of (c) the magnetization (d) the magnetostriction and (e) the combination of the two over a parametric sweep of $K$ and $\beta$. In parts (c)-(e) the red triangular markers are the locations of minimum combined error, while the yellow circular markers are locations of minimum magnetization or magnetostriction error. Data digitized from [115].

the experimental data for $Fe_{81.6}Ga_{18.4}$ using the combined fit parameters. Figures 3.5 (c) shows the average relative error for the data in 3.5(a) and (b) is 6.8% and 7% per data point respectively. Once again, the combined result in 3.5(c) is skewed towards the optimal magnetization. Despite this low relative error, a close look at 3.5(a) shows that the constitutive model doesn't qualitatively capture the nonlinear (Type II) behavior that occurs when the material is subjected to large compressive stresses. As a result, we do not recommend using the analytical model for this composition of Galfenol. Revisiting the anisotropy assumptions utilized in this model can help explain when the model is expected to accurately simulate experimental data. A relatively small restriction was placed on the isotropic magnetostrictive and Zeeman energies by assuming the principal stresses $\sigma_1 \neq \sigma_2 = \sigma_3$, with a magnetic field $\boldsymbol{H} \parallel \hat{e}_1$. We note this mimics the field / stress combinations applied in

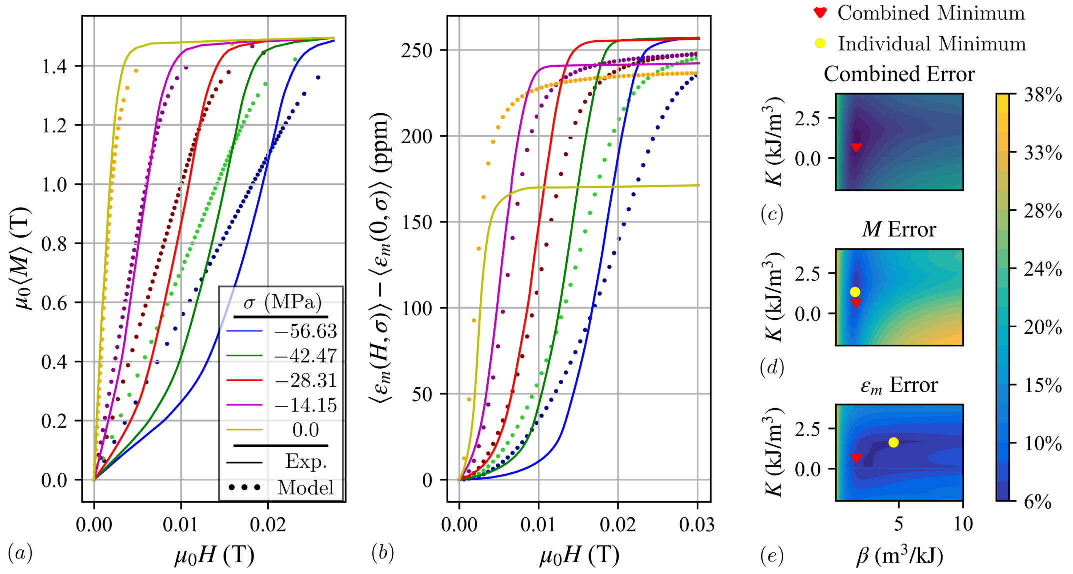

Figure 3.5: (a) Magnetization and (b) magnetostriction of $Fe_{81.6}Ga_{18.4}$ at constant stress values compared to constitutive model. Relative errors of (c) the magnetization (d) the magnetostriction and (e) the combination of the two over a parametric sweep of $K$ and $\beta$. In parts (c)-(e) the red triangular markers are the locations of minimum combined error, while the yellow circular markers are locations of minimum magnetization or magnetostriction error. Data digitized from [115].

the experimental studies compared to above and therefore should not decrease the accuracy of the model. Even for a non-isotropic magnetostrictive material, as long as the stress and field are parallel to the $\langle 100\rangle$ direction the model accurately describes the magnetostrictive energy. Conversely, a significant restriction was placed on the MCA by requiring it to be transversely isotropic. Due to this assumption the model is only capable of modeling Type I MH curves. The crystalline structure of Terfenol-D and Galfenol are typically cubic with MCA of the form,

$$f_{cubic} = K_1(m_1^2 m_2^2 + m_2^2 m_3^2 + m_3^2 m_1^2) + K_2(m_1^2 m_2^2 m_3^2). \tag{3.27}$$

While the use of cubic MCA is expected to produce a more accurate model, there is no known closed form solution to the integral equations above once an MCA of this form is utilized. However, we can analyze the effect $K_1$ and $K_2$ have on magnetization curves by relying on numerical integration (e.g., Riemann sums), to compare cubic MCA to transversely isotropic. Figure 3.6 (a) shows a Type I MH curve produced using the proposed model under 50 MPa of compression, and a $K$ value of -4500 (J/m$^3$), simulating the Terfenol-D modeled above. To understand how the MH curve saturates we examine the probability landscape of two points along the curve. For each point of interest, the probability density of the system in spherical coordinates is calculated using $P(\theta; H, \sigma, \beta) = \exp(-\beta g_L)/z$. The inset of Figure 3.6 (a) plots the probability density against the possible magnetization directions $\theta$. Starting at Point 1, $\mu_0 H = 15$ mT in the negative $z$ direction, the applied field has moved the peak probability from $\theta = \pi/2$ a small amount towards $\theta = \pi$. As $\mu_0 H$ increases to 20 mT and we transition along the MH curve to Point 2, the peak again gradually shifts to the right. As the field is continually increased past Point 2, the location of peak probability continues to gradually shift towards $\theta = \pi$. It is this gradual change in the probable direction of

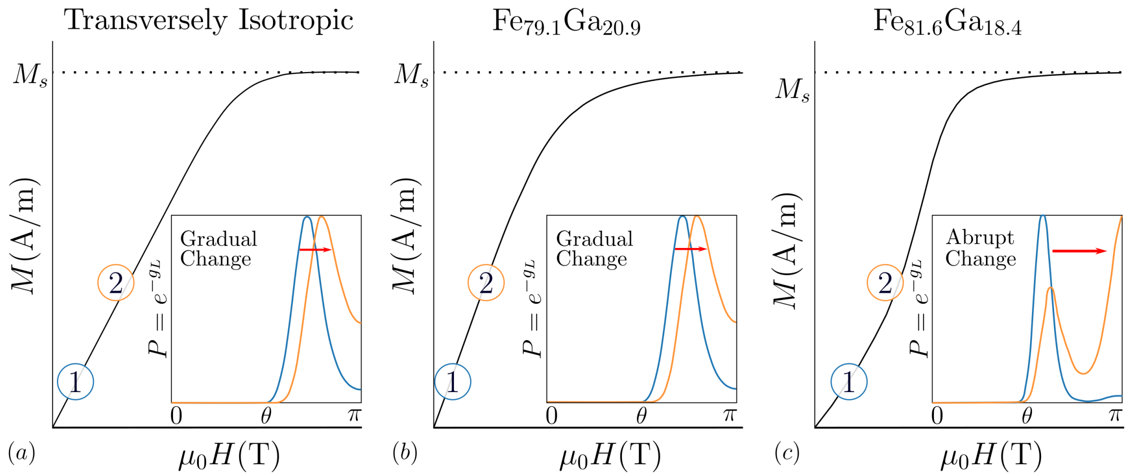
Transversely Isotropic

$Fe_{79.1}Ga_{20.9}$

$Fe_{81.6}Ga_{18.4}$

Figure 3.6: MH curves under 50 MPa of compression with (a) Transversely Isotropic MCA, $K = -4500\text{J/m}^3$, (b) Cubic MCA for $Fe_{79.1}Ga_{20.9}$, $K_1 = -1e3\text{J/m}^3$ and $K_2 = 1e4\text{J/m}^3$, (c) and Cubic MCA for $Fe_{81.6}Ga_{18.4}$, $K_1 = 3.5e4$ J/m$^3$ and $K_2 = -8e4$ J/m$^3$ [138]. Inset graphs contain the probability density of the systems at Points 1 and 2

magnetization that produces Type I behavior. The only noticeable change in the MH curve is the final approach to saturation. This occurs when the location of peak probability is exactly at $\theta = \pi$, and instead of moving, it simply becomes more and more probable (i.e., corresponding to an increasingly large energy minima at that point).

Figure 3.6 (b) shows an MH curve for $\mathrm{Fe}_{79.1}\mathrm{Ga}_{20.9}$ produced using $K_1 = -1e3$ J/m$^3$ and $K_2 = 1e4$ J/m$^3$ [138] and placing the material under 50 MPa of compression. For this MCA energy, minima occur in the $\langle 100 \rangle$ family of directions when $h = 0$ and $\sigma = 0$. Applying stress causes the minima to appear exclusively in the $\langle 100 \rangle$, $\langle \bar{1}00 \rangle$, $\langle 010 \rangle$, and $\langle 0\bar{1}0 \rangle$ directions (i.e., $\pm x$ and $\pm y$). To plot the 2D probability landscape in a single line the inset of Figure 3.6 (b) shows $P(\theta) = P(\theta, \phi = \pi/4)$. In the inset of Figure 3.6 (b) the exact same trend as the inset of Figure 3.6 (b) is observed. Starting at Point 1, $\mu_0 H = 15$ mT, and moving to point 2, $\mu_0 H = 20$ mT, we see the same gradual shift in the probable direction of magnetization which produces Type I behavior.

Finally, 3.6 (c) shows an MH curve for $\mathrm{Fe}_{81.6}\mathrm{Ga}_{18.4}$ produced using $K_1 = 3.5e4$ J/m$^3$ and $K_2 = -8e4$ J/m$^3$ [138] and placing the material under 50 MPa of compression. Of note the points of interest were specifically chosen to highlight the Type II transition from concave up to down and again occur at $\mu_0 H = 15$ mT and 20 mT. Also, as this is another cubic material, the single line plotted in the inset graph is the maximum probability, $P(\theta) = P(\theta, \phi = 0)$. At Point 1 the direction with the highest probability is slightly to the right of $\theta = \pi/2$. However, as we move to Point 2 there is a significant change in the probability landscape. The global minimum abruptly shifts to $\theta = \pi$ and an additional probability peak emerges. This abrupt change in the probable direction of magnetization is what causes the magnetization curve to change from concave up to down, and the presence of this second peak is what has kept the material from saturating. Due to the assumption of transversely isotropic MCA the model in this paper is incapable of simulating $\mathrm{Fe}_{81.6}\mathrm{Ga}_{18.4}$, or other materials with similar anisotropies that produce abrupt changes in the probability landscape.

## 3.4 Conclusion

This paper provides an analytical one-dimensional constitutive model for magnetostriction. Closed form analytical solutions were provided to calculate the average magnetization, magnetostriction, susceptibility, compliance, and piezomagnetic coupling coefficient. Additionally, it was demonstrated that the analytical model maintains numerical accuracy over a large range of applied magnetic fields and stress / anisotropy conditions. Finally, the model was used to simulate experimental data for three different materials. This comparison only required fitting two model parameters to the data. Comparisons between the experimental and modeled results indicate that the model is capable of simulating Terfenol-D and is expected to also accurately describe certain cubic materials as long as they have probability landscapes that are well approximated as transversely isotropic.

# Chapter 4

# Considerations for Numerical Approximations of Two-Dimensional Models of Magnetostriction

## Attribution

This chapter, a collaborative work with John P. Domann, is ready for submission to the Journal of Physics A: Mathematical and Theoretical

## Author Contributions

Imhof and Domann conceived of the project. Imhof was responsible for developing the constitutive model and implementing it in code, verified the numerical accuracy of the model and compared the model to experimental data. Imhof also prepared the initial draft of the manuscript and its associated visuals and coordinated the revisions. All of this was done with supervisory assistance from Domann, who also reviewed and edited the work at all stages until publication.

## 4.1 Introduction

Magnetostrictive materials possess energy densities, actuation strains, and response times that can improve the performance of actuators, sensors, and energy harvesting devices [42, 56, 59, 104, 110, 126, 172, 173, 183, 186]. A magnetostrictive device's utility stems from the material's strongly coupled highly nonlinear magneto-mechanical behavior. However, these features also make designing magnetostrictive technologies challenging, which is why accurate models are needed during the design process. Unfortunately, it is difficult to accurately model the nonlinear magneto-mechanical constitutive behavior, with existing models having numerous deficiencies. These difficulties ultimately hinder the development of future magnetostrictive technologies.

The main difficulty in modeling magnetostrictive materials originates from their macroscale response being dependent on complex microscale physics. At the microscale, the competition between various energies results in the formation of magnetic domains. The observed macroscale magnetization and magnetostriction are then dependent on the domain structure's evolution under varying magnetic and mechanical loads. While micromagnetic simulations provide the most accurate continuum models of magnetostriction [19, 86, 112, 113, 175], they become numerically intractable for model volumes on the order of $10\mu m^3$ or greater [11, 70, 75, 108, 165, 176]. Equilibrium statistical mechanics offers a useful way to bridge micromagnetics to larger size scales.

Models constructed with statistical mechanics can potentially model paramagnetic, ferromagnetic, ferrimagnetic, antiferromagnetic, and magnetostrictive materials [23, 50, 95, 154]. Although models derived using statistical mechanics are theoretically capable of accurately simulating all of the aforementioned materials, the requisite integral equations generally lack closed form solutions. As a result, only a limited number of analytical statistical mechanics models exist for magnetostrictive materials, all for highly specific material symmetries and loading cases [89, 139, 159]. For example, the authors have previously derived an analytical model in which the combined magnetostrictive and magnetocrystalline anisotropies (MCAs) were transversely isotropic, and the magnetic field was parallel to the unique transverse axis [89]. Statistical models with more general loading conditions and anisotropy typically require numerical approximation [8, 9, 10, 14, 16, 38, 53, 67, 68, 127, 160, 169]. Numerical approximations often reduce the number of degrees of freedom to improve computational efficiency, so that they may be leveraged in high fidelity simulations (e.g., finite element models for device design). A key concern for these models is ensuring that any simplifying assumptions do not hinder the model's ability to simulate observed magneto-mechanical behaviors or introduce any artificial spurious responses.

Several of the approximation methods typically used in statistical mechanics and magnetostrictive modeling use quadratures of the form,

$$F = \int_a^b f(x)\,dx \approx \int_a^b \sum_{k=1}^{N} w_k \tilde{f}(x; x_k)\,dx, \tag{4.1}$$

where $N$ is the number of quadrature points, $x_k$ are the quadrature points, $w_k$ are weights, and $\tilde{f}(x; x_k)$ approximates $f(x)$. Developing a numerical quadrature requires determining the 1) quadrature points $x_k$, 2) weights $w_k$, and 3) approximation functions $\tilde{f}(x; x_k)$ that are accurate, integrable, and computationally efficient. Laplace's Method (LM), which is perhaps the most common approximation technique in statistical mechanics, is exactly of this form [7, 34, 106]. This method tries to provide accurate approximations while using only a small set of well-chosen highly significant quadrature points. That is in distinct contrast with other techniques like Riemann sums which achieve high numerical accuracy by increasing the number of quadrature points N until convergence. While Riemann sums can ensure accuracy, that approach reduces computational efficiency. This paper is largely focused on analyzing methods that utilize a small number of quadrature points.

LM is a classical approach for approximating integrals of exponential functions with integrands of the form $f(x) = g(x)\exp(\mathcal{M}h(x))$, where $\max_{a\leq x\leq b}|h(x)| = 1$, and the scalar $\mathcal{M}$ controls the maximum value of the integrand. The simple principle guiding LM is that when $\mathcal{M} >> 1$ the maxima of $h(x)$ will control the value of the integral. In terms of Equation (4.1) LM has weights $w_k$ and approximation function $\tilde{f}(x; x_k)$ that are determined by approximating $h(x)$ with a second order Taylor series expansion about its maxima. Conceptually, by using significant quadrature points with locally accurate approximations, LM trades the difficulty of evaluating the requisite integral for the difficulty of locating the maxima. LM is expected to have an accurate solution when the integrand is well approximated by non-overlapping unnormalized Gaussian distributions. The approximation error of LM for one dimensional functions asymptotically converges with err $\approx |\mathcal{M}|^{-1}$ as $\mathcal{M} \to \infty$ [25, 134, 163, 164]. LM can fail when $\mathcal{M} << 1$, in which case even the minima of $f(x)$ add a non-trivial contribution to the integral.

LM is often used in statistical mechanics to approximate integrands $f(x) \propto \exp(-G(x))$ where $G(x)$ is the microscale free energy of the system normalized w.r.t. the thermal energy [7, 34, 106]. The quadrature points in these approximations are the energy minima which are the most probable states of the system. While LM is a well established standard technique with known numerical properties, a variation of it is commonly encountered in the magnetostrictive modeling literature.

This variation is the Discrete Energy Average (DEA) model which has shown an excellent ability to fit experimental data [67, 68, 127, 160, 169]. Similar to LM, the DEA model aims to use microscale energy minima as the quadrature points and attempts to approximate a Boltzmann distribution. While the DEA literature makes no reference to LM, in the present authors' opinion the DEA model can be seen as a simplification of LM. This statement will be revisited in Section 4.4.2 of the Results. Key differences between the DEA model and LM are that compared to LM the DEA model 1) uses simplified weights $w_k$ that ignore contributions from the local neighborhood of each quadrature point, and 2) uses its own approximate linearized extrema finding method to attempt to locate the energy minima. Analysis of the accuracy of both points is provided below in Sections 4.3.2 and 4.4.1. Even though there are significant similarities between the DEA model and LM, the authors have not found any reference to LM in the DEA literature [38, 67, 68, 127, 160]. While the numerical properties of LM are known, those of the DEA model have not been previously reported. One contribution of the current work is to provide an initial analysis of the DEA models' numerical accuracy.

It is worth mentioning that there have been several iterations of the DEA model [67, 68, 127, 160, 169], and this paper only analyzes the most recent version. Two main differences exist between the different iterations, 1) the forms of the microscale free energy, and 2) the methods used to find the energy minima. Both the earliest and most recent DEA models use well defined energy densities with cubic MCA and magnetostriction that are commonly encountered in the field of micromagnetics [24, 41, 49, 67, 133, 169]. The resulting DEA models then approximate the statistical mechanics of a paramagnet by neglecting the exchange energy. In contrast, the remaining DEA papers describe an ensemble of spin variants, one per MCA easy direction, with each variant having a quadratic free energy [68, 127, 160]. Exchange is again ignored. The DEA literature has shown that this ensemble can be curve fit to experimental data for single and polycrystalline cubic materials loaded along a single axis [68, 115, 127, 160]. However, the authors note that the ensemble energy is not derived from a valid continuum energy. Additionally, in the supplemental section of the author's previous work, it was shown that the DEA ensemble can artificially change the anisotropy of the modeled system (e.g., isotropic / constant energies influence the macroscale response of the material)[89]. Therefore, DEA can effectively create an unintended 'numerical anisotropy'.

The other key difference between DEA models is the method used to approximate microscale energy minima. The minima finding procedures leverage either Newton's method [67], or a single step update of either the quadratic variant energies [68, 127, 160] or a quadratic expansion of a continuous micromagnetic energy [169]. While Newton's method can guarantee accurate minima, it almost always requires multiple iterations before converging. Alternatively, the single step update is faster but has limited accuracy. In this work, the model proposed by Wahi *et al.* will be used as the reference model [169]. This iteration of DEA has been chosen because it uses a valid micromagnetic energy, which allows the present authors to compare the numerical accuracy of multiple extrema finding methods and approximation functions developed for a relevant magnetostrictive system.

This paper presents an analysis of several quadrature methods and shows how the numerical accuracy of the approximation techniques impacts the validity of the resulting magnetostrictive constitutive models. Of the four approximation techniques studied, two already exist in the literature (LM and DEA), while the remaining two were developed by the authors. One uses a wrapped normal mixture distribution (WNM) to eliminate several restrictive assumptions inherent to LM. The other performs numerical integration using a quadratic spline approximation (QSA) of the microscale energy of the system. The numerical accuracy for each method is presented, and the influence of this accuracy on the model's predictions is analyzed. Finally, the ability of the most accurate method to simulate experimental data from the literature is tested. Results show that when inaccurate numerical approximations are used the resulting constitutive models have degenerate / non-physical behaviors that limit their utility. However, there are expected trade-offs between ensuring the numerical accuracy of a model, and its computational efficiency. Finally, we'll see that ensuring the numerical accuracy of a paramagnetic model does not ensure the model is able to accurately describe a real ferromagnetic material.

## 4.2 Background

### 4.2.1 Statistical Mechanics of Magnetostriction

In this section, an outline of the basic theory for developing a nonlinear constitutive model of magnetostrictive materials using Boltzmann statistics is provided. The Gibbs Canonical Ensemble is used to model a magnetostrictive material in thermal equilibrium with a heat bath at constant temperature (i.e., the environment), capable of having work done on it. Equations (4.2) - (4.4) calculate the partition function $\mathcal{Z}$ and the expected macroscale free energy $\langle G \rangle$ for a given microscale (Landau) free energy $G_L$, where the integrand $\mathcal{B}(\boldsymbol{m})$ is the Boltzmann factor [24].

$$\mathcal{Z} = \int_{\mathbb{M}} \mathcal{B} \, \mathrm{d}\boldsymbol{m} \tag{4.2}$$

$$\langle G \rangle = -k_b \mathrm{T} \ln \mathcal{Z} \tag{4.3}$$

$$\mathcal{B} = \exp\left( -\frac{G_L(\boldsymbol{m})}{k_b \mathrm{T}} \right) \tag{4.4}$$

In Equations (4.2) - (4.4) $k_b\mathrm{T}$ is the thermal energy and integration is over all possible states of the system (i.e. $\mathbb{M}$ is the set of all admissible magnetization distributions $\boldsymbol{m}(\boldsymbol{x})$ for the body). The microscale free energy contains any of the relevant energy densities used in micromagnetics. This allows the impact of applied magnetic fields $\boldsymbol{H}_a$, magnetostatic / demag fields $\boldsymbol{H}_{ms}$, stresses $\boldsymbol{T}$, MCA, and exchange energy to be incorporated [24, 41, 49, 50, 94, 105, 133].

A key simplifying assumption in this work, and all prior DEA models, is that the material is paramagnetic (i.e., there is zero exchange coupling). Therefore, the model predicts the pointwise macroscale response is due to the statistics of an isolated spin interacting with its environment. This removes the need to integrate over all distributions $\mathbb{M}$ and instead restricts integration to all orientations of a single magnetic spin. It is common in the literature to develop paramagnetic models and then augment them with an effective field to provide a first order theory of ferromagnetism [24, 49, 50, 94]. While it is straightforward to introduce an effective field $\boldsymbol{H}_e = \boldsymbol{H} + \alpha \langle \boldsymbol{M} \rangle$ into any paramagnetic model, doing so requires using an implicit nonlinear solver while only approximating the exchange interaction. Mean field theory is not used in the present work.

Due to the paramagnetic assumption Equations (4.2) - (4.4) transition to,

$$z = \int_{\mathcal{S}^2} b(\boldsymbol{m}) \, \mathrm{d}\boldsymbol{m}, \tag{4.5}$$

$$\langle g \rangle = -\beta^{-1} \ln z, \tag{4.6}$$

$$b(\boldsymbol{m}) = \exp(-\beta g_L(\boldsymbol{m})), \tag{4.7}$$

where the lowercase terms Equations (4.5) - (4.7) are understood to be the respective volumetric densities of Equations (4.2) - (4.4), $\beta^{-1}$ is the thermal energy density, and integration is restricted to all orientations $\boldsymbol{m} \in \mathcal{S}^2$ (i.e., over the unit sphere).

Given the microscale free energy density $g_L$ all macroscale properties can be calculated from the partition function $z$ in Equation (4.5). The free energy density considered in this work is composed of Zeeman $g_Z$, magnetoelastic anisotropy $g_{ME}$, and magnetocrystalline anisotropy $g_{MCA}$ energy densities,

$$g_L(\boldsymbol{m}; \boldsymbol{H}_a, \boldsymbol{T}, \boldsymbol{K}) = g_Z(\boldsymbol{m}; \boldsymbol{H}_a) + g_{ME}(\boldsymbol{m}; \boldsymbol{T}) + g_{MCA}(\boldsymbol{m}; \boldsymbol{K}), \tag{4.8}$$

where the notation $g(\boldsymbol{m};...)$ indicates $\boldsymbol{m}$ is a prescribed parameter, and $\boldsymbol{K} = \{K_1, K_2\}$ contains the cubic MCA coefficients [24]. The individual micromagnetic energies for a cubic material are defined as follows,

$$g_Z(\boldsymbol{m};\boldsymbol{H}_a) = -\mu_0 M_s \boldsymbol{m} \cdot \boldsymbol{H}_a, \tag{4.9}$$

$$g_{ME}(\boldsymbol{m};\boldsymbol{T}) = -\frac{3}{2}\lambda_{100}\sum_i \left(m_i^2 - \frac{1}{3}\right) T_{ii} - 3\lambda_{111}\sum_{i\neq j} m_i m_j T_{ij}, \tag{4.10}$$

$$\begin{aligned} g_{MCA}(\boldsymbol{m};\boldsymbol{K}) =& (K_1 + \Delta K_{\boldsymbol{T}})\left(m_x^2 m_y^2 + m_x^2 m_z^2 + m_y^2 m_z^2\right) + K_2\left(m_x^2 m_y^2 m_z^2\right), && (4.11)\\ \Delta K_{\boldsymbol{T}} =& (9/4)\left((c_{11}-c_{12})\lambda_{100}^2 - 2c_{44}\lambda_{111}\right), && (4.12)\end{aligned}$$

where $\mu_0$ is the permeability of free space, $M_s$ is the saturation magnetization, $\lambda_{100}$ and $\lambda_{111}$ are the saturation magnetostriction constants, and $c_{ij}$ are the elastic moduli. As stress $\boldsymbol{T}$ is used as an independent variable instead of strain $\boldsymbol{\varepsilon}$, the material deforms when $\boldsymbol{m}$ changes, which causes the magnetostrictive coupling to contribute $\Delta K_{\boldsymbol{T}}$ to the MCA [99]. In terms of spherical coordinates, the Cartesian components of the microscale magnetization and magnetostriction are given by,

$$m_i(\theta,\phi) = \begin{bmatrix} \cos(\theta)\cos(\phi) \\ \cos(\theta)\sin(\phi) \\ \sin(\theta) \end{bmatrix}, \tag{4.13}$$

$$\varepsilon_{ij}^{m}(\boldsymbol{m}) = \begin{bmatrix} \frac{3}{2}\lambda_{100}\left(m_x^2 - \frac{1}{3}\right) & 3\lambda_{111}m_xm_y & 3\lambda_{111}m_xm_z \\ 3\lambda_{111}m_xm_y & \frac{3}{2}\lambda_{100}\left(m_y^2 - \frac{1}{3}\right) & 3\lambda_{111}m_ym_z \\ 3\lambda_{111}m_xm_z & 3\lambda_{111}m_ym_z & \frac{3}{2}\lambda_{100}\left(m_z^2 - \frac{1}{3}\right) \end{bmatrix}. \tag{4.14}$$

Once the partition function and macroscale energy density are constructed the equilibrium magnetization $\langle \boldsymbol{M} \rangle = (-1/\mu_0)\partial \langle g \rangle / \partial \boldsymbol{H}$, and magnetostriction $\langle \boldsymbol{\varepsilon}^m \rangle = -\partial \langle g \rangle / \partial \boldsymbol{T}$ are calculated by taking partial derivatives using classical thermodynamics. Evaluating the derivatives also leads to the definition of the probability density function (PDF) $P$ and associated thermodynamic average $\langle \boldsymbol{A} \rangle$ of any microscale property $\boldsymbol{A}(\boldsymbol{m})$,

$$P(\boldsymbol{m}; \boldsymbol{H}_a, \boldsymbol{T}, \boldsymbol{K}, \beta) = \frac{1}{z}\exp\left(-\beta g_L(\boldsymbol{m}; \boldsymbol{H}_a, \boldsymbol{T}, \boldsymbol{K})\right), \tag{4.15}$$

$$\langle \boldsymbol{A} \rangle = \int_{\mathcal{S}^2} \boldsymbol{A}(\boldsymbol{m}) P(\boldsymbol{m}; \boldsymbol{H}_a, \boldsymbol{T}, \boldsymbol{K}, \beta) \mathrm{d}\boldsymbol{m}. \tag{4.16}$$

Applying Equations (4.15) and (4.16) to $\boldsymbol{m}$ and $\boldsymbol{\varepsilon}^m$ provides the expected macroscale magnetization $\langle \boldsymbol{M} \rangle$ and magnetostriction $\langle \boldsymbol{\varepsilon}^m \rangle$,

$$\langle \boldsymbol{M} \rangle = M_s \langle \boldsymbol{m} \rangle, \tag{4.17}$$

$$\langle \boldsymbol{\varepsilon}^m \rangle = \langle \boldsymbol{\varepsilon}^m(\boldsymbol{m}) \rangle. \tag{4.18}$$

Note that the macroscale quantity of interest is the thermodynamic average of the relevant micromagnetic quantity. The goal of any approximation is then to define a suitable $\tilde{z}$, along with its associated $\tilde{P}$ and $\langle ... \rangle_{approx}$ operator, that approximates the definitions provided in Equations (4.7) - (4.18). A tilde in any future expressions should be understood to denote an approximate quantity.

### 4.2.2 Thin Film Restrictions

While generating a general 3D model is a goal for this line of research, all of the approximations discussed below require locating energy extrema. At present, finding the energy extrema for the general 3D case is not computationally efficient enough for use in FEA simulations. The authors note that locating the energy extrema in 3D depends on multivariate polynomial root finding, which is still an active area of research in its own right [17, 20, 21, 27, 29, 62, 92, 116, 120, 124, 132, 136, 137, 156, 162]. In contrast, there are known accurate and efficient methods of 1D extrema finding. The Fourier companion matrix method, presented by Boyd *et al.* [28, 30] and summarized in B.4, can be used to find the extrema of functions defined on the unit circle. That method can be applied here if the microscale free energy density is restricted to $\theta = \pi/2$, which can be used to approximate the response of a thin film. Applying this thin film restriction reduces the partition function to,

$$z = \int_0^{2\pi} \exp\left(-\beta g_L(\phi)\right) \mathrm{d}\phi. \tag{4.19}$$

In the following section, the thin film restriction will be applied to LM, WNM, and QSA. The DEA model has always been presented as a general 3D model and so when comparing the numerical accuracy of each approximation technique in Sections 4.4.1 and 4.4.2 the DEA model is only subject to thin film loading conditions, but the previously reported 3D equations are used.

## 4.3 Numerical Approximation Techniques

In Section 4.2 it was highlighted that the requisite integral equations for the macroscale material properties are all dependent on PDFs. In this section, we note that LM and the DEA model operate by approximating $P$ in Equation (4.16) with a mixture distribution $\tilde{P}$. Given a finite set of PDFs and weights $\overline{w}_k > 0$, a mixture distribution is defined as

$$\tilde{P}(\boldsymbol{m}; \{w\}, \{\nu\}) = \sum_{k=1}^{N} \overline{w}_k P(\boldsymbol{m}; \nu_k), \tag{4.20}$$

$$\overline{w}_k = \frac{w_k}{\sum_{k=1}^{N} w_k}, \tag{4.21}$$

where $N$ is the number of individual PDFs, the normalized weights $\overline{w}_k$ sum to 1, and $\nu_k$ is a parameter set needed to define each $P$. One of the parameters in $\nu_k$ is always the quadrature points (e.g., if $P$ is a Gaussian PDF then $\nu_k = \{\mu_k, \sigma_k\}$ contains the mean and standard deviation, with the mean acting as a quadrature point). Rewriting Equations (4.5) and (4.16) in terms of a mixture distribution yields,

$$\tilde{z} = \sum_{k=1}^{N} w_k \int_{\Gamma} P(\boldsymbol{m}; \nu_k) \mathrm{d}\boldsymbol{m} = \sum_{k=1}^{N} w_k, \tag{4.22}$$

$$\left\langle \tilde{\boldsymbol{A}} \right\rangle = \sum_{k=1}^{N} \overline{w}_k \int_{\Gamma} \boldsymbol{A}(\boldsymbol{m}) P(\boldsymbol{m}; \nu_k) \mathrm{d}\boldsymbol{m}, \tag{4.23}$$

where $\Gamma$ are the bounds of integration that correspond to the chosen PDF $P$. After choosing quadrature points $\boldsymbol{m}_k$ with PDFs $P$ and weights $w_k$, any macroscale property can be approximated by using Equations (4.22) and (4.23).

### 4.3.1 Laplace's Method

In what follows, the authors assume the reader to be familiar with the basic derivation of Laplace's Method. For while the following equations are by no means a conventional depiction of LM, nor should they be misconstrued as *deriving* LM, it's nonetheless true that LM is consistent with the equations presented in this section (i.e., they both produce the same final approximations).

As previously stated, a key principle guiding LM is that the energy minima of the microscale free energy density $g_L(\boldsymbol{m})$ will dominate the resulting value of the integrals in Equations (4.5) and (4.16) for $z$ and $\langle \boldsymbol{A} \rangle$. As a result, the free energy minima are used as the quadrature points $\boldsymbol{m}_k$. By analyzing the standard derivation of LM, we're led to conclude that

$$P_{LM}(\boldsymbol{m};\boldsymbol{m}_k) = \delta(\boldsymbol{m}-\boldsymbol{m}_k), \tag{4.24}$$

$$w_k = \left(\frac{2\pi}{\beta}\right)^{3/2} \frac{\exp(-\beta g_L(\boldsymbol{m}_k))}{\|\mathrm{H}_k\|^{1/2}}, \tag{4.25}$$

where $\|\mathrm{H}_k\|$ is the Hessian determinant of $g_L$ evaluated at $\boldsymbol{m}_k$. After applying the thin film assumption Equations (4.24) and (4.25) transition to

$$P_{LM}(\phi;\phi_k) = \delta(\phi-\phi_k), \tag{4.26}$$

$$w_k = \exp(-\beta g_L(\phi_k))\sqrt{\frac{2\pi}{\beta\, g_{L,\phi\phi}(\phi_k)}}, \tag{4.27}$$

where the notation $f_{,xx}(x) = \partial^2 f(x)/\partial^2 x$. As promised, substituting the weights and PDFs into Equation (4.22) reproduces the standard LM approximation of the partition function as shown in Chapter 27 of *Information Theory, Inference, and Learning Algorithms* [114],

$$\tilde{z}_{LM} = \sum_{k=1}^{N} \exp(-\beta g_L(\phi_k)) \sqrt{\frac{2\pi}{\beta\, g_{L,\phi\phi}(\phi_k)}}. \tag{4.28}$$

Note that the dependence of $w_k$ on the curvature of the free energy density allows LM to accurately approximate the partition function integrand in the neighborhood of each energy minima. We'll soon see that the DEA model does not include this factor. An initial look at a conventional depiction of LM may lead to the conclusion that $P$ should be a Gaussian distribution as they have the same weights. However, the authors note that the appearance of the Dirac delta function $\delta(\phi - \phi_k)$ emerges as a consequence of the fundamental LM assumption that when approximating $\boldsymbol{A}(\phi)\exp(-\beta g_L(\phi))$ the function $\boldsymbol{A}(\phi)$ is assumed to vary very slowly relative to the Boltzmann factor $\exp(-\beta g_L(\phi))$ near the energy minima. In that case, it is approximated as $\boldsymbol{A}(\phi_k)$, which the Dirac delta also produces. In the remainder of this paper, this assumption will be referred to as the Dirac delta assumption of LM. A consequence of the Dirac delta assumption of LM is that each of the PDFs in the mixture distribution are inherently isolated from one another and never overlap / interact. The unconventional presentation of LM here is intended to highlight this assumption.

Figure 4.1 highlights when Laplace's method is expected to have a valid approximation by comparing it to several possible Boltzmann factors. As the magnitude of the free energy minima increases the Boltzmann factor transitions from a base-like trigonometric function, shown with the dash-dotted orange line, to a sharp Gaussian peak, shown with the solid black line. The dashed green line schematically shows the Dirac delta function used in the LM approximation. With the proper weight we expect this assumption to be accurate when $|\min_\Gamma \beta g_L| \gg 1$. However, if $|\min_\Gamma \beta g_L|$ is on the order of 1 or smaller then this Dirac delta curve will be unable to accurately approximate the Boltzmann factor.

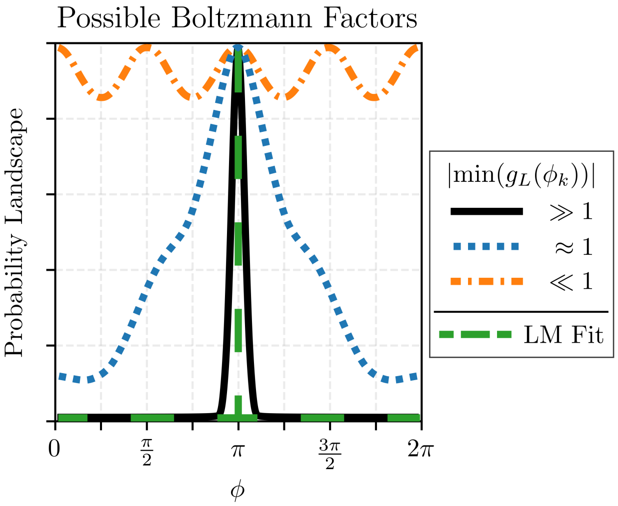

Figure 4.1: Different Boltzmann Factors dependent on the magnitude of the minima of the microscale free energy density and the Dirac delta function used in the LM approximation.

### 4.3.2 DEA

The model proposed by Wahi *et al.* serves as the starting point for this discussion [169]. While the DEA model is not typically presented as a mixture distribution the following equations are consistent with those in Wahi *et al.*, producing the same final approximations.

As stated earlier, the DEA model uses its own procedure to approximate the location of the energy minima of the microscale free energy. The approximate energy minima locations are then used as quadrature points $\boldsymbol{m}_k$. Analyzing the equations presented in the DEA literature [67, 68, 127, 160, 169] the authors once again conclude that the chosen PDF is the Dirac delta,

$$P_{DEA}(\boldsymbol{m}; \boldsymbol{m}_k) = \delta(\boldsymbol{m} - \boldsymbol{m}_k). \tag{4.29}$$

If the Dirac delta is the chosen PDF then the weights for the DEA model must be,

$$w_k = \exp(-\beta g_L(\boldsymbol{m}_k)). \tag{4.30}$$

This combination of weights and PDF reproduces the DEA approximation for magnetization as shown in Wahi *et al.*,

$$\left\langle \tilde{\boldsymbol{M}} \right\rangle_{DEA} = \frac{M_s \sum_{k=1}^{N} \boldsymbol{m}_k \exp(-g_L(\boldsymbol{m}_k)/\Omega)}{\sum_{k=1}^{N} \exp(-g_L(\boldsymbol{m}_k)/\Omega)}, \tag{4.31}$$

where $\Omega$ is referred to as a smoothing parameter in the DEA literature but is a thermal energy density when using Boltzmann statistics (i.e., $\Omega = \beta^{-1}$). By examining the DEA approximations of magnetization and magnetostriction the DEA average operator is understood to be,

$$\left\langle \tilde{\boldsymbol{A}} \right\rangle_{DEA} = \frac{\sum_{k=1}^{N} A(\boldsymbol{m}_k) \exp(-g_L(\boldsymbol{m}_k)/\Omega)}{\sum_{k=1}^{N} \exp(-g_L(\boldsymbol{m}_k)/\Omega)}. \tag{4.32}$$

By making the Dirac delta assumption the DEA model is also expected to accumulate error if $|\min_\Gamma \beta g_L| \gg 1$ is on the order of 1 or smaller. Furthermore, note that unlike LM this weight has no knowledge of the local curvature of the energy, which is also expected to contribute error.

### 4.3.3 Wrapped Normal Mixture (WNM)

The next approach is a generalization of LM that removes some of its inherent assumptions and restrictions. In this approach, which uses a wrapped normal mixture distribution, both energy minima and maxima are used as quadrature points $\phi_k$. While the minima of the microscale free energy density are the most probable states of the system, there are many cases in which the maxima are not negligible. In general, providing the quadrature method with additional significant quadrature points should improve the numerical accuracy of the approximation over a larger range of test cases (i.e., not just in the limit $|\min_{\Gamma} \beta g_L| \gg 1 \to \infty$).

The key idea behind the WNM method is to utilize a mixture PDF that has properties similar to those of the integrand being approximated. A key feature of the integrands for paramagnets is that they're periodic functions residing on the unit sphere (or circle). The general form of a wrapped normal distribution is,

$$P_{WN}(\phi; \mu_k, \sigma_k) = \frac{1}{\sqrt{2\pi}\sigma_k} \sum_{j=-\infty}^{\infty} \exp\left(\frac{-(\phi - \mu_k + 2\pi j)^2}{2\sigma_k^2}\right), \tag{4.33}$$

where $\mu_k$ is the mean, $\sigma_k$ the standard deviation of the unwrapped normal distribution, and the bounds of integration $\Gamma$ are any interval of length $2\pi$. In order to fit the wrapped normal distribution to the requisite integrals it is initially assumed that each PDF $P$ is isolated. It is also assumed that $\sigma_k$ is obtained from the curvature of the free energy density as,

$$\sigma_k = \frac{1}{\sqrt{|-\beta g_{L,\phi\phi}(\phi_k)|}}. \tag{4.34}$$

As the WNM method uses both maxima and minima as its quadrature points, the absolute value of the curvature is now required to properly define a mixture distribution. After setting $\mu_k = \phi_k$, the isolated weights are found to be

$$w_k = \sqrt{2\pi}\sigma_k \exp(-\beta g_L(\phi_k)). \tag{4.35}$$

However, in an effort to eliminate the Dirac delta assumption we note that the PDFs of the mixture distribution just defined are not inherently isolated. Figure 4.2 shows how numerical error accrues when using the initial isolated weights if neighboring extrema are close to each other or $|\min_\Gamma \beta g_L| \gg 1$ is not large enough. The solid blue line is the Boltzmann

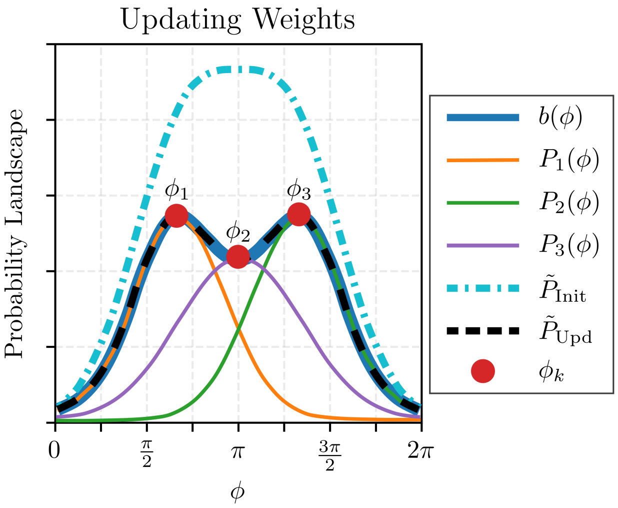
Updating Weights

Figure 4.2: A comparison of WNM approximations made with weights calculated for isolated peaks $\tilde{P}_{\text{Init}}$ and updated weights $\tilde{P}_{\text{Upd}}$.

factor $b(\phi) = \exp(-\beta g_L(\phi))$ which we are approximating. At each energy extremum $\phi_k$ an individual wrapped normal PDF was fit with the isolated weights (Equations 4.33 - 4.35). Summing these terms in an initial mixture distribution produces the dash-dotted cyan line $\tilde{P}_{\text{Init}}$. Notice that because the individual PDFs overlap so significantly the initial sum overestimates the actual integrand $b(\phi)$.

To improve the WNM approximation the initial isolated weights were updated by solving a set of linear equations to ensure the approximation matches the desired solution at the quadrature points. This is done by setting $\tilde{P}_{WN}(\phi_i) = \sum_{k=1}^{N} P_{WN}(\phi_i; \mu_k, \sigma_k) = b(\phi_i)$. By first defining the matrix $P_{ij} = P_j(\phi_i; \mu_j, \sigma_j)$, we have

$$\sum_{j=1}^{N} P_{ij} w_j = \exp(-\beta g_L(\phi_i)). \tag{4.36}$$

This equation can be solved for the updated weights $w_j$. The updated mixture is shown with the dashed black line $\tilde{P}_{\text{Upd}}$ in Figure 4.2. When solving these equations, we note that the weights of a mixture distribution are required to be positive and so the authors used the Matlab function `lsqnonneg()` to solve Equation (4.36) and guarantee that $w_k > 0$. Additionally, the authors note that updating the weights does not guarantee that the approximation is numerically accurate. With the mixture distribution, there is a linear dependence on the weights, but a nonlinear dependence on the other parameters ($\mu_k$ and $\sigma_k$). A more accurate solution would update all parameters, while the current approach was chosen for speed and simplicity. In what follows the weights $w_k$ used by the WNM method were those found with the update procedure.

### 4.3.4 Quadratic Spline Approximation (QSA)

In this subsection, the authors propose a new approximation technique that uses a quadratic spline approximation of the microscale free energy density $g_L(\phi)$. This is in contrast to all of the previous techniques which have approximated the Boltzmann factor $b(\phi) = \exp(-\beta g_L(\phi))$. The set of quadratic approximation functions $s_k(\phi)$ have the following form,

$$\tilde{g}_L(\phi) = \sum_{k=1}^{n-1} s_k(\phi), \tag{4.37}$$

$$s_k(\phi) = a_k\phi^2 + b_k\phi + c, \text{ for } \phi \in [\phi_k, \phi_{k+1}],\ k = 1, 2, ..., n-1. \tag{4.38}$$

For this approximation, the domain of integration is divided by a set of knots $\phi_k$. Note that by approximating the microscale free energy with a quadratic spline it is guaranteed that the requisite integral equations will have closed form solutions. However, the closed form solutions of the magnetization and magnetostriction contain Dawson functions with complex arguments. Accurately and efficiently calculating the Dawson function with complex arguments is an active area of research [2, 3, 181, 185]. The authors found that no single Dawson function algorithm was numerically accurate enough for use in the QSA method and that the use of these algorithms in the QSA framework would not be computationally efficient enough for use in FEA simulations. The QSA method instead performs standard numerical integration of the requisite integral equations using the quadratic functions $s_k(\phi)$. The QSA model is expected to have a faster convergence rate than standard numerical integration using the original free energy while still maintaining high numerical accuracy.

Algorithm 1 was used to determine key regions at which to anchor each spline with a knot. An example using Algorithm 1 is shown in Figure 4.3. The for loop in Algorithm 1 is

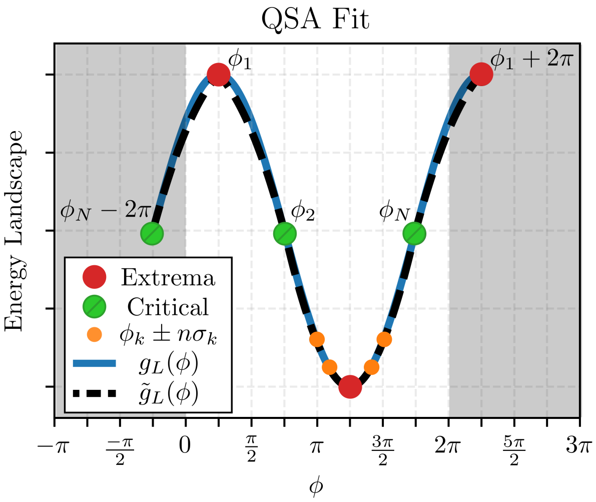

Figure 4.3: Example of QSA spline $\tilde{g}_L(\phi)$, built upon the knots $\phi_k$, fit to microscale free energy density $g_L(\phi)$.

used to improve the accuracy of the spline fit in the area surrounding energy minima. This is because the minima dominate most resulting integrals. Steps 8 and 9 of Algorithm 1 append quadrature points outside the bounds of integration, this is done to ensure that the splines fit at the bounds maintain the original function's periodicity. While the authors make no claims about Algorithm 1 being optimal, it will be shown that Algorithm 1 results

**Algorithm 1:** Find QSA knots $\phi_k$

```
Initialize $\phi_k$ with the extrema of $g_L(\phi)$                // $g'_L(\phi_k) = 0$
for $i$ = 1:number of $\phi_k$ do
    if $\phi_i$ is a minima then
        Append $\phi_i \pm \{n\}\sigma_i$ to $\phi_k$.*
Append critical points of $g_L(\phi)$ to $\phi_k$                  // $g''_L(\phi_j) = 0$
N = number of $\phi_k$
Sort $\phi_k$ in ascending order
Append $\phi_1 + 2\pi$ to $\phi_k$
Append $\phi_N - 2\pi$ to $\phi_k$
```

* Authors used $\{n\} = [\frac{1}{4}, \frac{1}{2}, \frac{3}{4}, 1]$

**Algorithm 2:** Fitting Quadratic Spline to microscale Free Energy

```
N = number of $\phi_k$
for $i$ = 1:N - 1 do
    Set $C_1 = -\beta g_L(\phi_i)$
    Set $C_2 = -\beta g_L(\phi_{i+1})$
    if $g_L(\phi_i) < g_L(\phi_{i+1})$ * then
        Set $C_3 = -\beta g_{L,\phi}(\phi_i)$
        Assign:
        $a_i = -\frac{C_1 - C_2 - C_3\phi_i + C_3\phi_{i+1}}{(\phi_i - \phi_{i+1})^2}$
        $b_i = -\frac{-2C_1\phi_i + 2C_2\phi_i + C_3\phi_i^2 - C_3\phi_{i+1}^2}{(\phi_i - \phi_{i+1})^2}$
        $c_i = -\frac{-C_2\phi_i^2 + 2C_1\phi_i\phi_{i+1} - C_3\phi_i^2\phi_{i+1} - C_1\phi_{i+1}^2 + C_3\phi_i\phi_{i+1}^2}{(\phi_i - \phi_{i+1})^2}$
    else
        Set $C_3 = -\beta g_{L,\phi}(\phi_{i+1})$
        Assign:
        $a_i = -\frac{-C_1 + C_2 + C_3\phi_i - C_3\phi_{i+1}}{(\phi_i - \phi_{i+1})^2}$
        $b_i = -\frac{(-C_3\phi_i^2 + 2C_1\phi_{i+1} - 2C_2\phi_{i+1} + C_3\phi_{i+1}^2}{(\phi_i - \phi_{i+1})^2}$
        $c_i = -\frac{-C_2\phi_i^2 + 2C_2\phi_i\phi_{i+1} + C_3\phi_i^2\phi_{i+1} - C_1\phi_{i+1}^2 - C_3\phi_i\phi_{i+1}^2}{(\phi_i - \phi_{i+1})^2}$
```

*This enforces $C^1$ continuity for the endpoint with lower energy, which contributes more to each integral

in accurate numerical approximations for all of the test conditions used in this paper. The authors note that an efficient adaptive algorithm could be developed that produces more accurate numerical approximations. The coefficients for the set of splines were calculated using Algorithm 2 and the generated list of knots.

## 4.4 Results and Discussion

This section provides 1) an assessment of the numerical accuracy and runtime of the DEA and Fourier extrema finding methods, 2) a comparison of the four approximation method's predictions of $z$, $\langle M_x \rangle$, and $\langle \varepsilon^m_{xx} \rangle$ to accurate numerical integration and their runtimes, 3) an assessment of how numerical accuracy affects the model's predictions, and finally 4) compares DEA to QSA, the most numerically accurate method, by assessing their ability to simulate the experimentally measured response for two different compositions of iron gallium.

### 4.4.1 Extrema Finding Analysis

The DEA model's approximate linearized extrema finder and the Fourier companion matrix method are both well described in existing literature [30, 169]. These methods are briefly summarized in B.2 and B.4 respectively. Two sets of $N = 10^5$ randomized applied loads $\boldsymbol{H}_a, \boldsymbol{T}$, and anisotropy coefficients $K_1$ were created to evaluate the numerical accuracy of the extrema locations returned by both methods. The magnitudes of $\boldsymbol{H}_a$, $\boldsymbol{T}$, and $K_1$ spanned from $10^{-4}$ to $10^5$. The first set of randomized loads, shown with the blue and hashed orange bars, were thin film loading conditions wherein the applied magnetic fields and principal stresses were restricted to the $xy$-plane (i.e., only have components in $\hat{\boldsymbol{\phi}}$). As the DEA model is depicted as a general 3D model, the DEA model was additionally tested with a second set of randomized loads, shown with the green hashed bars. For these loads, the applied magnetic fields and principal stresses were randomly applied in any direction. The accuracy of this data is vital for any method to be suitable for use in FEA calculations, where accuracy under arbitrary load conditions would be required. For each predicted extremum location, the first derivative $g'_L$ at that point was calculated. Additionally, the runtime of each procedure was recorded in order to analyze their computational efficiency.

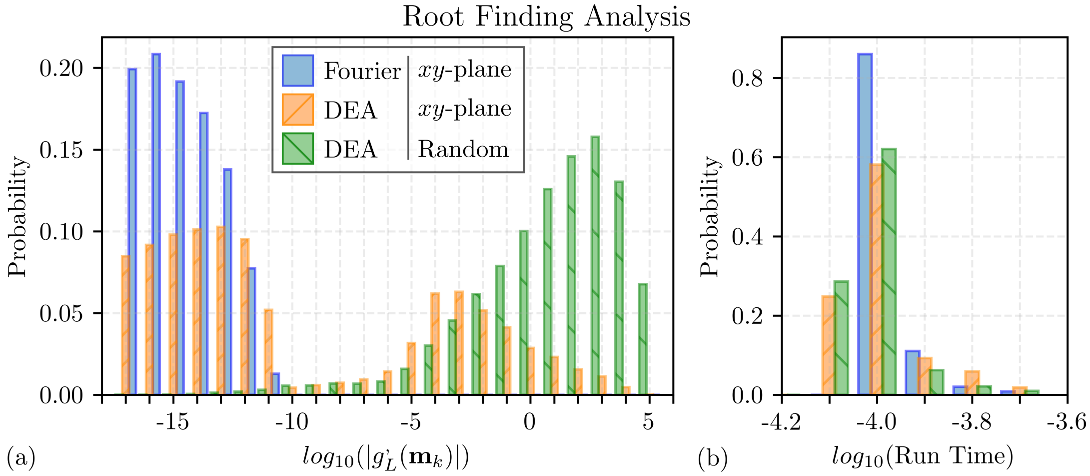

Figure 4.4: (a) Histogram of the numerical accuracy of the DEA and Fourier extrema finding techniques, when the magnetic field $\boldsymbol{H}_a$ and principal stresses of $\boldsymbol{T}$ are restricted to the $xy$-plane or both were applied randomly in any direction. (b) Histogram of the runtime for the DEA and Fourier methods.

The DEA results for the thin film configuration, the hashed orange data in Figure 4.4(a), have two distinct regions. The region $|-\beta g_L'(\boldsymbol{m}_k)| < 10^{-10}$ contains the extrema found in the $xy$-plane. These extrema don't leave the plane when $\boldsymbol{H}_a$ and $\boldsymbol{T}$ are applied. As a result, the DEA extrema finding technique can more easily identify them. The region from $10^{-5} < |-\beta g_L'(\boldsymbol{m}_k)| < 10^{5}$ are the extrema that were all initially parallel to $\hat{\theta}$ & $\hat{z}$ that move after applying the loads $\boldsymbol{H}_a$ and $\boldsymbol{T}$. These points represent 1/3 of the tested points.

The DEA results for fields in random directions, hashed green data in Figure 4.4(a), show that almost all the returned values are not extrema. Only 0.6% of the returned points have slopes smaller than $10^{-5}$. This figure highlights that the initial assumption of the DEA model, that the energy extrema remain close to the unloaded easy axes, is only valid when the magnitude of the applied fields is $\ll \beta^{-1}$. In that case, the applied loads barely move the initial MCA minima. The authors note that the entire logic behind using DEA (and LM) is predicated upon first locating the energy minima. So, this deficiency is expected to have a large negative impact on the overall accuracy of the method compared to the actual integrals.

Alternatively, the blue data in Figure 4.4(a) shows that 100% of the values returned by the Fourier method have slopes smaller than $10^{-10}$. The Fourier method is capable of finding numerically accurate extrema for all of the randomized loading conditions. The one drawback to this method is that it's only usable in thin-film models that require 1D root finding. Finally, Figure 4.4(b) shows that the Fourier method and the DEA extrema finding procedure have comparable average runtimes of around 0.1 ms. As the Fourier method always returns accurate extrema and has computationally efficient runtimes compared to the most popular magnetostrictive model in the literature, it was used to determine the quadrature points for each approximation technique aside from DEA. If a proper 2D generalization of the Fourier method is developed, the thin film assumptions present within this work can likely be removed.

### 4.4.2 Numerical Approximation Accuracy and Runtime

Table 4.1 summarizes the quadrature points, probabilities, and weights used for the first three approximation methods, while the QSA method is described in Algorithms 1 and 2. The $N = 10^5$ fields randomly rotated within the plane were used to evaluate the numerical accuracy of all four approximation methods.

Table 4.1: Mixture Distribution Comparison

| Method | $\phi_k$ | $P_k$ | $w_k$ |
|---|---|---|---|
| LM | Minima of $g_L(\phi)$ | $\delta(\phi - \phi_k)$ | $\exp(-\beta g_L(\phi_k))\sqrt{2\pi}\sigma_k$ |
| DEA | Approximate Extrema of $g_L(\boldsymbol{m})$ | $\delta(\boldsymbol{m} - \boldsymbol{m}_k)$ | $\exp(-\beta g_L(\boldsymbol{m}_k))$ |
| WNM | Extrema of $g_L(\phi)$ | Equation (4.33)* | Equation (4.36)** |

For each of the numerical approximations described in this paper, the accuracy of each method was compared relative to conventional numerical integration. For each set of fields, numerical integration was performed using Matlab's `integral()` function with relative and absolute errors of $10^{-16}$. The `integral()` function was given the locations of the energy extrema as waypoints to help ensure numerical accuracy. The relative errors for each value were calculated as $|f_{num} - f_{approx}|/f_{sat}$, where $f$ is the parameter of interest and $f_{sat}$ is the saturation value equal to $2\pi$, $M_s$, and $\lambda_{100}$ for the partition function, magnetization, and magnetostriction respectively. The $x$-axis of each plot is the is $|\min_\Gamma g_L|$, which will be referred to as x in the following discussion. Of note the DEA model is always presented as a general 3D model in the literature. So, while the loads used to evaluate DEA were restricted to the thin film conditions, the numerical integrals it was compared to utilized `integral2()` to solve Equation (4.5). Alternatively, the other three methods (LM, WNM, and QSA) were all compared to the requisite integral equations with the thin film assumption applied (e.g., Equation (4.19)).

Figures 4.5 (a) (b) and (c) plot the relative error of LM's approximations for $z$, $\langle M_x \rangle$, and $\langle \varepsilon_{xx}^m \rangle$. The magnetization $\langle M_x \rangle$ and magnetostriction $\langle \varepsilon_{xx}^m \rangle$ plots show a convergence rate of $\Theta(1/\mathrm{x}^{1.1})$ as x→ ∞, which is close to the expected convergence rate of LM. The partition function $z$ plot shows a steeper convergence rate $\Theta(1/\mathrm{x}^{1.5})$ as x→ ∞, slightly better than the expected rate. The numerical approximations are accurate when x $\gg$ 1. Also, as expected LM has inaccurate approximations when x is on the order of 1 or smaller. Of note, the large error that occurs in the partition function $z$ when x $\ll$ 1 is capped at 100% for both the magnetization $\langle M_x \rangle$ and magnetostriction $\langle \varepsilon_{xx}^m \rangle$. This occurs because the magnetization and magnetostriction are both divided by the partition function and so the error that occurs in both predictions is divided out.

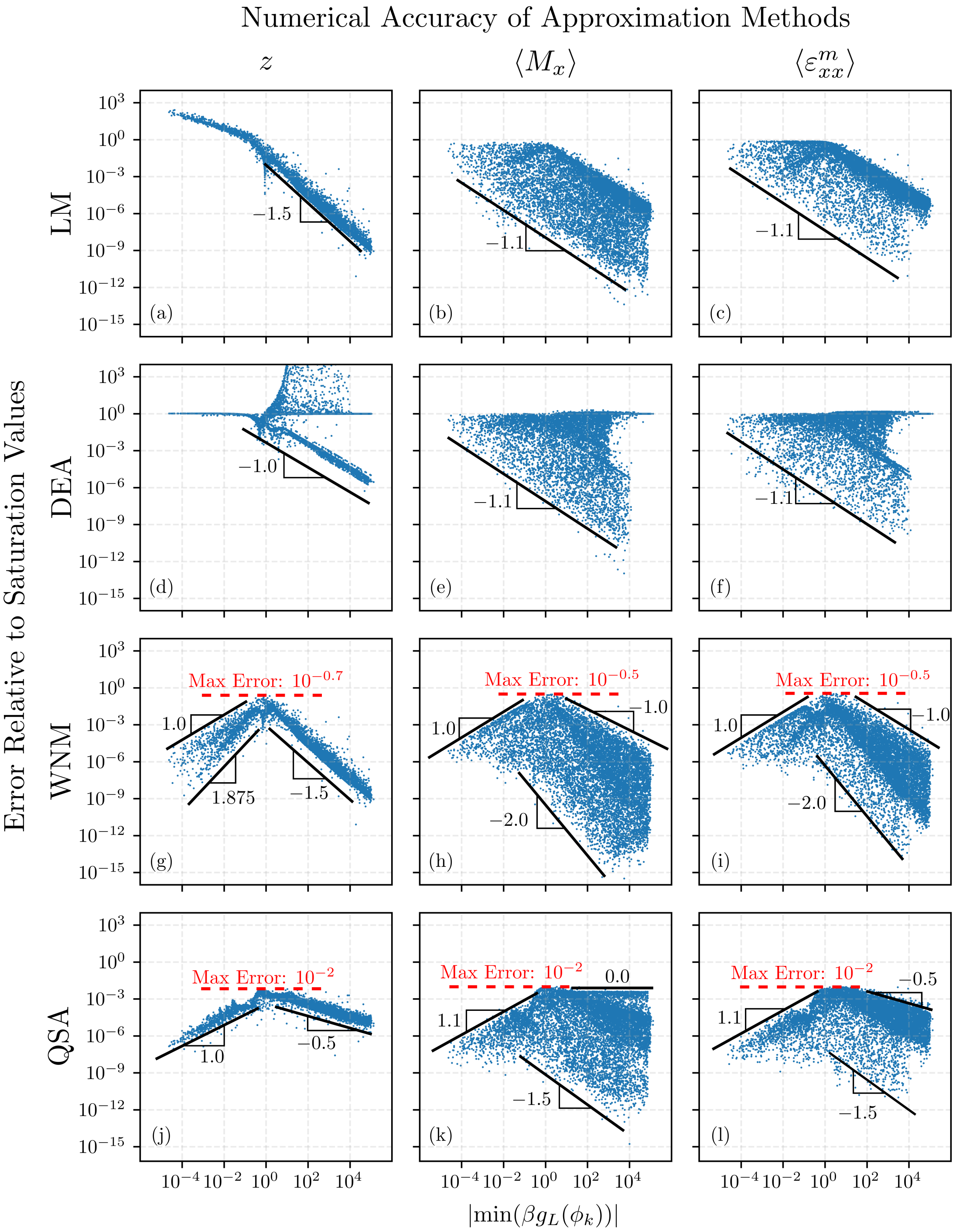

Figure 4.5: (a) Scatter plot of the Relative Error of the partition function $z$, $\langle M_x \rangle$, and $\langle \varepsilon^m_{xx} \rangle$ compared to standard numerical integration with relative errors of $10^{-16}$ for the approximation methods LM, DEA, WNM, and QSA.

Figures 4.5 (d) (e) and (f) plot the relative error of the DEA model's approximations for $z$, $\langle M_x \rangle$, and $\langle \varepsilon^m_{xx} \rangle$. Figure 4.5 (d) has three trends of note. The first is that when $\mathrm{x} \gg 1$ a subset of values has a convergence rate of $\Theta(1/\mathrm{x})$ as $\mathrm{x} \to \infty$. This trend line supports the author's assertion that the DEA model is a simplified version of LM. The second trend is that like LM the DEA approximation has inaccurate approximations when x is on the order of 1 or smaller. The final trend is that a significantly large error can also occur when $\mathrm{x} \gg 1$. The authors attribute the significant error to two points, 1) utilization of inaccurate quadrature points / extrema and 2) the lack of the LM weight function. Finally, the same error cancellation that was seen in LM is shown for both the magnetization $\langle M_x \rangle$ and magnetostriction $\langle \varepsilon^m_{xx} \rangle$, capping the maximum error slightly above 100%.

Figures 4.5 (g) (h) and (i) plot the relative error of the WNM method's approximations for $z$, $\langle M_x \rangle$, and $\langle \varepsilon^m_{xx} \rangle$. The partition function $z$ plot in Figure 4.5 (g) shows the same convergence of $\Theta(1/\mathrm{x}^{1.5}))$ as $\mathrm{x} \to \infty$ as was shown by LM in Figure 4.5 (a) when $\mathrm{x} \ll 1$. Note that unlike LM the error has a convergence bounded by $\mathcal{O}(\mathrm{x})$ and $\Omega(\mathrm{x}^{1.875})$ as $\mathrm{x} \to 0$. This improved accuracy in the low energy regions can also be seen in the magnetization and magnetostriction plots, Figures 4.5 (h) and (i) respectively, with an upper bound on the convergence of $\mathcal{O}(\mathrm{x})$ as $\mathrm{x} \to 0$. Note that the error in the magnetization and magnetostriction plots when $\mathrm{x} \gg 1$ has more spread than LM, with a bounded convergence of $\mathcal{O}(1/\mathrm{x})$ and $\Omega(1/\mathrm{x}^{2.0})$ as $\mathrm{x} \to \infty$. The improved accuracy when $\mathrm{x} \ll 1$ and the spread shown when $\mathrm{x} \gg 1$ can both be attributed to the updated weights used in WNM. Finally, note that none of the maximum errors of the WNM method reach 100%.

Figures 4.5 (j) (k) and (l) plot the relative error of the QSA method's approximations for $z$, $\langle M_x \rangle$, and $\langle \varepsilon^m_{xx} \rangle$. The partition function $z$ plot in Figure 4.5 (j) shows convergence rates of $\Theta(\mathrm{x})$ as $\mathrm{x} \to 0$ and $\Theta(1/\mathrm{x}^{0.5})$ as $\mathrm{x} \to \infty$. While these convergence rates are more gradual than the WNM, note that the maximum error has decreased from $10^{-0.7}$ to $10^{-2}$. When $\mathrm{x} \ll 1$

both the magnetization and magnetostriction plots, Figures 4.5 (k) and (l) respectively, with an upper bound on the convergence of $\mathcal{O}(\mathrm{x}^{1.1})$ as $\mathrm{x} \to 0$. The magnetization plot has a lower bound of $\Omega(1/\mathrm{x}^{1.5})$ and an upper bound of $\mathcal{O}(1)$ as $\mathrm{x} \to \infty$. Of note, this upper bound that shows a constant convergence occurs when the expected value of magnetization is nearly zero. The magnetostriction plot has a lower bound of $\Omega(1/\mathrm{x}^{1.5})$ and an upper bound of $\mathcal{O}(1/\mathrm{x}^{0.5})$ as $\mathrm{x} \to \infty$. The same constant convergence shown in magnetization does not appear as the $\langle \varepsilon_{xx}^{m} \rangle$ value of magnetostriction is never zero. Finally, both the magnetization and magnetostriction approximations of the QSA method have a maximum error of $10^{-2.0}$.

The results shown in Figure 4.5 can all be understood in reference to the Boltzmann factors shown in Figure 4.1. For the solid black line when $|\min_{\Gamma} g_L| \gg 1$ the discrete methods (i.e., LM, DEA, and WNM) have accurate approximations as their chosen PDFs are or can be sharp peaks. Once again, this accuracy is dependent on properly identifying the minima of the microscale free energy. For the dash-dotted orange line shown in Figure 4.1, when $|\min_{\Gamma} g_L| \ll 1$, the Boltzmann factor resembles a trigonometric function and so it was only accurately approximated by periodic methods (WNM and QSA). Finally, the blue dotted line when $|\min_{\Gamma} g_L| \approx 1$ is the most complex Boltzmann factor and is the most difficult for the discrete methods to approximate as it does not resemble a standard PDF or trigonometric function. By removing the dependence on PDFs, the QSA method can better approximate the more complex region. Of note the accuracy of the QSA method can be increased by improving Algorithm 1. Even so, this basic version of the QSA was able to achieve the lowest maximum error of all the studied methods.

Figure 4.6 shows a histogram of the runtimes of each approximation method and standard numerical integration after the quadrature points or knots have been found. The DEA model has the fastest average runtime less than 0.1 ms, followed by LM at slightly less than 1 ms, and the WNM, at 1 ms. This trend is expected as the number of computations needed in

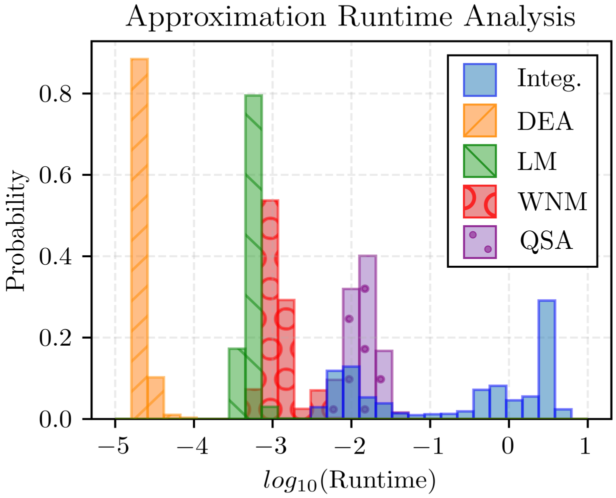

Figure 4.6: Histogram of the approximation runtime for the DEA, LM, WNM, QSA methods, and standard numerical integration.

each of these models grows, with LM having more complex weights than the DEA model, and the WNM updating the even more complex weights for overlapping peaks. The QSA method takes 10 ms to run, while the standard numerical integration of the initial problem can take anywhere from 10 ms to 5s (which is heavily dependent on the target accuracy). While the QSA method still relies on numerical integration by approximating the microscale free energy with quadratic splines the average runtime is several orders of magnitude faster than the slowest runtimes of the initial problem.

### 4.4.3 Effects of Numerical Accuracy on Predictions

For a numerical approximation to provide a valid constitutive model, it must not violate any of the relationships and established by classical thermodynamics. For example, the slope of the predicted magnetization and the predicted magnetic susceptibility should be consistent. Additionally, the choice of independent variables (i.e. stress and strain) should not artificially influence the material's response. The following section analyzes how the numerical error of the methods could violate these key thermodynamic relationships. As the DEA model is currently in use in the literature the focus will be on its predictions.

Figure 4.7 shows that the DEA model: 1) predicts thermodynamic inconsistencies, 2) has predictions influenced by the choice of independent variables, and 3) the response function and nonlinear material property predictions are inconsistent (e.g., $\langle \boldsymbol{\chi} \rangle_{DEA} \neq \mu_0^{-1} \partial \langle \boldsymbol{M} \rangle_{DEA} / \partial \boldsymbol{H}$). Figure 4.7(a) plots an M-H curve under a load of $T_{xx} = 12$ MPa, with all other stress components zero.

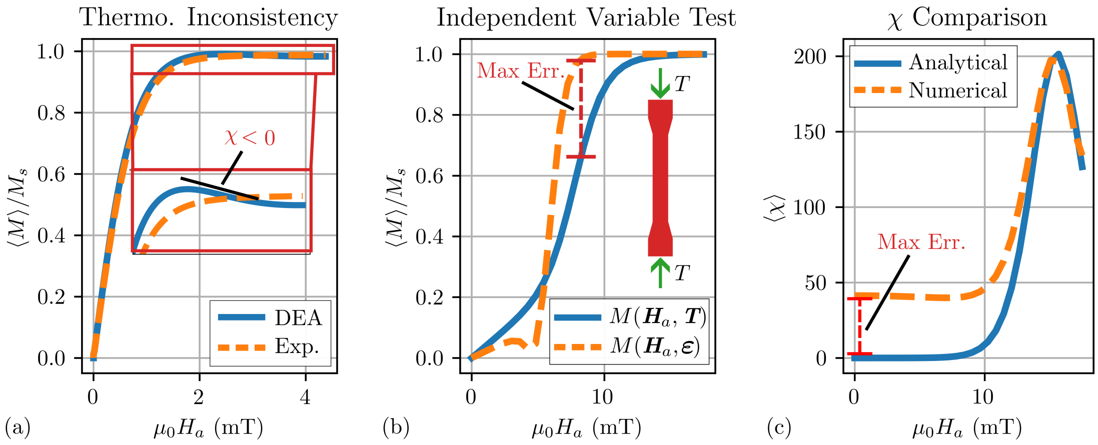

Figure 4.7: Analysis of DEA model: (a) An MH curve predicted by the DEA model after being curve fit to $Fe_{81.6}Ga_{18.4}$ [60]. Inset graph highlights an artificial thermodynamic inconsistency numerically created by the DEA model. (b) MH curves under constant axial load predicted by the DEA model using two different independent variables (stress or strain). In both cases, the sample is subjected to the same magnetic field and mechanical loads, but the predicted magnetization is clearly different. (c) Magnetic susceptibility approximated by the DEA model $\langle \boldsymbol{\chi} \rangle_{DEA}$ compared to that predicted by a numerical derivative $\langle \tilde{\boldsymbol{\chi}} \rangle_{num}$.

predicted by the DEA model, with material properties determined by curve fitting to experimental data for $Fe_{81.6}Ga_{18.4}$ [60]. The relative error of the fit (L2 norm) was 2.13% and the specific property values of the fit can be found in Table 4.2. While the fit shown in Figure 4.7(a) is generally good, the inset graph shows that the magnetic susceptibility becomes negative as the material approaches saturation. This is a thermodynamic inconsistency, as negative susceptibilities correspond to unstable systems. While negative susceptibilities may occur (e.g., after a ferromagnetic to diamagnetic phase change) [73, 90, 101, 140], this one is artificially generated by the inaccuracy of the DEA quadrature method. In the negative susceptibility regions, the DEA quadrature points sporadically hit and miss close to the actual extrema of $b(\boldsymbol{m})$, which leads to large numerical fluctuations. Although the severity of this inconsistency may appear small, in an alternate study the authors have found that it can cause faults that prevent nonlinear FEA simulations from converging.

Figure 4.7(b) plots a pair of M-H curves predicted by the DEA model. Both lines simulate the MH response of a material subjected to a constant uniaxial compressive stress. The 'stress control' line uses the exact equations from Wahi *et al.* [169]. The 'strain control' line performs a Legendre transform on the microscale free energy to convert from using stress to strain as the independent variable [99]. After the transform, the DEA procedure described in Wahi was used to construct a DEA model with strain as the independent variable. Both simulations were run with the same magnetic fields and same mechanical loads ($T_{xx} = -32$ MPa, with all other stress components zero.). For the strain control model, this required solving for the strain state consistent with the desired stress state. Figure 4.7(b) shows that changing the independent variable of the DEA model changes its predictions. The authors view this as a foundational concern, as the predictions of valid physical theories should be independent of the choice of independent variables.

Finally, Figure 4.7(c) plots the magnetic susceptibility predicted by $\langle \tilde{\boldsymbol{\chi}} \rangle_{DEA}$ shown in Equation (4.39), and compares it to $\langle \tilde{\boldsymbol{\chi}} \rangle_{num}$ calculated from a numerical derivative of $\langle \boldsymbol{M} \rangle_{DEA}$ (Equation (4.31)). As a reminder, the average DEA operator in Equation (4.32) is consistent with the equations presented in the literature [67, 68, 127, 160, 169]. The numerical $\langle \boldsymbol{\chi} \rangle_{num}$

was calculated with a finite difference derivative.

$$\langle \tilde{\boldsymbol{\chi}} \rangle_{DEA} = \frac{\mu_0}{\Omega} \left( \frac{\sum_{k=1}^{N} M_s^2 \boldsymbol{m}_k \otimes \boldsymbol{m}_k \exp(-g_L(\boldsymbol{m}_k)/\Omega)}{\sum_{k=1}^{N} \exp(-g_L(\boldsymbol{m}_k)/\Omega)} \right. \\ \left. - \left\langle \tilde{\boldsymbol{M}} \right\rangle_{DEA} \otimes \left\langle \tilde{\boldsymbol{M}} \right\rangle_{DEA} \right) \tag{4.39}$$

$$\langle \tilde{\chi}_{ij} \rangle_{num} = \frac{\left\langle \tilde{\boldsymbol{M}}_i(\boldsymbol{H}_a + \Delta H_a \hat{e}_j) \right\rangle_{DEA} - \left\langle \tilde{\boldsymbol{M}}_i(\boldsymbol{H}_a) \right\rangle_{DEA}}{\Delta H_a} \tag{4.40}$$

A parametric sweep was performed on $\Delta H$ to ensure the finite differences converged. Figure 4.7(c) shows a large difference between these two calculations of $\chi$. This again highlights that the DEA model does not accurately approximate the requisite integral equations of statistical mechanics. The importance of this observation can be briefly explained by considering how a nonlinear magnetostrictive constitutive model is utilized within an FEA routine. In that scenario one needs to calculate both the response functions $\langle \boldsymbol{M} \rangle$, $\langle \boldsymbol{\varepsilon}^m \rangle$ and the material jacobian (e.g., the linearized material properties $\langle \boldsymbol{\chi} \rangle$,$\langle \boldsymbol{q} \rangle$, $\langle \boldsymbol{S}^m \rangle$) in order to calculate a Newton update / linear perturbation. Based on the results in Figure 4.7(c), when using the DEA model this requires the use of numerical derivatives for the linear perturbations to be accurate. To fully populate the magnetic susceptibility, piezomagnetic coupling, and magnetic stiffness tensor the constitutive model must be called a total of 10 times. This increases the runtime of a single step in a FEA simulation by an order of magnitude. Alternatively, an accurate numerical approximation of the requisite integral equations would only need to be called twice.

Figure 4.7 demonstrates the importance of calculating numerically accurate approximations. Unless a certain level of numerical accuracy can be maintained spurious artifacts can be introduced into the model's predictions. Figures 4.8 (a) and (b) plot the magnetization and

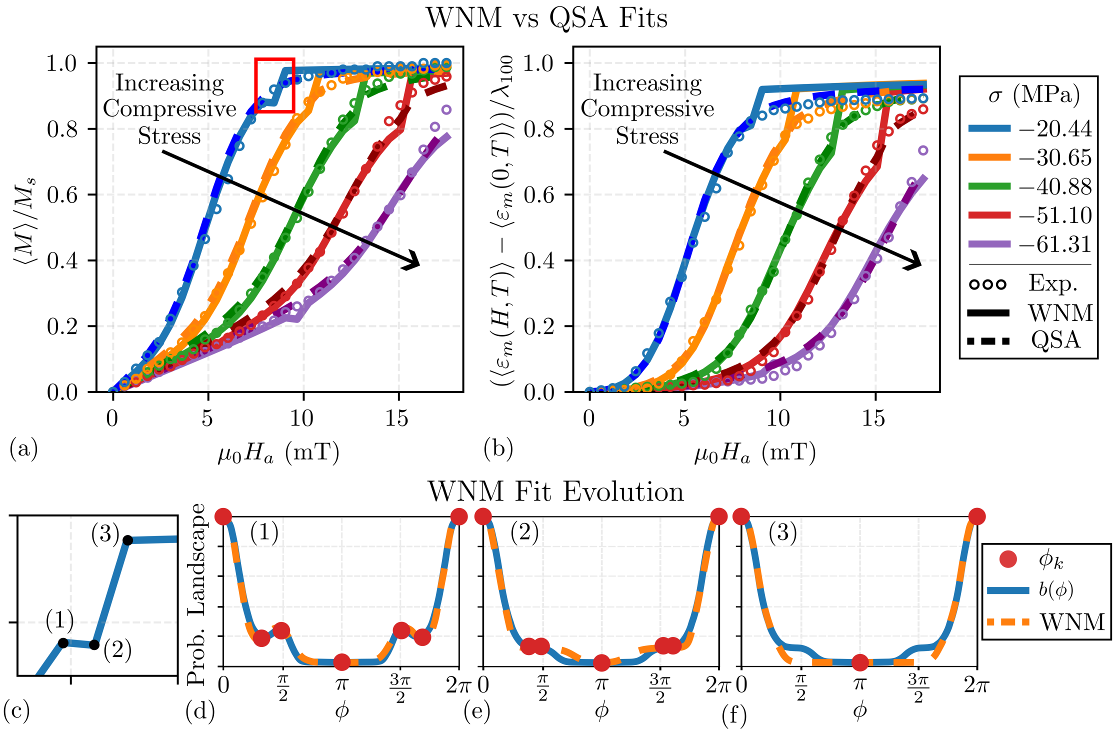

Figure 4.8: WNM and QSA predictions of (a) magnetization and (b) magnetostriction curves, curve fit to $Fe_{81.6}Ga_{18.4}$ [60]. (c) Comparison of 3 WNM partition function fits surrounding a thermodynamic consistency labeled in (a).

magnetostriction curves of $Fe_{81.6}Ga_{18.4}$ digitized from the literature with dotted lines [60]. Additionally, the predictions of the WNM model and the QSA model fit to the experimental data were plotted with solid and dashed lines respectively. Figures 4.8(a) and (b) both show that the WNM model breaks as the material approaches saturation (i.e., it incorrectly predicts negative susceptibilities). Figure 4.8 (c) shows a zoomed in view of the troublesome region, with three points around the negative susceptibility highlighted. Figures 4.8 (d)-(f) plot the Boltzmann factor $b(\phi)$ at each of these three points, the locations of energy extrema, and the approximate integrand / Boltzmann factor constructed by WNM with those extrema. Note that progressing from Figure 4.8 (d) to (f) (i.e., points 1 to 3) the extrema near $\pm\pi/2$ evolve by 1) starting as min/max pairs, then 2) merging into saddle points, before 3) annihilating and leaving the system with 4 fewer extrema. Trying to approximate the integrand with LM or WNM becomes very challenging with just the 2 remaining extrema. Of note, the thermodynamic inconsistency produced by this does not occur in the DEA model as it uses a constant number of quadrature points. This allows MH curves predicted by the DEA model to vary smoothly through the entire magnetization process. Similarly, Figures 4.8(a) and (b) show that the QSA approximation varies smoothly through the entire magnetization process. This can be attributed to the $\pm\{n\}\sigma_i$ knots scattered around the energy minima (described in Algorithm 1). As the QSA method can guarantee a consistent level of numerical accuracy that does not introduce any artificial spurious responses it will be used to simulate experimental data in the following section.

### 4.4.4 Experimental Comparison

This section compares the ability of the DEA and QSA models to simulate experimental data. It is worth noting that based on the accuracy results just presented, QSA most accurately solves the integral equations of statistical mechanics, while DEA had the largest errors. The DEA and QSA models were fit to the magnetization and magnetostriction curves for two compositions of Iron Gallium were digitized from the literature (see references in Table 4.2). The saturation magnetization $M_s$ was directly obtained from the data. The remaining material properties $\lambda_{100}$, $K_1$, and $\beta$ were obtained by minimizing the relative error between the models and the experimental data. Table 4.2 lists the average relative error between the models and the experimental data, and the material properties used to find them.

Table 4.2 shows that the DEA model more accurately simulates the experimental data for both of the tested materials, compared to the QSA model. It is worth noting that while both models have comparable relative errors the minimized properties that they use are different. The authors found that the QSA properties were nearly identical to those that would be found using standard numerical integration. This once again highlights that the DEA model

Table 4.2: Optimized parameters of QSA and DEA models

| $\text{Ga}_x$ | Model | $M_s$ | $\lambda_{100}$ | $K_1$ | $\beta$ | Error | Ref. |
|---|---|---|---|---|---|---|---|
| 18.4 | QSA | 126 | $176 \times 10^{-6}$ | 10.1 | $1.03 \times 10^{-3}$ | 2.70 | [60] |
| | DEA | | $156 \times 10^{-6}$ | 9.95 | $1.04 \times 10^{-3}$ | 2.13 | |
| 20.9 | QSA | 117 | $161 \times 10^{-6}$ | -1.49 | $1.27 \times 10^{-3}$ | 5.17 | [115] |
| | DEA | | $132 \times 10^{-6}$ | 117 | $0.56 \times 10^{-3}$ | 3.45 | |

*Units: $M_s$ (kA/M), $\lambda_{100}$ (-), $K$ (kJ/m$^3$), $\beta$ (m$^3$/J), Error (%)

is not accurately approximating the requisite integral equations. However, the fact that the DEA model achieves higher accuracy could suggest that the microscale free energy used in this work may not be complex enough to simulate the experimental data. As a reminder the presented model was limited to a thin film, is paramagnetic, and MFT was not used to approximate exchange energy.

## 4.5 Conclusion

This paper provides an analysis of several numerical approximation methods and shows how the numerical accuracy of the methods impacts the validity of the resulting magnetostrictive constitutive models. It was found that approximation methods built around approximating the Boltzmann factor $b(\phi)$ using PDFs (i.e., DEA, LM, and WNM) where computationally efficient but their numerical accuracy was highly dependent on finding the extrema of the microscale free energy density $g_L$. It was also found that the inaccurate numerical approximations of these methods resulted in degenerate / non-physical behaviors. Alternatively, the QSA method built around approximating $g_L$ was able to achieve a sufficient level of numerical accuracy that did not produce non-physical behaviors. Additionally, it was demonstrated that the QSA model was able to simulate two compositions of Iron Gallium with comparable fits to those of the DEA model.

# Chapter 5

# Non-equilibrium Thermodynamic Framework: Preliminary Study

## Attribution

This chapter, describes preliminary collaborative work with John P. Domann that has not yet been prepared for publication and so is not in manuscript form.

## 5.1 Introduction

Figure 5.1 shows the different responses that hysteretic dependence can produce. These include the major hysteresis loop, the largest loop in which the material saturates at both ends, and the much more complicated minor loops that can occur. A fully developed model of hysteresis should be able capture all of these responses.

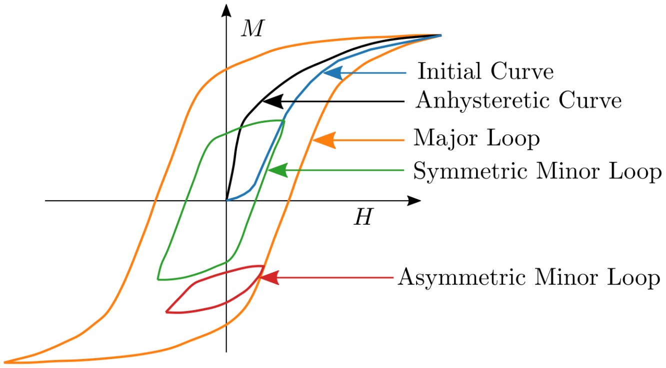

Figure 5.1: Possible Hysteresis Loops and Magnetization Curves

Chapter 2 briefly introduced the Jiles-Atherton model, which introduced hysteresis in terms of a first-order differential equation and decomposes magnetization into reversible and irreversible components. The three main postulates of the original JA model are,

$$\boldsymbol{M} = \boldsymbol{M}_{rev} + \boldsymbol{M}_{irr} \tag{5.1}$$

$$\boldsymbol{M}_{rev} = c(\boldsymbol{M}_{an} - \boldsymbol{M}) \tag{5.2}$$

$$\frac{d\boldsymbol{M}_{irr}}{d\boldsymbol{H}} = \frac{\boldsymbol{M}_{an} - \boldsymbol{M}_{irr}}{\delta k - \alpha(\boldsymbol{M}_{an} - \boldsymbol{M}_{irr})} \tag{5.3}$$

where $\alpha$ is inter-domain coupling approximation term from MFT while $c$ and $k$ are said to quantify magnetization reversibility and energy loss per unit magnetization respectively. Additionally, $\delta$ takes the value of ±1 depending on whether the applied field is increasing towards the positive or negative saturation values. The final differential equation of the JA model is,

$$\frac{d\boldsymbol{M}}{d\boldsymbol{H}} = \frac{1}{1+c}\frac{\boldsymbol{M}_{an}-\boldsymbol{M}}{\delta k-\alpha(\boldsymbol{M}_{an}-\boldsymbol{M})} + \frac{c}{1+c}\frac{d\boldsymbol{M}_{an}}{d\boldsymbol{H}}. \tag{5.4}$$

Note that this original presentation is the result of an algebra mistake and combing Equations (5.1) - (5.3) should produce,

$$\frac{d\boldsymbol{M}}{d\boldsymbol{H}} = \frac{\boldsymbol{M}_{an}-\boldsymbol{M}}{\delta k-\alpha(1+c)(\boldsymbol{M}_{an}-\boldsymbol{M})} + \frac{c}{1+c}\frac{d\boldsymbol{M}_{an}}{d\boldsymbol{H}}. \tag{5.5}$$

A significant limitation of the JA model is the inability to capture the effects of magnetostriction. Many models have attempted to include the effects of magnetostriction by using Langevin Magnetostriction as the anhysteretic magnetization, the limitations of which were discussed in previous Chapters [111, 128, 129, 146, 147, 148]. Furthermore, it was recognized that if $k$ is constant then the differential equations do not account for losses due to applied stresses [107]. For example, when $\boldsymbol{H} = 0$ the magnetization will also be equal to 0. Applying a stress to the material in this state will change the domain structure of the material which should result in losses due to domain wall motion. However, as the total magnetization is zero during this process, the JA model predicts zero energy loss. In summary there are numerous inconsistencies in the JA model from basic algebraic errors to thermodynamic issues. The proposed framework will be derived using rigorous thermodynamics to address these inconsistencies. However, as the JA model is widely used, its positive aspects will be used to guide the development of the dissipative constitutive laws.

As discussed in Chapter 2 another branch of hysteretic models have been inspired by modern approaches of kinematic hardening and plasticity theory. Notably, these models also separate the conjugate work variables into reversible and irreversible components using internal state variable formalism which again results in a system of differential equations that describe hysteresis. This reinforces the idea that the relations described in the JA model have merit and that by constructing a framework using rigorous thermodynamics ensures that inconsistencies like negative susceptibilities can be avoided. The derivation of this framework begins by specializing the non-equilibrium inequality from Chapter 2 to a magnetostrictive system.

## 5.2 Problem Definition

The non-equilibrium term imbalance is reproduced here:

$$\rho(\Theta\dot{\eta} - \dot{u}) + \mathbb{s} \cdot \dot{\mathbb{f}} - \boldsymbol{q} \cdot \frac{\nabla\Theta}{\Theta} = -\Theta\Gamma \leq 0 \tag{5.6}$$

For the proposed magnetostrictive system the total work is decomposed into magnetic and mechanical work. Equation (5.7) shows an expression for magnetic work containing the applied magnetic field $H_a$, which is a quantity of more direct physical interest than the total magnetic field $H$.

$$\dot{\boldsymbol{W}}_M = \mu_0 \boldsymbol{H}_a \cdot \dot{\boldsymbol{M}} \tag{5.7}$$

where $M$ is the magnetization. The heat flow of the system is described by the divergence of heat flux vector $\boldsymbol{q}$ and an internal heat source per unit mass $r$. The local form of the first law of thermodynamics can be expanded as

$$\rho\dot{u} = \mu_0 \boldsymbol{H}_a \cdot \dot{\boldsymbol{M}} + \boldsymbol{\sigma} : \dot{\boldsymbol{\varepsilon}} - \nabla \cdot \boldsymbol{q} + r. \tag{5.8}$$

Using the new definitions of work the free energy imbalance becomes:

$$\rho(\Theta\dot{\eta} - \dot{u}) + \mu_0 \boldsymbol{H}_a \cdot \dot{\boldsymbol{M}} + \boldsymbol{\sigma} : \dot{\boldsymbol{\varepsilon}} - \boldsymbol{q} \cdot \frac{\nabla\Theta}{\Theta} = -\Theta\Gamma \leq 0 \tag{5.9}$$

Non-equilibrium processes are dependent on irreversible forces and their conjugate irreversible fluxes, these terms are often commonly referred to as internal state variables. In this work applied magnetic field and stress are typically treated as the independent variables, and so both are separated into reversible and irreversible components,

$$\boldsymbol{H}_a = \boldsymbol{H}_a^{rev} + \boldsymbol{H}_a^{irr},\ \boldsymbol{\sigma} = \boldsymbol{\sigma}^{rev} + \boldsymbol{\sigma}^{irr}. \tag{5.10}$$

Additionally, a Legendre transform is applied to the free energy imbalance so that it is now dependent on the Gibbs Free energy density $g(\boldsymbol{H}_a, \boldsymbol{\sigma})$,

$$\rho(\dot{\Theta}\eta + \dot{g}) + \mu_0 \boldsymbol{M} \cdot \dot{\boldsymbol{H}}_a + \boldsymbol{\varepsilon} : \dot{\boldsymbol{\sigma}} - \boldsymbol{q} \cdot \frac{\nabla\Theta}{\Theta} = -\Theta\Gamma \leq 0. \tag{5.11}$$

Substituting Equation (5.10) into Equation (5.11) produces

$$\begin{aligned}(\mu_0 \boldsymbol{M} + \rho\frac{\partial g}{\partial \boldsymbol{H}_a}) \cdot \dot{\boldsymbol{H}}_a + \rho\frac{\partial g}{\partial \boldsymbol{H}_a^{irr}} \cdot \dot{\boldsymbol{H}}_a^{irr} + (\boldsymbol{\varepsilon} + \rho\frac{\partial g}{\partial \boldsymbol{\sigma}}) : \dot{\boldsymbol{\sigma}} \\ + \rho\frac{\partial g}{\partial \boldsymbol{\sigma}^{irr}} : \dot{\boldsymbol{\sigma}}^{irr} + \rho(\eta + \frac{\partial g}{\partial \Theta}) \cdot \dot{\Theta} = -\Theta\Gamma \leq 0\end{aligned} \tag{5.12}$$

Note that as the terms inside of the parentheses must be equal to zero the classical thermodynamic relationships are reproduced,

$$\boldsymbol{M} = -\frac{\rho}{\mu_0}\frac{\partial g}{\partial \boldsymbol{H}_a},\ \boldsymbol{\varepsilon} = -\rho\frac{\partial g}{\partial \boldsymbol{\sigma}},\ \eta = -\rho\frac{\partial g}{\partial \Theta}. \tag{5.13}$$

Furthermore, Equation (5.12) is reduced such that it only contains the irreversible terms:

$$\rho \left( \frac{\partial g}{\partial \boldsymbol{H}_a^{irr}} \cdot \dot{\boldsymbol{H}}_a^{irr} + \frac{\partial g}{\partial \boldsymbol{\sigma}^{irr}} : \dot{\boldsymbol{\sigma}}^{irr} \right) = -\Theta\Gamma \leq 0 \tag{5.14}$$

Thus far the model has been constructed to ensure that the evolution process obeys the second law of thermodynamics in the form of the Clausius-Duhem inequality. However an additional constraint is required to determine which evolution process is actually taken between equilibrium states.

## 5.3 Defining Constitutive Relationships

The constitutive relationship of dissipative material response is evolution equations for the internal state variables. Determining these evolution equations are determined by introducing a dissipation function,

$$\mathcal{D} = \Theta\Gamma \tag{5.15}$$

$$\mathcal{D} \geq 0 \tag{5.16}$$

The dissipation function is a pseudo-potential analogous to the thermodynamic potentials that relates the irreversible work terms to the internal variables of the system. From the second law of thermodynamics, the dissipation must remain non-negative. Convex analysis provides a way to ensure that the chosen definition of the dissipation does not violate the second law. The simplest dissipation potential (a quadratic one) was developed by Onsager [135] that results in a linear kinetic evolution equations. Onsager's work was extended to material modeling by Ziegler which allows for nonlinear dissipation [191, 192, 193, 194].

The dissipation function is related to the yield function through a Legendre transform. The yield function is commonly used in plasticity theory to determine when the deformation of a material switches from elastic to plastic. This switching criterion determines when the dissipation of the system is zero. Finally, the differential of the yield function defines the flow rule of the internal variables. In plasticity theory the flow rules define how a material deforms plastically when subjected to stress beyond its yield surface.

Different modeling approaches focus on defining a single one of these related functions to try and simulate the desired response. While starting from a physically consistent dissipation potential guarantees that the second law is not violated, it is not immediately obvious what flow rule is associated with that potential. On the other hand starting from a flow rule that qualitatively produces the desired dissipation response, it's dissipation potential may not always be valid.

## 5.4 Preliminary Results

To quickly test the validity of the framework and derivation above this formalism was applied to the case of a purely magnetic material. The next intention was to define a flow rule that mimicked the base differential equations of the JA model.

To derive a flow rule for the internal variable $\boldsymbol{H}_a^{irr}$ assume that $\boldsymbol{M}$, $\boldsymbol{H}_a$, $\dot{\boldsymbol{M}}$, and $\dot{\boldsymbol{H}}_a$ have been measured, which implies that $\boldsymbol{\chi} = dM/dH$ has also been measured. Note that by choosing to separate the applied magnetic field into reversible and irreversible parts the final model of magnetization can be presented as $\hat{\boldsymbol{M}}(\boldsymbol{H}_a - \boldsymbol{H}_a^{irr})$ where, $\hat{\boldsymbol{M}}(\boldsymbol{H}_a)$ is an anhysteretic model. Of note had magnetization been chosen as the variable being separated into reversible and irreversible parts the constitutive model would have the form of $\hat{\boldsymbol{H}}(\boldsymbol{M} - \boldsymbol{M}^{irr})$ instead.

Using this final version of the constitutive model,

$$\boldsymbol{\chi} = \frac{d\boldsymbol{M}}{d\boldsymbol{H}_a} = \frac{d\hat{\boldsymbol{M}}}{d(\boldsymbol{H}_a - \boldsymbol{H}_a^{irr})} \left( \frac{d\boldsymbol{H}_a}{d\boldsymbol{H}_a} - \frac{d\boldsymbol{H}_a^{irr}}{d\boldsymbol{H}_a} \right) = \hat{\boldsymbol{\chi}}(\boldsymbol{H}_a - \boldsymbol{H}_a^{irr}) \left( \mathbb{1} - \frac{d\boldsymbol{H}_a^{irr}}{d\boldsymbol{H}_a} \right) \tag{5.17}$$

To solve for the evolution of the internal variable first,

$$\frac{d\boldsymbol{H}_a^{irr}}{d\boldsymbol{H}_a} = (\mathbb{1} - \chi_{H-h}^{-1}\chi) \tag{5.18}$$

and so

$$\dot{\boldsymbol{H}}_a^{irr} = (\mathbb{1} - \boldsymbol{\chi}_{\boldsymbol{H}_a - \boldsymbol{H}_a^{irr}}^{-1}\boldsymbol{\chi})\dot{\boldsymbol{H}}_a \tag{5.19}$$

To define this system $\boldsymbol{\chi}$ needs to be solved for. As this work is trying to simulate the JA model, $\boldsymbol{\chi} \to \boldsymbol{\chi}_{JA}$. Now, it is possible to solve the ordinary differential equation for $\boldsymbol{H}_a^{irr}$ which can then be plugged into the Langevin equation. This choice was made so that the non-equilibrium framework can be tested to see if it qualitatively produces the same hysteretic behavior as the Jiles-Atherton model. Of note the Mean Field term in in the JA model was ignored because it can independently introduce hysteresis (i.e., $\alpha = 0$). Figure 5.2 plots the anhysteretic (Langevin) curve, the original Jiles-Atherton model, and the anhysteretic model with the irreversible magnetic field calculated using the ISV theory. Figure 5.2 shows that in this formalism the same qualitative hysteresis loop can still be predicted now with the guarantee that the second law of thermodynamics will not be violated.

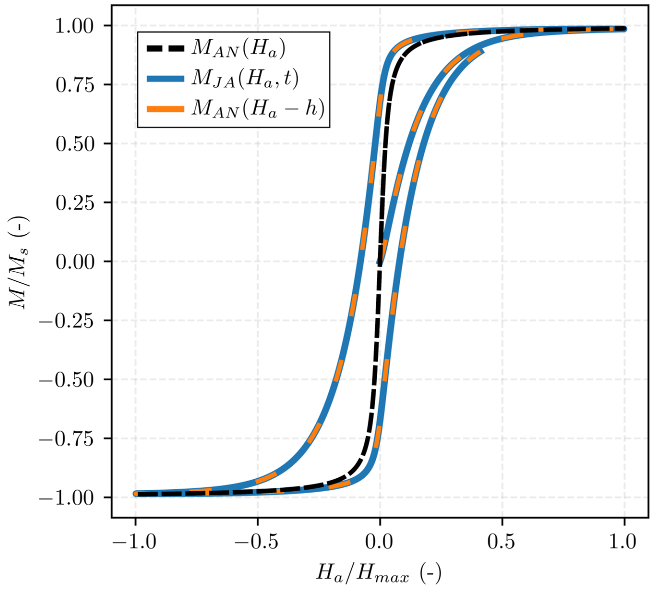

Figure 5.2: A comparison of the Jiles-Atherton model to an ISV hysteretic model inspired by the JA model

## 5.5 Summary

One of the major takeaways of this framework is that the entire constitutive framework can be derived once both a thermodynamic potential (Landau free energy) and the pseudo-potential (Dissipation) are defined. Figure 5.2 shows that this non-equilibrium framework allows for the inclusion of unambiguous dissipation potentials and so there are several avenues of further study that would be required to bring this work to a significant advancement in the field.

First, instead of choosing the Langevin function as the anhysteretic function using either of the models defined in Chapters 3 and 4 would produce a magnetostrictive hysteretic model. Second, the existing flow rules in the rest of the literature as well as plasticity theory itself which have various different forms need to be analyzed. In doing so the author would intend to determine if there are any properties that a new flow rule must exhibit, if the general

JA differential equations satisfy the required features of a flow rule, and thoroughly analyze how this flow rule influences the models predictions.

Another point to be addressed is that magnetic hysteresis models typically model the sources of loss separately as they occur at different size and time scales. It would be useful to translate rate-dependent plasticity models as a method of simulating anomalous eddy current loss.

# Chapter 6

# Conclusions

## 6.1 Summary

This dissertation provided and overview of the requirements and considerations of a framework for a unified model of macroscale magnetostriction. Starting from a rigorous thermodynamic derivation it was proposed that a magnetostrictive material can be fully defined by choosing a thermodynamic potential and a dissipative pseudo-potential. Utilizing this framework would allow one to easily compare the individual assumptions of existing models and test their range of validity. The chapters explored possible definitions of these potentials and what would be needed to accurately and efficiently solve them for high fidelity simulations.

Chapter 3 provided an analytical one-dimensional constitutive model for magnetostriction. Closed form analytical solutions were provided to calculate the average magnetization, magnetostriction, susceptibility, compliance, and piezomagnetic coupling coefficient. Additionally, it was demonstrated that the analytical model maintains numerical accuracy over a large range of applied magnetic fields and stress / anisotropy conditions. Finally, the model was used to simulate experimental data for three different materials. This comparison only required fitting two model parameters to the data. Comparisons between the experimental and modeled results indicate that the model is capable of simulating Terfenol-D and is expected to also accurately describe certain cubic materials as long as they have probability landscapes that are well approximated as transversely isotropic.

Chapter 4 provided an analysis of several numerical approximation methods and shows how the numerical accuracy of the methods impacts the validity of the resulting magnetostrictive constitutive models. It was found that approximation methods built around approximating the Boltzmann factor $b(\phi)$ using PDFs (i.e., DEA, LM, and WNM) where computationally efficient but their numerical accuracy was highly dependent on finding the extrema of the microscale free energy density $g_L$. It was also found that the inaccurate numerical approximations of these methods resulted in degenerate / non-physical behaviors. Alternatively, the QSA method built around approximating $g_L$ was able to achieve a sufficient level of numerical accuracy that did not produce non-physical behaviors. Additionally, it was demonstrated that the QSA model was able to simulate two compositions of Iron Gallium with comparable fits to those of the DEA model.

Finally, Chapter 5 presented the non-equilibrium thermodynamic framework necessary to introduce hysteresis to the anhysteretic magnetostrictive models in Chapters 3 and 4. This was followed by a brief discussion on the terms that define the dissipative constitutive laws. This chapter ended with a qualitative comparison of this an ISV hysteretic model to the original JA model and it was found that they were essentially identical.

## 6.2 Future Work

While this dissertation advances the state of magnetostrictive modeling in several directions, it also raises many different questions that require further study. The main questions come from Chapters 4 and 5. Chapter 4 established that a sufficiently accurate numerical approximation of the requisite integral equations is necessary to ensure thermodynamic consistency. Further work should investigate computational implementations of the Error function and the Dawson function. While Chapter 3 showed that a one dimensional model could produce numerically accurate solutions, the two dimensional model required that these special functions evaluate complex arguments. The implementations used by the authors could not maintain numerical accuracy and so the runtime of the quadratic spline approach was hindered. Proper solutions could potentially increase the runtime of this approach and make it competitive with the DEA model without sacrificing its accuracy. Furthermore, the quadrature methods that the author explored could not maintain a physically relevant solution even as their numerical accuracy improved. To areas of study could focus on other approximation methods, or ways to reduce the complexity of the proposed approximation methods to improve their physical predictions.

As chapter 5 only contained preliminary work the areas for future work are extensive. A full review of the existing hysteretic plasticity-inspired models should be performed to gain a qualitative understanding of different dissipation potentials and their associated flow rules. As hysteretic losses are often separated into three different size and time scales the author expects that multiple different internal variables will be needed to capture all of the potential hysteretic responses. Existing plasticity models may have already defined dissipation potentials applicable to this problem that have yet to be transplanted to a magnetic system. Finally, the base anhysteretic model used in this framework should be magnetostrictive. Either of the models presented in Chapters 3 and 4 could be used but the authors suspect that an additional dissipation term solely dependent on irreversible mechanics will be needed to fully define the system.

# Bibliography

[1] Burden of Musculoskeletal Diseases in the United States (BMUS). Technical report, 2014.

[2] Sanjar M. Abrarov and Brendan M. Quine. Accurate approximations for the complex error function with small imaginary argument. *Journal of Mathematics Research*, 7 (1):p44, January 2015. ISSN 1916-9809, 1916-9795. doi: 10.5539/jmr.v1n1p44.

[3] Sanjar M. Abrarov and Brendan M. Quine. A rational approximation of the Dawson's integral for efficient computation of the complex error function. *Applied Mathematics and Computation*, 321:526–543, March 2018. ISSN 0096-3003. doi: 10.1016/j.amc.2017.10.032.

[4] Amr A. Adly, Isaak D. Mayergoyz, and Anders J. Bergqvist. Preisach modeling of magnetostrictive hysteresis. *Journal of Applied Physics*, 69(8):5777–5779, April 1991. ISSN 0021-8979. doi: 10.1063/1.347873.

[5] Mohammad Al Janaideh, Subhash Rakheja, and Chun-Yi Su. An Analytical Generalized Prandtl–Ishlinskii Model Inversion for Hysteresis Compensation in Micropositioning Control. *IEEE/ASME Transactions on Mechatronics*, 16(4):734–744, August 2011. ISSN 1941-014X. doi: 10.1109/TMECH.2010.2052366.

[6] Anibal Almeida, Manuel Martinez, Angelo Baggini, and Hans De Keulenaer. Energy PROPHET II: The potential for global energy savings from high-efficiency distribution transformers. Technical report, Novermber 2014.

[7] Maria Antónia Amaral Turkman, Carlos Daniel Paulino, and Peter Müller. *Compu-*

*tational Bayesian Statistics: An Introduction.* Institute of Mathematical Statistics Textbooks. Cambridge University Press, Cambridge, 2019. ISBN 978-1-108-48103-8. doi: 10.1017/9781108646185.

[8] William D. Armstrong. Magnetization and magnetostriction processes in Tb(0.27-0.30)Dy(0.73-0.70)Fe(1.9-2.0). *Journal of Applied Physics*, 81(5):2321–2326, March 1997. ISSN 0021-8979, 1089-7550. doi: 10.1063/1.364235.

[9] William D. Armstrong. A directional magnetization potential based model of magnetoelastic hysteresis. *Journal of Applied Physics*, 91(4):2202–2210, February 2002. ISSN 0021-8979, 1089-7550. doi: 10.1063/1.1431433.

[10] William D. Armstrong. Fully three-dimensional incremental model of magneto-elastic hysteresis in Terfenol-D. In Dimitris C. Lagoudas, editor, *Smart Structures and Materials*, page 405, San Diego, CA, August 2003. doi: 10.1117/12.484698.

[11] Tadashi Ataka, Atsushi Furuya, Yuji Uehara, Koichi Shimizu, Jun Fujisaki, Tomohiro Tanaka, and Hirotaka Oshima. Accelerating Algorithm of Micromagnetic Simulation by Interpolating Magnetization Vectors. *IEEE Transactions on Magnetics*, 51(11):1–4, November 2015. ISSN 1941-0069. doi: 10.1109/TMAG.2015.2436411.

[12] Jayasimha Atulasimha. *Characterization and Modeling of the Magnetomechanical Behavior of Iron-Gallium Alloys.* PhD thesis, University of Maryland, August 2006.

[13] Jayasimha Atulasimha and Alison B. Flatau. A Review of Magnetostrictive Iron–Gallium Alloys. *Smart Materials and Structures*, 20:043001, March 2011. doi: 10.1088/0964-1726/20/4/043001.

[14] Jayasimha Atulasimha, Alison B. Flatau, and Eric Summers. Characterization and energy-based model of the magnetomechanical behavior of polycrystalline iron–gallium

alloys. *Smart Materials and Structures*, 16(4):1265–1276, August 2007. ISSN 0964-1726, 1361-665X. doi: 10.1088/0964-1726/16/4/039.

[15] Jayasimha Atulasimha, George Akhras, and Alison B. Flatau. Comprehensive three dimensional hysteretic magnetomechanical model and its validation with experimental $\langle 110 \rangle$ single-crystal iron-gallium behavior. *Journal of Applied Physics*, 103(7):07B336, April 2008. ISSN 0021-8979. doi: 10.1063/1.2839280.

[16] Jayasimha Atulasimha, Alison B. Flatau, and James R. Cullen. Energy-based quasi-static modeling of the actuation and sensing behavior of single-crystal iron-gallium alloys. *Journal of Applied Physics*, 103(1):014901, January 2008. ISSN 0021-8979. doi: 10.1063/1.2826946.

[17] Winfried Auzinger and Hans J. Stetter. An Elimination Algorithm for the Computation of All Zeros of a System of Multivariate Polynomial Equations. In Ch. Blanc, K.-H. Hoffmann, H. D. Mittelmann, J. Todd, Ravi P. Agarwal, Y. M. Chow, and S. J. Wilson, editors, *Numerical Mathematics Singapore 1988*, volume 86, pages 11–30. Birkhäuser Basel, Basel, 1988. ISBN 978-3-7643-2255-7 978-3-0348-6303-2. doi: 10.1007/978-3-0348-6303-2_2.

[18] Daichi Azuma and Ryusuke Hasegawa. Audible noise from amorphous metal and silicon steel-based transformer core. *IEEE Transactions on Magnetics*, 44(11 PART 2):4104–4106, 2008. doi: 10.1109/TMAG.2008.2003174.

[19] Anthony Barra, Ajit Mal, Greg P. Carman, and Angel E. Sepulveda. Voltage induced mechanical/spin wave propagation over long distances. *Applied Physics Letters*, 110 (7):072401, February 2017. ISSN 0003-6951, 1077-3118. doi: 10.1063/1.4975828.

[20] Kim Batselier. *A Numerical Linear Algebra Framework for Solving Problems with Multivariate Polynomials*. PhD thesis, Katholieke Universiteit Leuven, 2013.

[21] Kim Batselier, Philippe Dreesen, and Bart De Moor. On the null spaces of the Macaulay matrix. *Linear Algebra and its Applications*, 460:259–289, November 2014. ISSN 00243795. doi: 10.1016/j.laa.2014.07.035.

[22] James S. Bennett, Brian E. Vyhnalek, Hamish Greenall, Elizabeth M. Bridge, Fernando Gotardo, Stefan Forstner, Glen I. Harris, Félix A. Miranda, and Warwick P. Bowen. Precision Magnetometers for Aerospace Applications: A Review. *Sensors*, 21(16):5568, January 2021. ISSN 1424-8220. doi: 10.3390/s21165568.

[23] Anders J. Bergqvist, Andreas Lundgren, F. Stillesjö, and Göran Engdahl. Statistical modeling of magnetic and magnetostrictive properties due to domain wall motion. *Journal of Applied Physics*, 85(8):5190–5192, April 1999. ISSN 0021-8979, 1089-7550. doi: 10.1063/1.369120.

[24] Giorgio Bertotti. *Hysteresis in Magnetism: For Physicists, Materials Scientists, and Engineers.* Gulf Professional Publishing, Oxford, May 1998. ISBN 978-0-12-093270-2.

[25] Blair Bilodeau, Yanbo Tang, and Alex Stringer. On the Tightness of the Laplace Approximation for Statistical Inference. *Statistics & Probability Letters*, 198:109839, July 2023. ISSN 01677152. doi: 10.1016/j.spl.2023.109839.

[26] Oriano Bottauscio, Paolo Emilio Roccato, and Mauro Zucca. Micropositioning Through Magnetostrictive Actuators. *Sensor Letters*, 11(1):87–90, January 2013. doi: 10.1166/sl.2013.2820.

[27] John P. Boyd. Computing the zeros, maxima and inflection points of Chebyshev, Legendre and Fourier series: Solving transcendental equations by spectral interpolation and polynomial rootfinding. *Journal of Engineering Mathematics*, 56(3):203–219, January 2007. ISSN 0022-0833, 1573-2703. doi: 10.1007/s10665-006-9087-5.

[28] John P. Boyd. A Fourier Companion Matrix (Multiplication Matrix) with Real-Valued Elements: Finding the Roots of a Trigonometric Polynomial by Matrix Eigensolving. *Numerical Mathematics: Theory, Methods and Applications*, 6(4):586–599, June 2013. ISSN 1004-8979, 2079-7338. doi: 10.4208/nmtma.2013.1220nm.

[29] John P. Boyd. *Solving Transcendental Equations.* Other Titles in Applied Mathematics. Society for Industrial and Applied Mathematics, September 2014. ISBN 978-1-61197-351-8. doi: 10.1137/1.9781611973525.

[30] John P. Boyd and Burhan A. Sadiq. Computing the real roots of a Fourier series-plus-linear-polynomial: A Chebyshev companion matrix approach. *Applied Mathematics and Computation*, 219(3):819–826, October 2012. ISSN 0096-3003. doi: 10.1016/j.amc.2012.06.045.

[31] William Fuller Brown, Jr. Rigorous Approach to the Theory of Ferromagnetic Microstructure. *Journal of Applied Physics*, 29(3):470–471, March 1958. ISSN 0021-8979. doi: 10.1063/1.1723183.

[32] William Fuller Brown, Jr. Micromagnetics, Domains, and Resonance. *Journal of Applied Physics*, 30(4):S62–S69, April 1959. ISSN 0021-8979. doi: 10.1063/1.2185970.

[33] John L. Butler. *Application Manual for the Design of ETREMA Terfenol-D Magnetostrictive Transducers.* ETREMA Products, Inc., Ames, IA, 1988.

[34] Ronald W. Butler. *Saddlepoint Approximations with Applications.* Cambridge University Press, August 2007. ISBN 978-1-139-46651-6.

[35] Greg P. Carman and Milan Mitrovic. Nonlinear Constitutive Relations for Magnetostrictive Materials with Applications to 1-D Problems. *Journal of Intelligent Ma-*

*terial Systems and Structures*, 6(5):673–683, September 1995. ISSN 1045-389X. doi: 10.1177/1045389X9500600508.

[36] Kenneth H. Carpenter. A Differential Equation Approach to Minor Loops in the Jiles-Atherton Hysteresis Model. *IEEE Transactions on Magnetics*, 27(6):4404–4406, 1991. ISSN 0018-9464. doi: 10.1109/20.278655.

[37] Suryarghya Chakrabarti. *Modeling of 3D Magnetostrictive Systems with Application to Galfenol and Terfenol-D Transducers*. PhD thesis, The Ohio State University, 2011.

[38] Suryarghya Chakrabarti and Marcelo J. Dapino. Fully coupled discrete energy-averaged model for Terfenol-D. *Journal of Applied Physics*, 111(5):054505, March 2012. ISSN 0021-8979. doi: 10.1063/1.3687372.

[39] Yunshuai Chen, Pengyang Li, Jian Sun, and Guoqing Chen. Domain Switching-Based Nonlinear Coupling Response for Giant Magnetostrictive Materials. *Materials*, 16(14): 4914, July 2023. ISSN 1996-1944. doi: 10.3390/ma16144914.

[40] Peng Cheng and Roman Szewczyk. Modified Description of Magnetic Hysteresis in Jiles-Atherton Model. In Roman Szewczyk, Cezary Zieliński, and Małgorzata Kaliczyńska, editors, *Automation 2018*, volume 743, pages 648–654. Springer International Publishing, Cham, 2018. ISBN 978-3-319-77178-6 978-3-319-77179-3. doi: 10.1007/978-3-319-77179-3_62.

[41] Soshin Chikazumi. *Physics of Ferromagnetism*. International Series of Monographs on Physics. Oxford University Press, Oxford, New York, second edition edition, June 2009. ISBN 978-0-19-956481-1.

[42] Frank Claeyssen, Nicolas Lhermet, Ronan L. Le Letty, and Philippe Bouchilloux. Actuators, transducers and motors based on giant magnetostrictive materials. *Jour-*

*nal of Alloys and Compounds*, 258(1):61–73, August 1997. ISSN 0925-8388. doi: 10.1016/S0925-8388(97)00070-4.

[43] Arthur E. Clark, B. F. DeSavage, and Richard M. Bozorth. Anomalous Thermal Expansion and Magnetostriction of Single-Crystal Dysprosium. *Physical Review*, 138 (1A):A216–A224, April 1965. doi: 10.1103/PhysRev.138.A216.

[44] Arthur E. Clark, Raymond J. Abbundi, and W. Gillmor. Magnetization and magnetic anisotropy of TbFe2, DyFe2, Tb0.27Dy0.73Fe2and TmFe2. *IEEE Transactions on Magnetics*, 14(5):542–544, September 1978. ISSN 1941-0069. doi: 10.1109/TMAG.1978.1059879.

[45] Arthur E. Clark, James B. Restorff, Marilyn Wun-Fogle, and Thomas A. Lograsso. Magnetostrictive properties of Fe-Ga alloys under large compressive stresses. In *INTERMAG 2000 Digest of Technical Papers. 2000 IEEE International Magnetics Conference*, pages 177–177, Toronto, Canada, 2000. IEEE. ISBN 978-0-7803-5943-7. doi: 10.1109/INTMAG.2000.871955.

[46] Arthur E. Clark, Marilyn Wun-Fogle, James B. Restorff, Thomas A. Lograsso, and J.R. Cullen. Effect of quenching on the magnetostriction on Fe/sub 1-x/Ga/sub x/ (0.13x lt;0.21). *IEEE Transactions on Magnetics*, 37(4):2678–2680, July 2001. ISSN 1941-0069. doi: 10.1109/20.951272.

[47] Arthur E. Clark, Marilyn Wun-Fogle, James B. Restorff, and Thomas A. Lograsso. Magnetostrictive Properties of Galfenol Alloys Under Compressive Stress. *Materials Transactions*, 43(5):881–886, 2002. doi: 10.2320/matertrans.43.881.

[48] William J. Cody. Algorithm 715: SPECFUN–a portable FORTRAN package of special function routines and test drivers. *ACM Transactions on Mathematical Software*, 19 (1):22–30, March 1993. ISSN 0098-3500, 1557-7295. doi: 10.1145/151271.151273.

[49] John Michael David Coey. *Magnetism and Magnetic Materials*. Cambridge University Press, Cambridge, 2010. ISBN 978-0-521-81614-4. doi: 10.1017/CBO9780511845000.

[50] Bernard Dennis Cullity and Charles Danne Graham. *Introduction to Magnetic Materials*. IEEE/Wiley, Hoboken, N.J, 2nd ed edition, 2009. ISBN 978-0-471-47741-9.

[51] Sandrine Da Col, Michael Darques, Olivier Fruchart, and L. Cagnon. Reduction of magnetostatic interactions in self-organized arrays of nickel nanowires using atomic layer deposition. *Applied Physics Letters - APPL PHYS LETT*, 98, January 2011. doi: 10.1063/1.3562963.

[52] E. Dan Dahlberg and Jian-Gang Zhu. Micromagnetic Microscopy and Modeling. *Physics Today*, 48(4):34–40, April 1995. ISSN 0031-9228. doi: 10.1063/1.881447.

[53] Marcelo J. Dapino, Ralph C. Smith, Frederick T. Calkins, and Alison B. Flatau. A Coupled Magnetomechanical Model for Magnetostrictive Transducers and its Application to Villari-Effect Sensors. *Journal of Intelligent Material Systems and Structures*, 13 (11):737–747, November 2002. ISSN 1045-389X. doi: 10.1177/1045389X02013011005.

[54] Supratik Datta. *Quasi-Static Characterization and Modeling of the Bending Behavior of Single Crystal Galfenol for Magnetostrictive Sensors and Actuators*. PhD thesis, University of Maryland, College Park, United States – Maryland, 2009.

[55] Supratik Datta, Jayasimha Atulasimha, Chaitanya Mudivarthi, and Alison B. Flatau. Stress and magnetic field-dependent Young's modulus in single crystal iron–gallium alloys. *Journal of Magnetism and Magnetic Materials*, 322(15):2135–2144, August 2010. ISSN 0304-8853. doi: 10.1016/j.jmmm.2010.01.046.

[56] Daniele Davino, Alessandro Giustiniani, Ciro Visone, and Amr Adly. Experimental analysis of vibrations damping due to magnetostrictive based energy harvest-

ing. *Journal of Applied Physics*, 109(7):07E509, April 2011. ISSN 0021-8979. doi: 10.1063/1.3545798.

[57] Yaşar Demirel and Vincent Gerbaud. Fundamentals of Nonequilibrium Thermodynamics. In *Nonequilibrium Thermodynamics*, pages 135–186. Elsevier, 2019. ISBN 978-0-444-64112-0. doi: 10.1016/B978-0-444-64112-0.00003-4.

[58] Zhangxian Deng. Explicit and efficient discrete energy-averaged model for Terfenol-D. *Journal of Applied Physics*, 122(4):043901, July 2017. ISSN 0021-8979. doi: 10.1063/1.4994647.

[59] Zhangxian Deng and Marcelo J. Dapino. Review of magnetostrictive materials for structural vibration control. *Smart Materials and Structures*, 27(11):113001, November 2018. ISSN 0964-1726, 1361-665X. doi: 10.1088/1361-665X/aadff5.

[60] Zhangxian Deng, Justin J. Scheidler, Vivake M. Asnani, and Marcelo J. Dapino. Quasi-static major and minor strain-stress loops in textured polycrystalline Fe81.6Ga18.4 Galfenol. *Journal of Applied Physics*, 120(24):243901, December 2016. ISSN 0021-8979. doi: 10.1063/1.4972479.

[61] John P. Domann. Single Input Straintronics for Micro - Nanoscale Antennas and Motors. In IEEE Magnetics, editor, *62nd Annual Conference on Magnetism and Magnetic Materials*, pages 17–17. AIP Publishing, November 2017.

[62] Philippe Dreesen. *Polynomial System Solving Using Linear Algebra.* PhD thesis, Arenberg Doctoral School, Septemnber 2013.

[63] Igor Ekhielevich Dzialoshinskii. The Problem of piezomagnetism. *Journal of Experimental and Theoretical Physics*, page 2, September 1957.

[64] Farzad Ebrahimi and Mehrdad Farajzadeh Ahari. Thermomechanical active vibration control of auxetic plates with magnetostrictive layers. *Journal of the Brazilian Society of Mechanical Sciences and Engineering*, 46(1):19, December 2023. ISSN 1806-3691. doi: 10.1007/s40430-023-04597-w.

[65] Rani Elhajjar, Chiu-Tai Law, and Alessandro Pegoretti. Magnetostrictive polymer composites: Recent advances in materials, structures and properties. *Progress in Materials Science*, 97:204–229, August 2018. ISSN 0079-6425. doi: 10.1016/j.pmatsci.2018.02.005.

[66] Phillip G. Evans and Marcelo J. Dapino. State-Space Constitutive Model for Magnetization and Magnetostriction of Galfenol Alloys. *IEEE Transactions on Magnetics*, 44(7):1711–1720, July 2008. ISSN 1941-0069. doi: 10.1109/TMAG.2008.921534.

[67] Phillip G. Evans and Marcelo J. Dapino. Efficient model for field-induced magnetization and magnetostriction of Galfenol. *Journal of Applied Physics*, 105(11):113901, June 2009. ISSN 0021-8979. doi: 10.1063/1.3129316.

[68] Phillip G. Evans and Marcelo J. Dapino. Efficient magnetic hysteresis model for field and stress application in magnetostrictive Galfenol. *Journal of Applied Physics*, 107 (6):063906, March 2010. ISSN 0021-8979. doi: 10.1063/1.3318494.

[69] Phillip G. Evans and Marcelo J. Dapino. Measurement and modeling of magnetic hysteresis under field and stress application in iron–gallium alloys. *Journal of Magnetism and Magnetic Materials*, 330:37–48, March 2013. ISSN 03048853. doi: 10.1016/j.jmmm.2012.10.002.

[70] Lukas Exl, Johann Fischbacher, Alexander Kovacs, Harald Oezelt, Markus Gusenbauer, and Thomas Schrefl. Preconditioned nonlinear conjugate gradient method for

micromagnetic energy minimization. *Computer Physics Communications*, 235:179–186, February 2019. ISSN 00104655. doi: 10.1016/j.cpc.2018.09.004.

[71] Josef Fidler and Thomas Schrefl. Micromagnetic modelling—the current state of the art. 2004.

[72] Josef Fidler, Thomas Schrefl, Werner Scholz, Dieter Suess, Rok Dittrich, and Markus Kirschner. Micromagnetic modelling and magnetization processes. 2000.

[73] M. E. Foglio, Carlos A. Balseiro, and Leopoldo Máximo Falicov. New approach to the theory of intermediate valence. II. Magnetic susceptibility and magnetic instabilities. *Physical Review B*, 20(11):4560–4568, December 1979. ISSN 0163-1829. doi: 10.1103/PhysRevB.20.4560.

[74] Vincent François-Lavet, François Henrotte, Laurent Stainier, Ludovic Noels, and Christophe A. Geuzaine. An energy-based variational model of ferromagnetic hysteresis for finite element computations. *Journal of Computational and Applied Mathematics*, 246:243–250, July 2013. ISSN 0377-0427. doi: 10.1016/j.cam.2012.06.007.

[75] Jun Fujisaki, Atsushi Furuya, Yuji Uehara, Koichi Shimizu, Hirotaka Oshima, Tadakatsu Ohkubo, Satoshi Hirosawa, and Kazuhiro Hono. Micromagnetic Simulations of Magnetization Reversal in Misaligned Multigrain Magnets With Various Grain Boundary Properties Using Large-Scale Parallel Computing. *IEEE Transactions on Magnetics*, 50(11):1–4, November 2014. ISSN 1941-0069. doi: 10.1109/TMAG.2014.2326176.

[76] Chengde Gao, Zihao Zeng, Shuping Peng, and Cijun Shuai. Magnetostrictive alloys: Promising materials for biomedical applications. *Bioactive Materials*, 8:177–195, February 2022. ISSN 2452-199X. doi: 10.1016/j.bioactmat.2021.06.025.

[77] Mojtaba Ghodsi, Morteza Mohammadzaheri, Payam Soltani, and Hamidreza Ziaifar. A new active anti-vibration system using a magnetostrictive bimetal actuator. *Journal of Magnetism and Magnetic Materials*, 557:169463, September 2022. ISSN 0304-8853. doi: 10.1016/j.jmmm.2022.169463.

[78] Ramsis S. Girgis, Mats S. Bernesjö, Scott Thomas, Jan Anger, Donald Chu, and Harold R. Moore. Development of ultra — Low noise transformer technology. In *2011 IEEE Power and Energy Society General Meeting*, pages 1–8, July 2011. doi: 10.1109/PES.2011.6038896.

[79] Jesús María González. Magnetoelasticity and Magnetostriction for Implementing Biomedical Sensors. In Elisa López-Dolado and María Concepción Serrano, editors, *Engineering Biomaterials for Neural Applications: Targeting Traumatic Brain and Spinal Cord Injuries*, pages 127–147. Springer International Publishing, Cham, 2022. ISBN 978-3-030-81400-7. doi: 10.1007/978-3-030-81400-7_6.

[80] Sybren R. De Groot and Peter Mazur. *Non-Equilibrium Thermodynamics.* Courier Corporation, January 2013. ISBN 978-0-486-15350-6.

[81] Ryusuke Hasegawa and Daichi Azuma. Impacts of amorphous metal-based transformers on energy efficiency and environment. *Journal of Magnetism and Magnetic Materials*, 320(20):2451–2456, October 2008. ISSN 03048853. doi: 10.1016/j.jmmm.2008.04.052.

[82] Gokhan Hatipoglu and Srinivas Tadigadapa. Micromachined magnetoflexoelastic resonator based magnetometer. *Applied Physics Letters*, 107(19):192406, November 2015. ISSN 0003-6951. doi: 10.1063/1.4935790.

[83] Tom Hilgert, Lieven Vandevelde, and Jan Melkebeek. Neural-Network-Based Model for Dynamic Hysteresis in the Magnetostriction of Electrical Steel Under Sinusoidal

Induction. *IEEE Transactions on Magnetics*, 43(8):3462–3466, August 2007. ISSN 1941-0069. doi: 10.1109/TMAG.2007.899756.

[84] Kwangsoo Ho. A constitutive model for magnetostriction based on thermodynamic framework. *Journal of Magnetism and Magnetic Materials*, 412:250–254, August 2016. ISSN 0304-8853. doi: 10.1016/j.jmmm.2016.04.017.

[85] Mark F. Horstemeyer and Douglas J. Bammann. Historical review of internal state variable theory for inelasticity. *International Journal of Plasticity*, 26(9):1310–1334, September 2010. ISSN 07496419. doi: 10.1016/j.ijplas.2010.06.005.

[86] Jia-Mian Hu, Long-Qing Chen, and Ce-Wen Nan. Multiferroic Heterostructures Integrating Ferroelectric and Magnetic Materials. *Advanced Materials*, 28(1):15–39, 2016. ISSN 1521-4095. doi: 10.1002/adma.201502824.

[87] Olivier Hubert and Laurent Daniel. Measurement and Analytical Modeling of the Delta-E Effect in a Bulk Iron-Cobalt Alloy. *IEEE Transactions on Magnetics*, 46(2): 401–404, February 2010. ISSN 1941-0069. doi: 10.1109/TMAG.2009.2033387.

[88] Mohammed Ibrahim and Armaghan Salehian. Modeling, fabrication, and experimental validation of hybrid piezo-magnetostrictive and piezomagnetic energy harvesting units. *Journal of Intelligent Material Systems and Structures*, 26(10):1259–1271, July 2015. ISSN 1045-389X. doi: 10.1177/1045389X14538540.

[89] Alecsander N. Imhof and John P. Domann. Nonlinear one-dimensional constitutive model for magnetostrictive materials. *Multifunctional Materials*, 5(1):015002, February 2022. ISSN 2399-7532. doi: 10.1088/2399-7532/ac4ccd.

[90] James F. Janak. Uniform susceptibilities of metallic elements. *Physical Review B*, 16 (1):255–262, July 1977. ISSN 0556-2805. doi: 10.1103/PhysRevB.16.255.

[91] David C. Jiles and David L. Atherton. Theory of ferromagnetic hysteresis (invited). *Journal of Applied Physics*, 55(6):2115–2120, March 1984. ISSN 0021-8979. doi: 10.1063/1.333582.

[92] Guḥbjörn F. Jónsson and Stephen A. Vavasis. Accurate solution of polynomial equations using Macaulay resultant matrices. *Mathematics of Computation*, 74(249):221–263, July 2004. ISSN 0025-5718. doi: 10.1090/S0025-5718-04-01722-3.

[93] James P. Joule. XVII. On the effects of magnetism upon the dimensions of iron and steel bars. *The London, Edinburgh, and Dublin Philosophical Magazine and Journal of Science*, 30(199):76–87, February 1847. ISSN 1941-5966. doi: 10.1080/14786444708645656.

[94] Mehran Kardar. *Statistical Physics of Particles*. Cambridge University Press, June 2007. ISBN 978-1-139-46487-1.

[95] Shigetoshi Katsura. Statistical Mechanics of the Anisotropic Linear Heisenberg Model. *Physical Review*, 127(5):1508–1518, September 1962. ISSN 0031-899X. doi: 10.1103/PhysRev.127.1508.

[96] Rick A. Kellogg, Alison B. Flatau, Arthur E. Clark, Marilyn Wun-Fogle, and Thomas A. Lograsso. Temperature and stress dependencies of the magnetic and magnetostrictive properties of Fe0.81Ga0.19. *Journal of Applied Physics*, 91(10):7821–7823, May 2002. ISSN 0021-8979, 1089-7550. doi: 10.1063/1.1452216.

[97] Rick A. Kellogg, Alison B. Flatau, Arthur E. Clark, Marilyn Wun-Fogle, and Thomas A. Lograsso. Quasi-Static Transduction Characterization of Galfenol. In *ASME 2003 International Mechanical Engineering Congress and Exposition*, pages 273–280. American Society of Mechanical Engineers Digital Collection, November 2003. doi: 10.1115/IMECE2003-43140.

[98] Sok Kim, Kwanghun Kim, Kang Choe, U. JuHyok, and Hyongchol Rim. A nonlinear magneto-mechanical coupling model for magnetization and magnetostriction of ferromagnetic materials. *AIP Advances*, 10(8):085304, August 2020. doi: 10.1063/5.0016489.

[99] Charles Kittel. Physical Theory of Ferromagnetic Domains. *Reviews of Modern Physics*, 21(4):541–583, October 1949. ISSN 0034-6861. doi: 10.1103/RevModPhys.21.541.

[100] Signe Kjelstrup and Dick Bedeaux. Chapter 4. Local Equilibrium in Non-equilibrium Thermodynamics. In Dick Bedeaux, Signe Kjelstrup, and Jan Sengers, editors, *Experimental Thermodynamics Volume X*, pages 61–77. Royal Society of Chemistry, Cambridge, 2015. ISBN 978-1-78262-024-2. doi: 10.1039/9781782622543-00061.

[101] Mark B. Knickelbein. Chapter 11 - Uncovering New Magnetic Phenomena in Metal Clusters. In Purusottam Jena and A. Welford Castleman, editors, *Science and Technology of Atomic, Molecular, Condensed Matter & Biological Systems*, volume 1 of *Nanoclusters*, pages 415–435. Elsevier, January 2010. doi: 10.1016/B978-0-444-53440-8.00011-2.

[102] Jumpei Kobori, Yasuhito Takahashi, and Koji Fujiwara. The international round robin test of magnetostriction measurement of grain-oriented electrical steel by means of a single sheet tester and an optical sensor. *Journal of Magnetism and Magnetic Materials*, 513:166541, November 2020. ISSN 03048853. doi: 10.1016/j.jmmm.2020.166541.

[103] Amritesh Kumar and Arunachalakasi Arockiarajan. Evolution of nonlinear magneto-elastic constitutive laws in ferromagnetic materials: A comprehensive review. *Journal of Magnetism and Magnetic Materials*, 546:168821, March 2022. ISSN 0304-8853. doi: 10.1016/j.jmmm.2021.168821.

[104] Thomas Lafont, Leticia Gimeno, Jerome Delamare, Gor A. Lebedev, Dmitry I. Zakharov, Bernard Viala, Orphee Cugat, Nicolas Galopin, Lauric Garbuio, and Olivier Geoffroy. Magnetostrictive–piezoelectric composite structures for energy harvesting. *Journal of Micromechanics and Microengineering*, 22(9):094009, August 2012. ISSN 0960-1317. doi: 10.1088/0960-1317/22/9/094009.

[105] Lev D. Landau and Evgeny M. Lifshitz. *The Classical Theory of Fields*. Butterworth-Heinemann, 1976.

[106] Tomasz M. Łapiński. Approximations of the Sum of States by Laplace's Method for a System of Particles with a Finite Number of Energy Levels and Application to Limit Theorems. *Mathematical Physics, Analysis and Geometry*, 23(1):9, March 2020. ISSN 1572-9656. doi: 10.1007/s11040-020-9330-8.

[107] Dieter Lederer, Hajime Igarashi, Arnulf Kost, and Toshihisa Honma. On the parameter identification and application of the Jiles-Atherton hysteresis model for numerical modelling of measured characteristics. *IEEE Transactions on Magnetics*, 35(3):1211–1214, May 1999. ISSN 1941-0069. doi: 10.1109/20.767167.

[108] Jonathan Leliaert and Jeroen Mulkers. Tomorrow's micromagnetic simulations. *Journal of Applied Physics*, 125(18):180901, May 2019. ISSN 0021-8979. doi: 10.1063/1.5093730.

[109] An Li, Yuusuke Kobayashi, Yushin Hara, Keisuke Otsuka, and Kanjuro Makihara. Magnetostrictive-based induced current inversion and amplification: Semi-active vibration suppression for multiple-degree-of-freedom flexible structures. *Journal of Sound and Vibration*, 568:118069, January 2024. ISSN 0022-460X. doi: 10.1016/j.jsv.2023.118069.

[110] Deren Li, Shanhong Li, and Zhichao Lu. The effects of post-processing on longitudinal magnetostriction and core losses of high saturation flux density FeSiBC amorphous alloy ribbons and cores. *Journal of Magnetism and Magnetic Materials*, 538:168272, November 2021. ISSN 03048853. doi: 10.1016/j.jmmm.2021.168272.

[111] Jianwei Li and Minqiang Xu. Modified Jiles-Atherton-Sablik model for asymmetry in magnetomechanical effect under tensile and compressive stress. *Journal of Applied Physics*, 110(6):063918, September 2011. ISSN 0021-8979. doi: 10.1063/1.3638711.

[112] Cheng-Yen Liang, Scott M Keller, Abdon E Sepulveda, Alexandre Bur, Wei-Yang Sun, Kyle Wetzlar, and Greg P. Carman. Modeling of magnetoelastic nanostructures with a fully coupled mechanical-micromagnetic model. *Nanotechnology*, 25(43):435701, October 2014. ISSN 0957-4484, 1361-6528. doi: 10.1088/0957-4484/25/43/435701.

[113] Cheng-Yen Liang, Scott M. Keller, Abdon E. Sepulveda, Wei-Yang Sun, Jizhai Cui, Christopher S. Lynch, and Greg P. Carman. Electrical control of a single magnetoelastic domain structure on a clamped piezoelectric thin film—analysis. *Journal of Applied Physics*, 116(12):123909, September 2014. ISSN 0021-8979. doi: 10.1063/1.4896549.

[114] David J. C. MacKay. *Information Theory, Inference and Learning Algorithms*. Cambridge University Press, September 2003. ISBN 978-0-521-64298-9.

[115] Arjun Mahadevan, Phillip G. Evans, and Marcelo J. Dapino. Dependence of magnetic susceptibility on stress in textured polycrystalline Fe81.6Ga18.4 and Fe79.1Ga20.9 Galfenol alloys. *Applied Physics Letters*, 96(1):012502, January 2010. ISSN 0003-6951. doi: 10.1063/1.3280374.

[116] Alexander Maletzky. Under consideration for publication in Formal Aspects of Computing Gröbner Bases and Macaulay Matrices in Isabelle/HOL. In *Formal Aspects of Computing*, 2019.

[117] Amir Manbachi and Richard S C Cobbold. Development and Application of Piezoelectric Materials for Ultrasound Generation and Detection. *Ultrasound*, 19(4):187–196, November 2011. ISSN 1742-271X. doi: 10.1258/ult.2011.011027.

[118] Ansar Masood, Hasan A. Baghbaderani, Kenny L. Alvarez, Juan M. Blanco, Zoran Pavlovic, Valter Ström, Plamen S. Stamenov, Cian O. Mathuna, and Paul McCloskey. High-frequency power loss mechanisms in ultra-thin amorphous ribbons. *Journal of Magnetism and Magnetic Materials*, 519:167469, February 2021. ISSN 0304-8853. doi: 10.1016/j.jmmm.2020.167469.

[119] John H. McCabe. A continued fraction expansion, with a truncation error estimate, for Dawson's integral. *Mathematics of Computation*, 28(127):811–816, 1974. ISSN 0025-5718, 1088-6842. doi: 10.1090/S0025-5718-1974-0371020-3.

[120] Mateusz Michałek and Bernd Sturmfels. *Invitation to Nonlinear Algebra.* American Mathematical Soc., March 2021. ISBN 978-1-4704-6551-3.

[121] Mark B. Moffett, Arthur E. Clark, Marilyn Wun-Fogle, Jan Linberg, Joseph P. Teter, and Elizabeth A. McLaughlin. Characterization of Terfenol-D for magnetostrictive transducers. *The Journal of the Acoustical Society of America*, 89(3):1448–1455, March 1991. ISSN 0001-4966. doi: 10.1121/1.400678.

[122] Malick Mouhamad, Christophe Elleau, Frederic Mazaleyrat, Christian Guillaume, and Bertrand Jarry. Physicochemical and Accelerated Aging Tests of Metglas 2605SA1 and Metglas 2605HB1 Amorphous Ribbons for Power Applications. *IEEE Transactions on Magnetics*, 47(10):3192–3195, September 2011. doi: 10.1109/TMAG.2011.2158295.

[123] Nabil M'zali, Floran Martin, Ugur Aydin, Anouar Belahcen, Abdelkader Benabou, and Thomas Henneron. Determination of stress dependent magnetostriction from a macroscopic magneto-mechanical model and experimental magnetization curves. *Journal of*

*Magnetism and Magnetic Materials*, 500:166299, April 2020. ISSN 03048853. doi: 10.1016/j.jmmm.2019.166299.

[124] Yuji Nakatsukasa, Vanni Noferini, and Alex Townsend. Computing the common zeros of two bivariate functions via Bézout resultants. *Numerische Mathematik*, 129(1): 181–209, January 2015. ISSN 0945-3245. doi: 10.1007/s00211-014-0635-z.

[125] Ce-Wen Nan, M. I. Bichurin, Shuxiang Dong, D. Viehland, and G. Srinivasan. Multiferroic magnetoelectric composites: Historical perspective, status, and future directions. *Journal of Applied Physics*, 103(3):031101, February 2008. ISSN 0021-8979. doi: 10.1063/1.2836410.

[126] Fumio Narita and Marina Fox. A Review on Piezoelectric, Magnetostrictive, and Magnetoelectric Materials and Device Technologies for Energy Harvesting Applications. *Advanced Engineering Materials*, 20(5):1700743, May 2018. ISSN 1438-1656. doi: 10.1002/adem.201700743.

[127] Ismail Nas, Zhangxian Deng, Suryarghya Chakrabarti, and Marcelo J. Dapino. Parameter Optimization Algorithm of a Discrete Energy-Averaged Model for Galfenol Alloys. In *Volume 1: Development and Characterization of Multifunctional Materials; Mechanics and Behavior of Active Materials; Bioinspired Smart Materials and Systems; Energy Harvesting; Emerging Technologies*, page V001T02A005, Snowbird, Utah, USA, September 2017. American Society of Mechanical Engineers. ISBN 978-0-7918-5825-7. doi: 10.1115/SMASIS2017-3906.

[128] Henricus W. L. Naus. Ferromagnetic hysteresis and the effective field. *IEEE Transactions on Magnetics*, 38(5):3417–3419, September 2002. ISSN 1941-0069. doi: 10.1109/TMAG.2002.802714.

[129] Henricus W. L. Naus. Theoretical Developments in Magnetomechanics. *IEEE Transactions on Magnetics*, 47(9):2155–2162, September 2011. ISSN 1941-0069. doi: 10.1109/TMAG.2011.2134863.

[130] Ali H. Nayfeh, Mohammad I. Younis, and Eihab M. Abdel-Rahman. Reduced-Order Models for MEMS Applications. *Nonlinear Dynamics*, 41(1-3):211–236, August 2005. ISSN 0924-090X, 1573-269X. doi: 10.1007/s11071-005-2809-9.

[131] Robert E. Newnham. *Properties of Materials: Anisotropy, Symmetry, Structure*. OUP Oxford, 2005. ISBN 978-0-19-852075-7.

[132] Vanni Noferini and Alex Townsend. Numerical Instability of Resultant Methods for Multidimensional Rootfinding. *SIAM Journal on Numerical Analysis*, 54(2):719–743, January 2016. ISSN 0036-1429, 1095-7170. doi: 10.1137/15M1022513.

[133] Robert C. O'Handley. *Modern Magnetic Materials: Principles and Applications*. Wiley, New York, 2000. ISBN 978-0-471-15566-9.

[134] Frank W. J Olver. Error bounds for the laplace approximation for definite integrals. *Journal of Approximation Theory*, 1(3):293–313, November 1968. ISSN 0021-9045. doi: 10.1016/0021-9045(68)90007-5.

[135] Lars Onsager. Crystal Statistics. I. A Two-Dimensional Model with an Order-Disorder Transition. *Physical Review*, 65(3-4):117–149, February 1944. doi: 10.1103/PhysRev.65.117.

[136] Bor Plestenjak. Minimal determinantal representations of bivariate polynomials. *Linear Algebra and its Applications*, 532:550–569, November 2017. ISSN 00243795. doi: 10.1016/j.laa.2017.07.013.

[137] Bor Plestenjak and Michiel E. Hochstenbach. Roots of bivariate polynomial systems via determinantal representations. *SIAM Journal on Scientific Computing*, 38(2): A765–A788, January 2016. ISSN 1064-8275, 1095-7197. doi: 10.1137/140983847.

[138] Sadia Rafique, James R. Cullen, Manfred Wuttig, and Jun Cui. Magnetic anisotropy of FeGa alloys. *Journal of Applied Physics*, 95(11):6939–6941, June 2004. ISSN 0021-8979, 1089-7550. doi: 10.1063/1.1676054.

[139] Arun Raghunathan, Yevgen Melikhov, John E. Snyder, and David C. Jiles. Generalized form of anhysteretic magnetization function for Jiles–Atherton theory of hysteresis. *Applied Physics Letters*, 95(17):172510, October 2009. ISSN 0003-6951. doi: 10.1063/1.3249581.

[140] Alessio Recati and Sandro Stringari. Spin Fluctuations, Susceptibility, and the Dipole Oscillation of a Nearly Ferromagnetic Fermi Gas. *Physical Review Letters*, 106(8): 080402, February 2011. ISSN 0031-9007, 1079-7114. doi: 10.1103/PhysRevLett.106.080402.

[141] Limin Ren, Kun Yu, and Yisong Tan. Applications and Advances of Magnetoelastic Sensors in Biomedical Engineering: A Review. *Materials*, 12(7):1135, January 2019. ISSN 1996-1944. doi: 10.3390/ma12071135.

[142] James B. Restorff, Marilyn Wun-Fogle, Arthur E. Clark, and K.B. Hathaway. Induced Magnetic Anisotropy in Stress-Annealed Galfenol Alloys. *IEEE Transactions on Magnetics*, 42(10):3087–3089, October 2006. ISSN 1941-0069. doi: 10.1109/TMAG.2006.878395.

[143] James J. Rhyne and Arthur E. Clark. Magnetic Anisotropy of Terbium and Dysprosium. *Journal of Applied Physics*, 38(3):1379–1380, March 1967. ISSN 0021-8979, 1089-7550. doi: 10.1063/1.1709631.

[144] James J. Rhyne and Sam Legvold. Magnetostriction of Tb Single Crystals. *Physical Review*, 138(2A):A507–A514, April 1965. ISSN 0031-899X. doi: 10.1103/PhysRev.138.A507.

[145] Jungho Ryu, Alfredo Vázquez Carazo, Kenji Uchino, and Hyoun-Ee Kim. Magnetoelectric Properties in Piezoelectric and Magnetostrictive Laminate Composites. *Japanese Journal of Applied Physics*, 40(8R):4948, August 2001. ISSN 1347-4065. doi: 10.1143/JJAP.40.4948.

[146] Martin J. Sablik. A model for asymmetry in magnetic property behavior under tensile and compressive stress in steel. *IEEE Transactions on Magnetics*, 33(5):3958–3960, September 1997. ISSN 1941-0069. doi: 10.1109/20.619628.

[147] Martin J. Sablik and David C. Jiles. Coupled magnetoelastic theory of magnetic and magnetostrictive hysteresis. *IEEE Transactions on Magnetics*, 29(4):2113–2123, July 1993. ISSN 1941-0069. doi: 10.1109/20.221036.

[148] Martin J. Sablik, H. Kwun, G. L. Burkhardt, and David C. Jiles. Model for the effect of tensile and compressive stress on ferromagnetic hysteresis. *Journal of Applied Physics*, 61(8):3799–3801, April 1987. ISSN 0021-8979. doi: 10.1063/1.338650.

[149] Pejush Chandra Sarker, Youguang Guo, Hai Yan Lu, and Jian Guo Zhu. A generalized inverse Preisach dynamic hysteresis model of Fe-based amorphous magnetic materials. *Journal of Magnetism and Magnetic Materials*, 514:167290, November 2020. ISSN 03048853. doi: 10.1016/j.jmmm.2020.167290.

[150] Pengpeng Shi, Ke Jin, and Xiaojing Zheng. A general nonlinear magnetomechanical model for ferromagnetic materials under a constant weak magnetic field. *Journal of Applied Physics*, 119(14):145103, April 2016. ISSN 0021-8979. doi: 10.1063/1.4945766.

[151] Harshita Singh and Scott D. Sudhoff. Reconsideration of Energy Balance in Jiles–Atherton Model for Accurate Prediction of B–H Trajectories in Ferrites. *IEEE Transactions on Magnetics*, 56(7):1–8, July 2020. ISSN 1941-0069. doi: 10.1109/TMAG.2020.2994022.

[152] Julie Slaughter. TERFENOL-D Lamination Process Cost Reduction. Technical report, ETREMA PRODUCTS INC AMES IA, November 1998.

[153] Julie Slaughter. TERFENOL-D Lamination Process Cost Reduction, Option 1. Technical report, ETREMA PRODUCTS INC AMES IA, October 1999.

[154] Ralph C. Smith, Marcelo J. Dapino, and Stefan Seelecke. Free energy model for hysteresis in magnetostrictive transducers. *Journal of Applied Physics*, 93(1):458–466, January 2003. ISSN 0021-8979. doi: 10.1063/1.1524312.

[155] Ivan V. Soldatov and Rudolf Schäfer. Selective sensitivity in Kerr microscopy. *Review of Scientific Instruments*, 88(7):073701, July 2017. ISSN 0034-6748. doi: 10.1063/1.4991820.

[156] Hans J. Stetter. *Numerical Polynomial Algebra.* Society for Industrial and Applied Mathematics, January 2004. ISBN 978-0-89871-557-6 978-0-89871-797-6. doi: 10.1137/1.9780898717976.

[157] Shaik M. Subhani, Subramanian Maniprakash, and Arunachalakasi Arockiarajan. Nonlinear magneto-electro-mechanical response of layered magneto-electric composites: Theoretical and experimental approach. *Acta Mechanica*, 228(9):3185–3201, September 2017. ISSN 1619-6937. doi: 10.1007/s00707-017-1889-1.

[158] Soheil Talebian, Yousef Hojjat, Mojtaba Ghodsi, and Mohammad Reza Karafi. Study on classical and excess eddy currents losses of Terfenol-D. *Journal of Magnetism and*

*Magnetic Materials*, 388:150–159, August 2015. ISSN 03048853. doi: 10.1016/j.jmmm.2015.04.033.

[159] Hakeim Talleb and Zhuoxiang Ren. Modeling of multiferroic composites using a multiscale approach with the temperature dependence. In *Conference CEFC 2020*, November 2020.

[160] Hafez Tari, Justin J. Scheidler, and Marcelo J. Dapino. Robust solution procedure for the discrete energy-averaged model on the calculation of 3D hysteretic magnetization and magnetostriction of iron–gallium alloys. *Journal of Magnetism and Magnetic Materials*, 384:266–275, June 2015. ISSN 0304-8853. doi: 10.1016/j.jmmm.2015.02.035.

[161] Hafez Tari, Sushma S Santapuri, and Marcelo J. Dapino. Efficient and robust nonlinear model for smart materials with application to composite magnetostrictive plates. *Smart Materials and Structures*, 26(4):045010, April 2017. ISSN 0964-1726, 1361-665X. doi: 10.1088/1361-665X/aa5fe3.

[162] Simon Telen. *Solving Systems of Polynomial Equations.* PhD thesis, University of California at Berkeley, 2016.

[163] Luke Tierney and Joseph B. Kadane. Accurate Approximations for Posterior Moments and Marginal Densities. *Journal of the American Statistical Association*, 81(393):82–86, March 1986. ISSN 0162-1459. doi: 10.1080/01621459.1986.10478240.

[164] Luke Tierney, Robert E. Kass, and Joseph B. Kadane. Fully Exponential Laplace Approximations to Expectations and Variances of Nonpositive Functions. *Journal of the American Statistical Association*, 84(407):710–716, 1989. ISSN 0162-1459. doi: 10.2307/2289652.

[165] Hiroshi Tsukahara, Kaoru Iwano, Chiharu Mitsumata, Tadashi Ishikawa, and Kanta

Ono. Micromagnetic simulation for the magnetization reversal process of Nd-Fe-B hot-deformed nanocrystalline permanent magnets. *AIP Advances*, 7(5):056234, March 2017. ISSN 2158-3226. doi: 10.1063/1.4978645.

[166] Shohei Ueno, Takashi Todaka, and Masato Enokizono. Measurement of Vector Magnetic Properties of Fe–Si–B Amorphous Material. *IEEE Transactions on Magnetics*, 47(10):3188–3191, October 2011. ISSN 1941-0069. doi: 10.1109/TMAG.2011.2158524.

[167] Rajesh Venkataraman and Perinkulam S. Krishnaprasad. Qualitative analysis of a bulk ferromagnetic hysteresis model. In *Proceedings of the 37th IEEE Conference on Decision and Control (Cat. No.98CH36171)*, volume 3, pages 2443–2448 vol.3, December 1998. doi: 10.1109/CDC.1998.757777.

[168] Dwight Viehland, Manfred Wuttig, Jeffrey McCord, and Eckhard Quandt. Magnetoelectric magnetic field sensors. *MRS Bulletin*, 43(11):834–840, November 2018. ISSN 0883-7694, 1938-1425. doi: 10.1557/mrs.2018.261.

[169] Sajan K. Wahi, Manik Kumar, Sushma Santapuri, and Marcelo J. Dapino. Computationally efficient locally linearized constitutive model for magnetostrictive materials. *Journal of Applied Physics*, 125(21):215108, June 2019. ISSN 0021-8979. doi: 10.1063/1.5086953.

[170] Yongping Wan, Daining Fang, and Keh-Chih Hwang. Non-linear constitutive relations for magnetostrictive materials. *International Journal of Non-Linear Mechanics*, 38(7): 1053–1065, October 2003. ISSN 0020-7462. doi: 10.1016/S0020-7462(02)00052-5.

[171] Jian Wang, Yu Lu, Lei Ye, Rong Chen, and Richard Leach. Efficient analysis-suitable T-spline fitting for freeform surface reconstruction and intelligent sampling. *Precision Engineering*, 66:417–428, November 2020. ISSN 01416359. doi: 10.1016/j.precisioneng.2020.08.008.

[172] Jun Wang, Tiefu Zhao, Jun Li, Alex Q. Huang, Robert Callanan, Fatima Husna, and Anant Agarwal. Characterization, Modeling, and Application of 10-kV SiC MOSFET. *IEEE Transactions on Electron Devices*, 55(8):1798–1806, August 2008. ISSN 1557-9646. doi: 10.1109/TED.2008.926650.

[173] Nai-juan Wang, Yuan Liu, Hua-wei Zhang, Xiang Chen, and Yan-xiang Li. Fabrication, magnetostriction properties and applications of Tb-Dy-Fe alloys: A review. *China Foundry*, 13(2):75–84, March 2016. ISSN 2365-9459. doi: 10.1007/s41230-016-5114-y.

[174] Qianchang Wang, John P. Domann, Guoqiang Yu, and Greg P. Carman. Strain Assisted Field-Free Deterministic Switching of Perpendicular Magnetization by Spin-Orbit Torque. In IEEE Magnetics, editor, *62nd Annual Conference on Magnetism and Magnetic Materials*, pages 200–200. AIP Publishing, November 2017.

[175] Qianchang Wang, Xu Li, Cheng-Yen Liang, Anthony Barra, John P. Domann, Chris Lynch, Abdon Sepulveda, and Greg P. Carman. Strain-mediated 180° switching in CoFeB and Terfenol-D nanodots with perpendicular magnetic anisotropy. *Applied Physics Letters*, 110(10):102903, March 2017. ISSN 0003-6951, 1077-3118. doi: 10.1063/1.4978270.

[176] Sumei Wang, Dan Wei, and Kai-Zhong Gao. Limits of Discretization in Computational Micromagnetics. *IEEE Transactions on Magnetics*, 47(10):3813–3816, October 2011. ISSN 1941-0069. doi: 10.1109/TMAG.2011.2157474.

[177] Wenjie Wang, Yue Xiang, Jingfeng Yu, and Long Yang. Development and Prospect of Smart Materials and Structures for Aerospace Sensing Systems and Applications. *Sensors*, 23(3):1545, January 2023. ISSN 1424-8220. doi: 10.3390/s23031545.

[178] Marilyn Wun-Fogle, James B. Restorff, and Arthur E. Clark. Magnetostriction of Stress-annealed Fe-Ga and Fe-Ga-Al Alloys under Compressive and Tensile Stress.

*Journal of Intelligent Material Systems and Structures*, 17(2):117–122, February 2006. ISSN 1045-389X. doi: 10.1177/1045389X06056060.

[179] Zhi Yan. Modeling of a piezoelectric/piezomagnetic nano energy harvester based on two dimensional theory. *Smart Materials and Structures*, 27(1):015016, January 2018. ISSN 0964-1726, 1361-665X. doi: 10.1088/1361-665X/aa9bbd.

[180] Long Yang, Wenjie Wang, Xu Zhao, Haojun Li, and Yue Xiang. Design and Optimization of High-Power and Low-Frequency Broadband Transducer with Giant Magnetostrictive Material. *Sensors*, 23(1):108, January 2023. ISSN 1424-8220. doi: 10.3390/s23010108.

[181] Can Evren Yarman. Approximating fractional derivative of Faddeeva function, Gaussian function, and Dawson's integral. *Mathematical Methods in the Applied Sciences*, 44(10):8042–8056, 2021. ISSN 1099-1476. doi: 10.1002/mma.5679.

[182] Sicheng Yi, Quan Zhang, Xiaoqing Sun, Bintang Yang, and Guang Meng. Simultaneous micropositioning and microvibration control of a magnetostrictive Stewart platform with synthesized strategy. *Mechanical Systems and Signal Processing*, 187:109925, March 2023. ISSN 0888-3270. doi: 10.1016/j.ymssp.2022.109925.

[183] JinHyeong Yoo and Nicholas J. Jones. A Performance Prediction for Fe–Ga Magnetostrictive Strain Sensor Using Simplified Model. *IEEE Transactions on Magnetics*, 53(11):1–4, November 2017. ISSN 1941-0069. doi: 10.1109/TMAG.2017.2698340.

[184] Mohammad I. Younis, Eihab M. Abdel-Rahman, and Ali H. Nayfeh. A reduced-order model for electrically actuated microbeam-based MEMS. *Journal of Microelectromechanical Systems*, 12(5):672–680, October 2003. ISSN 1941-0158. doi: 10.1109/JMEMS.2003.818069.

[185] Mofreh R. Zaghloul. Efficient numerical algorithms for multi-precision and multi-accuracy calculation of the error functions and Dawson integral with complex arguments. *Numerical Algorithms*, February 2024. ISSN 1017-1398, 1572-9265. doi: 10.1007/s11075-023-01727-2.

[186] Ashraf M. Zenkour and Hela D. El-Shahrany. Vibration suppression of magnetostrictive laminated beams resting on viscoelastic foundation. *Applied Mathematics and Mechanics*, 41(8):1269–1286, August 2020. ISSN 1573-2754. doi: 10.1007/s10483-020-2635-7.

[187] Da-Guang Zhang, Meng-Han Li, and Hao-Miao Zhou. A general one-dimension nonlinear magneto-elastic coupled constitutive model for magnetostrictive materials. *AIP Advances*, 5(10):107201, October 2015. doi: 10.1063/1.4933024.

[188] Xugen G. Zhao and D. G. Lord. Magnetostriction and susceptibilities of twinned single crystals of Terfenol-D. *Journal of Applied Physics*, 83(11):7276–7278, June 1998. ISSN 0021-8979. doi: 10.1063/1.367617.

[189] Hao-Miao Zhou, Meng-Han Li, Xiao-Hong Li, and Da-Guang Zhang. An analytical and explicit multi-field coupled nonlinear constitutive model for Terfenol-D giant magnetostrictive material. *Smart Materials and Structures*, 25(8):085036, July 2016. ISSN 0964-1726. doi: 10.1088/0964-1726/25/8/085036.

[190] Lixun Zhu, Hee-Sung Yoon, Hyun-Jin Cho, Doo-Jong Um, and Chang-Seop Koh. Finite-Element Analysis of Magnetostriction Force in Power Transformer Based on the Measurement of Anisotropic Magnetostriction of Highly Grain-Oriented Electrical Steel Sheet. *IEEE Transactions on Magnetics*, 52(3):1–4, March 2016. ISSN 1941-0069. doi: 10.1109/TMAG.2015.2481466.

[191] Hans Ziegler. An attempt to generalize Onsager's principle, and its significance for rheological problems. *ZAMP Zeitschrift für Angewandte Mathematik und Physik*, 9 (5-6):748–763, March 1958. ISSN 0044-2275, 1420-9039. doi: 10.1007/BF02424793.

[192] Hans Ziegler. A modification of Prager's hardening rule. *Quarterly of Applied Mathematics*, 17(1):55–65, 1959. ISSN 0033-569X, 1552-4485. doi: 10.1090/qam/104405.

[193] Hans Ziegler. Zwei Extremalprinzipien der irreversiblen Thermodynamik. *Ingenieur-Archiv*, 30(6):410–416, 1961. ISSN 0020-1154, 1432-0681. doi: 10.1007/BF00531783.

[194] Hans Ziegler. A Possible Generalization of Onsager's Theory. In H. Parkus and L. I. Sedov, editors, *Irreversible Aspects of Continuum Mechanics and Transfer of Physical Characteristics in Moving Fluids*, pages 411–424. Springer Vienna, Vienna, 1968. ISBN 978-3-7091-5583-7 978-3-7091-5581-3. doi: 10.1007/978-3-7091-5581-3_29.

# Appendices

# Appendix A

# Appendix for Chapter 3

## A.1 Low Anisotropy Series Expansion

As previously stated, the solutions become indeterminate when $A = 0$. By performing a series expansion of $\exp(Am_1^2)$ about $A = 0$ we not only provide a solution for when $A = 0$, but also obtain an accurate solution when $h >> |A|$. Expanding the exponential about $A = 0$ and substituting it into the partition function we find that,

$$z/2\pi = \sum_{n=0}^{N} z_n = \sum_{n=0}^{N} \int_{-1}^{1} \frac{(-Am_1^2)^n}{n!} \exp(hm_1) \mathrm{d}m_1 \tag{A.1}$$

which has the general solution

$$z_n = \frac{(2n)!(-A)^n(-h)^{-2n}}{hn!} \left( (-1)^{4n+1} - 1 + \sum_{k=0}^{2n} \frac{(-h)^k \mathrm{e}^h + (-1)^{4n+1} h^k \mathrm{e}^{-h}}{k!} \right). \tag{A.2}$$

This expression has been provided in terms of polynomial expansions, however slightly more compact expressions can be obtained in terms of gamma functions. As the expressions can become very lengthy, the authors utilized a computer algebra system (Mathematica) to simplify the expressions and export them for use in Matlab.

Using the thermodynamic relationships described above both the average material response and material properties can be found by taking partial derivatives of $z_n$ with respect to $h$

and $A$ for a desired level of accuracy, controlled by $N$. In the error analysis below, a value of $N = 2$ was utilized.

## A.2 Material Properties

Magnetization and magnetostriction (Equations (4.17) and (4.18)) are proportional to $\langle \boldsymbol{m} \rangle$ and $\langle \boldsymbol{m} \otimes \boldsymbol{m} \rangle$. When restricted to one dimensional behavior, this can be simplified to

$$\langle M \rangle = M_s \langle m \rangle \tag{A.3}$$

$$\langle \varepsilon_m \rangle = \frac{3}{2} \lambda_s \langle m^2 \rangle \tag{A.4}$$

Using this new notation the relationships in equations (3.8) - (3.10) can be rewritten as

$$\langle \chi \rangle = \beta \mu_0 M_s^2 \left[ \langle m^2 \rangle - \langle m \rangle^2 \right] \tag{A.5}$$

$$\langle S_m \rangle = \beta \left( \frac{3\lambda_s}{2} \right)^2 \left[ \langle m^4 \rangle - \langle m^2 \rangle^2 \right] \tag{A.6}$$

$$\langle q \rangle = \beta M_s \frac{3\lambda_s}{2} \left[ \langle m^3 \rangle - \langle m \rangle \langle m^2 \rangle \right] \tag{A.7}$$

The definitions for $\langle m \rangle$ and $\langle m^2 \rangle$ were previously presented in equations (3.23) and (3.24). The only terms yet to be defined are the tensor products $\{ \langle \boldsymbol{m} \otimes \boldsymbol{m} \otimes \boldsymbol{m} \rangle, \langle \boldsymbol{m} \otimes \boldsymbol{m} \otimes \boldsymbol{m} \otimes \boldsymbol{m} \rangle \}$

simplified in one dimension as $\{\langle m^3\rangle, \langle m^4\rangle\}$ respectively. These two terms are shown here.

$$\langle m^3\rangle = \begin{cases} \frac{1}{\tilde{z}_+ 8A^{7/2}} \Big(\sqrt{A}\left(4A^2\left(1-e^{-2h}\right)-2A\left(e^{-2h}(h-2)+h+2\right)\right. & \\ \qquad \left. +\left(1-e^{-2h}\right)h^2\right)\Big)-\frac{6Ah+h^3}{8A^3} & A>0 \\ & \\ \frac{1}{\tilde{z}_- 8A^3}\left(4A^2\left(1-e^{-2h}\right)-2A\left(e^{-2h}(h-2)+h+2\right)\right. & \\ \qquad \left. +\left(1-e^{-2h}\right)h^2\right)+\frac{6Ah-h^3}{8A^3} & A<0,\ \gamma_+>0 \\ & \\ \frac{1}{\tilde{z}_- 8A^3}\Big(e^{-\gamma 1^2-\gamma 2^2}\left(\left(\frac{1}{2}\left(e^h-e^{-h}\right)\left(6Ah+8(A-1)A+5h^2\right)\right.\right. & \\ +\frac{1}{2}\left(e^{-h}+e^h\right)h(2A+3h)\big)e^{\gamma 1^2+h}-3e^{\gamma 2^2}h(2A+h)\Big)\Big)+\frac{6Ah-h^3}{8A^3} & A<0,\ \gamma_+<0 \end{cases} \tag{A.8}$$

$$\langle m^4\rangle = \begin{cases} \frac{1}{\tilde{z}_+ 8A^4}\left(A\left(e^{-2h}+1\right)\left(4A^2-6A+h^2\right)\right. & \\ \left.-\frac{1}{2}\left(1-e^{-2h}\right)h\left(2A(2A-5)+h^2\right)\right)+\frac{12A^2-12Ah^2+h^4}{16A^4} & A>0 \\ & \\ \frac{1}{\tilde{z}_- 16A^4}\left(e^{-2h}\left(8A^3\left(e^{-2h}+1\right)-4A^2\left(e^{-2h}(3-h)+h+3\right)\right.\right. & \\ \left.\left.+2Ah\left(e^{-2h}(h-5)+h+5\right)-\left(1-e^{-2h}\right)h^3\right)\right)+\frac{12A^2-12Ah^2+h^4}{16A^4} & A<0,\ \gamma_+>0 \\ & \\ \frac{1}{\tilde{z}_- 16A^4}\Big(e^{-\gamma 2^2}\left(8A^3\left(e^{2h}+1\right)+4A^2\left(h-e^{2h}(h+3)-3\right)\right. & \\ -2Ah\left(-6he^{\gamma 2^2-\gamma 1^2}+5e^{2h}(h-1)-h+5\right)-h^3\left(-6e^{\gamma 2^2-\gamma 1^2}+7e^{2h}-1\right)\Big)\Big) & \\ +\frac{12A^2-12Ah^2+h^4}{16A^4} & A<0,\ \gamma_+<0 \end{cases} \tag{A.9}$$

## A.3 Error Surfaces

The following figures are the error surfaces generated by comparing the presented model to numerical integration. A grid of $N = 100$ logarithmically spaced field points $10^{-2} \leq h \leq 10^6$ and $N = 200$ logarithmically spaced anisotropies $10^{-2} \leq |\pm A| \leq 10^6$ were generated for $N_{total} = 20,000$ points. At each grid point numerical integration was performed using Matlab's `integral()` function with relative and absolute errors of $10^{-12}$. The relative errors for each equation were calculated as $|f_{num} - f_{eqn}|/f_{num}$, where $f$ is the parameter of interest.

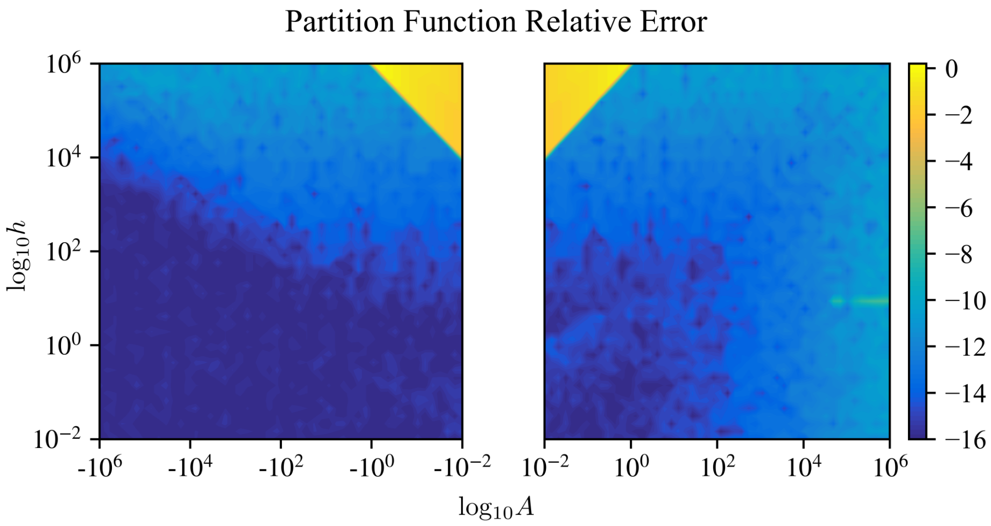

Figure A.1: Logarithmically scaled relative error of the equation (3.21) for $\tilde{z}$ compared to standard numerical integration with absolute errors $10^{-12}$

Figure A.1 examines equation (3.21) for $\tilde{z}$ which notably includes the energy offsets shown in (3.22). Including these offsets changes the numerical value of the partition function, however only the slope of $\tilde{z}$ produces observable quantities, so the shift has negligible physical impact. The yellow triangular region, which has relative errors ranging from 10% to 100%, is where the low anisotropy series expansion was employed ($|A|/h < 10^{-7}$). While this error is quite high Figures A.2 and A.3 below show that the low anisotropy expansion maintained low relative errors for the magnetization and magnetostriction, respectively. Outside the expansion region the equations for $\tilde{z}$ maintains an average relative error near $10^{-14}$.

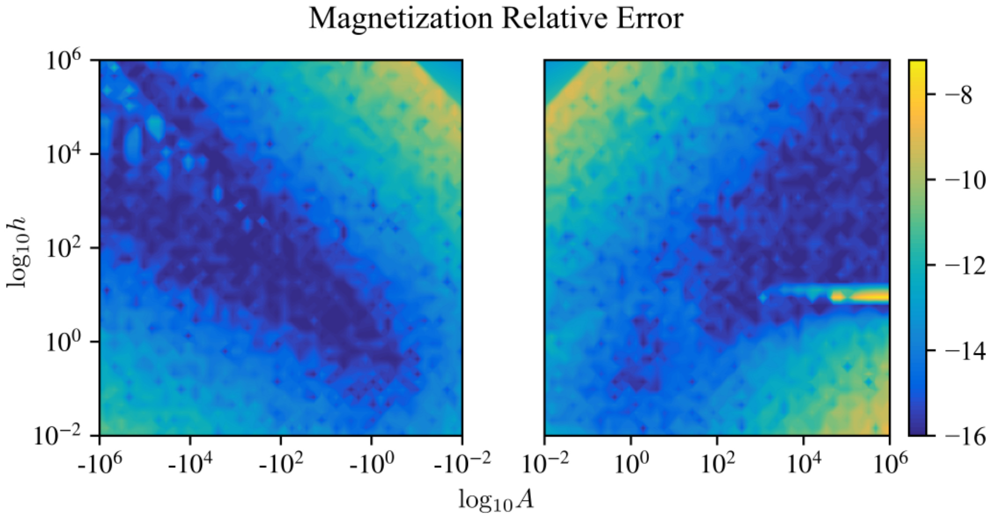

Figure A.2: Logarithmically scaled relative error of equation (3.23) for $\langle M \rangle$ compared to standard numerical integration with absolute errors $10^{-12}$

Figure A.2 compares equation (3.23) for $\langle M \rangle$ to numerical integration. Over all tested field values the relative error ranged from only $10^{-16}$ to $10^{-8}$ showing that the magnetization solutions maintain significant numerical accuracy for all applied fields and stresses. The error starts increasing as $h/|A|$ grows, however once the low anisotropy expansion is utilized the error returns to $10^{-13}$.

Finally, Figure A.3 compares equation (3.24) for $\langle \varepsilon_m \rangle$ to numerical integration. The maximum observed error in this graph remains $\leq 10^{-3}$. While the error once again climbs as both $h/|A|$ grows, the low anisotropy expansion prevents the error from climbing any larger.

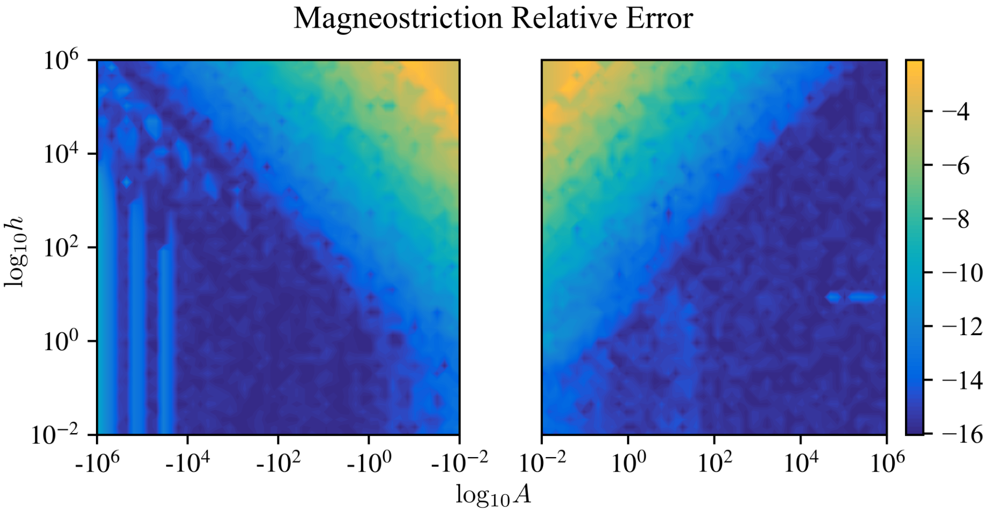

Figure A.3: Logarithmically scaled relative error of equation (3.24) for $\langle \varepsilon_m \rangle$ compared to standard numerical integration with absolute errors $10^{-12}$

# Appendix B

# Appendix for Chapter 4

## B.1 Author's DEA validation

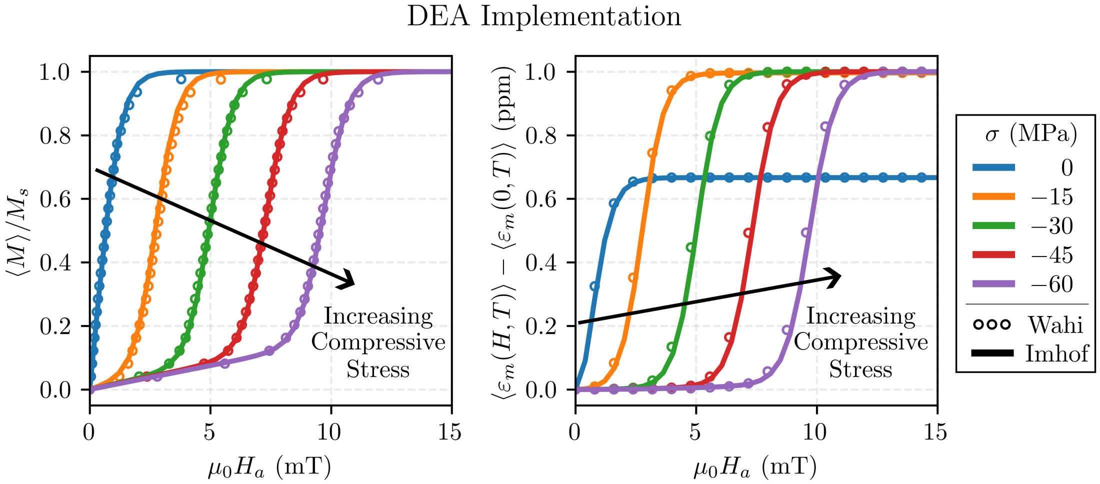

Figure B.1: Comparison of the author's implementation of the Wahi model, shown with the solid lines, to the dotted results presented by Wahi *et al.*

Table B.1: Wahi Material Properties

| $M_s$ | $(3/2)\lambda_{100}$ | $(3/2)\lambda_{111}$ | $K_1$ | $K_2$ | $\Omega$ | $\Gamma$ |
|---|---|---|---|---|---|---|
| $1.83/\mu_0$ | $255\times10^{-6}$ | $-7\times10^{-6}$ | $3.6\times10^{4}$ | 0 | 625 | 0.8 |

*Units: $M_s$ (A/M), $\lambda_{100}$ & $\lambda_{111}$ (-), $K_1$ & $K_2$ (J/m$^3$), $\Omega$ (J/m$^3$), $\Gamma$ (-)

Figure B.1 plots the MH curves of the DEA model presented in 2019 [169], and the authors implementation of that same model. The MH curves were digitized by the authors, and the material parameters used in the author's implementation shown in Table B.1 were taken directly from the text. The near exact fit shown in Figure B.1 proves the authors have faithfully reproduced the DEA model. The minor difference near the saturation region is most likely due to the digitization process employed by the authors.

## B.2 DEA Extrema Finding

The DEA model uses the method of Lagrange multipliers to find the extrema of the microscale free energy density $g_L(\boldsymbol{m})$, with the constraint $f(\boldsymbol{m})$ that the minima must lie on the unit sphere,

$$\mathcal{L}(\boldsymbol{m},\lambda) = g_L(\boldsymbol{m}) - \lambda f(\boldsymbol{m}), \tag{B.1}$$

$$f(\boldsymbol{m}) = \boldsymbol{m}\cdot\boldsymbol{m} - 1 = 0. \tag{B.2}$$

As minimizing the non-linear free energy was found to be computationally expensive a Taylor series expansion is performed about the crystallographic easy axes of the unloaded material $\boldsymbol{c}$,

$$\begin{aligned} \tilde{g}_L(\boldsymbol{m}) = g_L(\boldsymbol{m})\big|_{\boldsymbol{c}} &+ \left.\frac{\partial g_L(\boldsymbol{m})}{\partial m_i}\right|_{\boldsymbol{c}} (m_i - c_i) \\ &+ \frac{1}{2}\left.\frac{\partial^2 g_L(\boldsymbol{m})}{\partial m_i \partial m_j}\right|_{\boldsymbol{c}} (m_i - c_i)\,(m_i - c_i)\,(m_j - c_j) \end{aligned}. \tag{B.3}$$

The constraint was also linearized and reduced as follows,

$$\tilde{f}(\boldsymbol{m}) = 2(\boldsymbol{m}\cdot\boldsymbol{c} - 1), \tag{B.4}$$

$$\boldsymbol{m}\cdot\boldsymbol{c} \approx 1. \tag{B.5}$$

Minimizing the Lagrangian produces,

$$\boldsymbol{m} = \boldsymbol{\kappa}^{-1}(\lambda \boldsymbol{c} + \boldsymbol{A}) + \boldsymbol{c}, \tag{B.6}$$

$$\lambda = -\frac{\boldsymbol{\kappa}^{-1}\boldsymbol{A} \cdot \boldsymbol{c}}{\boldsymbol{\kappa}^{-1}\boldsymbol{c} \cdot \boldsymbol{c}}, \tag{B.7}$$

where $\boldsymbol{A}$ and $\boldsymbol{\kappa}$ are the first and second derivatives of the free energy at the crystallographic directions respectively.

$$\boldsymbol{A} = \left.\frac{\partial g_L(\boldsymbol{m})}{\partial m_i}\right|_{\boldsymbol{c}} \tag{B.8}$$

$$\boldsymbol{\kappa} = \left.\frac{\partial^2 g_L(\boldsymbol{m})}{\partial m_i \partial m_j}\right|_{\boldsymbol{c}} \tag{B.9}$$

Wahi *et al.* found that inverting $\boldsymbol{\kappa}$ can fail under certain loading conditions so $\tilde{\boldsymbol{\kappa}}$ was defined to prevent this failure,

$$\tilde{\boldsymbol{\kappa}} = \boldsymbol{\kappa} + 2K_1 \boldsymbol{c} \otimes \boldsymbol{c}. \tag{B.10}$$

Finally, it was possible for the solutions of $m$ in Equation (B.6) to lie off of the unit sphere and so each solution was then normalized,

$$\boldsymbol{m} = \frac{\boldsymbol{m}}{||\boldsymbol{m}||}. \tag{B.11}$$

## B.3 Strain Controlled Micromagnetic Magnetostriction

The magnetoelastic anisotropy with strain as the independent variable is,

$$g_{ME}(\boldsymbol{m};\boldsymbol{\varepsilon}) = B_1 \sum_i \left(m_i^2 - \frac{1}{3}\right)\varepsilon_{ii} + B_2 \sum_{i\neq j} m_i m_j \varepsilon_{ij}, \tag{B.12}$$

where $B_1$ and $B_2$ are the magnetoelastic coupling constants [41]. $B_1$ and $B_2$ have the following relation to the saturation magnetostriction constants,

$$\lambda_{100} = -\frac{2}{3}\frac{B_1}{c_{12} - c_{11}}, \tag{B.13}$$

$$\lambda_{111} = -\frac{1}{3}\frac{B_2}{c_{44}}. \tag{B.14}$$

For the test performed for Figure 4.7 (b) this version of magnetostriction was used. To find the extrema to predict the strain-controlled magnetization the procedure presented in B.2 was performed a second time with the new definition of $g_L$.

## B.4 Fourier Extrema Finding

After restricting the Landau free energy to the thin film case, its derivative with respect to $\phi$ can be represented as a Fourier series,

$$f_N(\phi) \equiv \sum_{j=0}^{N} a_j \cos(j\phi) + \sum_{j=1}^{N} b_j \sin(j\phi). \tag{B.15}$$

where $N$ is a variable related to the order or degree of the Landau free energy. The extrema of a Fourier series can be calculated from the eigenvalues of a generalized Frobenius companion matrix. To populate the Frobenius companion matrix the following vector is needed,

$$h_k = \begin{cases} a_{N-k} + \mathrm{i}b_{N-k}, & k = 0, 1, ..., (N-1) \\ 2_{a_0}, & k = N \\ a_{k-N} - \mathrm{i}b_{k-N}, & k = N+1, N+2, ..., 2N \end{cases} . \tag{B.16}$$

The companion matrix is defined as,

$$B_{jk} = \begin{cases} \delta_{j,k-1}, & j = 1, 2, ..., (2N-1) \\ -\frac{h_{k-1}}{a_N - \mathrm{i}b_N}, & j = 2N \end{cases} , \tag{B.17}$$

where $\delta$ is the Kronecker delta. With the eigenvalues of $B_{jk}$ given as $z_k$ the extrema of $f_N(\phi)$ are,

$$\phi_k = -\mathrm{i}\log(z_k). \tag{B.18}$$

Through the use of the companion matrix method the energy extrema can be found to near machine precision [28, 30]. The runtime and accuracy of this method are presented in the results subsection 4.4.1.